

AD-A077 151

ILLINOIS UNIV AT URBANA-CHAMPAIGN COORDINATED SCIENCE LAB F/G 7/4  
EXTREMAL EFFECTS IN ROTATIONALLY INELASTIC DIFFRACTION.(U)

MAR 79 L C RATHBUN

DAAB07-72-C-0259

UNCLASSIFIED

R-840

NL

1 OF 2  
AD-A077151



REPORT R-640 MARCH, 1979

UILU-ENG 78-2233

42

**CSL COORDINATED SCIENCE LABORATORY**

LEVEL

AD A 077151

**EXTREMAL EFFECTS IN  
ROTATIONALLY  
INELASTIC DIFFRACTION**

LYNN CHARLES RATHBUN



DDC FILE COPY

APPROVED FOR PUBLIC RELEASE. DISTRIBUTION UNLIMITED.

UNIVERSITY OF ILLINOIS - URBANA, ILLINOIS

79 11 21 025

## UNCLASSIFIED

SECURITY CLASSIFICATION OF THIS PAGE (When Data Entered)

REPORT DOCUMENTATION PAGE			READ INSTRUCTIONS BEFORE COMPLETING FORM
1. REPORT NUMBER	2. GOVT ACCESSION NO.	3. RECIPIENT'S CATALOG NUMBER	(9) Doctoral Thesis,
4. TITLE (and Subtitle)	5. TYPE OF REPORT & PERIOD COVERED		
(6) EXTREMAL EFFECTS IN ROTATIONALLY INELASTIC DIFFRACTION	Technical Report		
7. AUTHOR(s)	8. PERFORMING ORGANIZATION NAME AND ADDRESS	9. CONTRACT OR GRANT NUMBER(s)	(14) TR-8407, UILU-ENG-78-2233
(10) Lynn Charles Rathbun	Coordinated Science Laboratory University of Illinois at Urbana-Champaign Urbana, Illinois 61801	10. PROGRAM ELEMENT, PROJECT, TASK AREA & WORK UNIT NUMBERS	(15) DMR-76-82088 (12) 1332
11. CONTROLLING OFFICE NAME AND ADDRESS	12. REPORT DATE		
Joint Services Electronics Program	(11) March 1979		
14. MONITORING AGENCY NAME & ADDRESS(if different from Controlling Office)	15. SECURITY CLASS. (of this report)		
	UNCLASSIFIED		
16. DISTRIBUTION STATEMENT (of this Report)	18a. DECLASSIFICATION/DOWNGRADING SCHEDULE		
Approved for public release; distribution unlimited	124		
17. DISTRIBUTION STATEMENT (of the abstract entered in Block 20, if different from Report)			
18. SUPPLEMENTARY NOTES			
19. KEY WORDS (Continue on reverse side if necessary and identify by block number)			
Surfaces Energy Exchange Molecular Beams			
20. ABSTRACT (Continue on reverse side if necessary and identify by block number)			
The scattering of the hydrogenic molecules $H_2^7$ , $D_2^7$ , and HD from vacuum cleaved MgO (001) along the [110] azimuth has been studied. A thermal beam at 300 K and 80 K was used. Particular emphasis has been placed on the rotational inelastic processes which accompany diffraction of HD. Singularities in the scattering amplitude for the rotationally inelastic events have been found to significantly effect the scattered distributions. This effect, extremal scattering, has been explained in terms of a simple mechanism, allowing → next page			

UNCLASSIFIED

SECURITY CLASSIFICATION OF THIS PAGE(When Data Entered)

20. ABSTRACT (continued)

accurate calculation of the scattering profiles and angles. The scattering of helium along both the  $\langle 110 \rangle$  and the  $\langle 100 \rangle$  azimuths has also been studied. Anomalous shifts and structure have been seen in the diffraction lobes for scattering along the  $\langle 110 \rangle$  azimuth. These are explained in terms of a wavelength dependent transition probability, calculated in the semiclassical approximation.

Accession For  
NTIS GRA&I  
DDC TAB  
Unannounced  
Justification

By \_\_\_\_\_  
Distribution/  
Availability Codes  
Avail and/or  
special

Dist	P
------	---

UNCLASSIFIED

SECURITY CLASSIFICATION OF THIS PAGE(When Data Entered)

EXTREMAL EFFECTS IN ROTATIONALLY  
INELASTIC DIFFRACTION\*

by

Lynn Charles Rathbun

\*Carried out under Grant DMR 76-82088 from the National Science Foundation.

†Supported in part by the Joint Services Electronics Program (U.S. Army,  
U.S. Navy and U.S. Air Force) under Contract DAAB-07-72-C-0259.

Reproduction in whole or in part is permitted for any purpose of the  
United States Government.

Approved for public release. Distribution unlimited.

EXTREMAL EFFECTS IN ROTATIONALLY INELASTIC DIFFRACTION

BY

LYNN CHARLES RATHBUN

B.S., The Ohio State University, 1971  
M.S., University of Illinois, 1973

THESIS

Submitted in partial fulfillment of the requirements  
for the degree of Doctor of Philosophy in Physics  
in the Graduate College of the  
University of Illinois at Urbana-Champaign, 1979

Thesis Advisor: Professor Gert Ehrlich

Urbana, Illinois

## EXTREMAL EFFECTS IN ROTATIONALLY INELASTIC DIFFRACTION

Lynn Charles Rathbun, Ph.D.  
Coordinated Science Laboratory and Department of Physics  
University of Illinois at Urbana-Champaign, 1979

The scattering of the hydrogenic molecules  $H_2$ ,  $D_2$ , and HD from vacuum cleaved MgO (001) along the [110] azimuth has been studied. A thermal beam at 300 K and 80 K was used. Particular emphasis has been placed on the rotational inelastic processes which accompany diffraction of HD. Singularities in the scattering amplitude for the rotationally inelastic events have been found to significantly effect the scattered distributions. This effect, extremal scattering, has been explained in terms of a simple mechanism, allowing accurate calculation of the scattering profiles and angles. The scattering of helium along both the [110] and the [100] azimuths has also been studied. Anomalous shifts and structure have been seen in the diffraction lobes for scattering along the [110] azimuth. These are explained in terms of a wavelength dependent transition probability, calculated in the semiclassical approximation.

## ACKNOWLEDGMENTS

I would like to thank the technical staff of the Coordinated Science Laboratory for their help in this project. The assistance of the machine shop, the glass shop, and the materials processing shop was especially valuable. I am particularly indebted to Bob Bales for his help and advice in the construction of parts of the apparatus. The cooperation of all the staff in meeting my deadlines near the end of this investigation was most appreciated.

I would like to thank Prof. Gert Ehrlich, my advisor, for his encouragement and advice during this entire project.

I would like to thank Phyllis Young and Hazel Corray for a speedy and excellent job of typing this manuscript.

The help of Brymer Chin and Don Coulman in conducting some of these experiments is gratefully acknowledged. I also thank Dr. R. G. Rowe for introducing me to this experimental apparatus and for his help when I began.

I would like to thank Profs. Flynn and Maurer for graciously accommodating this effort in the Materials Research Laboratory.

I also wish to acknowledge support from National Science Foundation under Grant DMR 76-82088.

## TABLE OF CONTENTS

CHAPTER	Page
1. INTRODUCTION .....	1
2. FUNDAMENTALS .....	7
2.1 Surface Geometry .....	7
2.2 Diffraction .....	10
2.3 Diffraction of Monoenergetic Beam .....	10
2.4 Inelastic Diffraction .....	11
2.5 Diffraction of a Thermal Beam .....	12
3. EXPERIMENTAL APPARATUS AND TECHNIQUE .....	19
3.1 Gas Handling System .....	19
3.2 Beam Source and Beam Chamber .....	23
3.3 Main Chamber .....	27
3.4 Crystal Holder and Specimens .....	30
3.5 Data Handling .....	32
3.6 Experimental Procedure .....	33
4. HELIUM SCATTERING FROM MgO (001) .....	36
4.1 Experimental Results: Helium Scattering .....	36
4.1.1 [110] Azimuth .....	36
4.1.2 [100] Azimuth .....	44
4.2 Semiclassical Calculations of Scattering .....	49
4.2.1 Review of Semiclassical Theory .....	50
4.2.2 Calculation of Diffraction Intensities .....	55
4.3 Discussion .....	68
5. SCATTERING OF HYDROGENIC MOLECULES .....	79
5.1 Experimental Results: HD .....	79
5.2 Extremal Effects .....	89
5.3 Scattering of H <sub>2</sub> and D <sub>2</sub> .....	102
5.4 Summary .....	110

CHAPTER	Page
6. DIFFUSION OF CHEMISORBED GASES .....	111
6.1 Experimental Apparatus .....	111
6.2 Proposed Experiments .....	116
REFERENCES .....	120
VITA .....	124

## CHAPTER 1

## INTRODUCTION

The interaction of gases with solid surfaces is a topic of considerable fundamental as well as technical interest. Such processes as catalytic reactions, corrosion, and oxidation begin with the collision of a gas molecule with a surface. One of the ways to study this interaction is molecular beam scattering.<sup>1</sup> In this technique, a well defined beam of atoms or molecules is allowed to collide with a crystal surface in an ultrahigh vacuum. The resulting scattering distribution contains considerable information, not only on the scattering process itself, but also on the potential and structure at the surface.

In this thesis, we investigate several aspects of the scattering of light molecules ( $H_2$ ,  $D_2$ , HD, and He) at thermal energies from magnesium oxide. The magnesium oxide surface is of interest not only as an elementary oxide, but also as a simple model system on which to study the dynamics of the gas-surface interaction. Our primary emphasis is on the elastic and inelastic diffraction of the molecular beam from the crystal surface. Of particular interest are those inelastic processes involving rotational energy, which can accompany the scattering of diatomic molecules. We will show that a new effect, extremal scattering, can cause singularities in the intensity of these inelastic rotational processes. Our chief concern is in studying those scattering processes which are unique to molecular species, that is processes involving the internal degrees of freedom. We have, however, undertaken limited studies of helium diffraction from magnesium oxide to afford a baseline for comparison with the more complex molecular scattering.

Molecular beam scattering in the gas phase, either single beam or crossed beam, has been used in chemical investigations for many years. It has yielded considerable information not only on the intermolecular potentials, but also on energy transfer and the reactivity of vibrationally, rotationally, and electronically excited species. In contrast, scattering from surfaces has not yet reached this level of sophistication. The scattering process can be completely characterized by the translational energy, the internal state, and the angular distribution of both the incident and scattered molecules. For gas phase and beam-beam scattering, these can be measured or controlled with relative ease. For instance, lasers can be used to selectively excite the internal states of the beam, and fluorescence used to monitor the state of the scattered species. Unfortunately, these techniques cannot in general be applied in studying scattering from surfaces. The requirements of ultrahigh vacuum keep the beam and scattered intensities far too low. At present, for the most part, we must be content with knowledge of the average incident energy and angle, and the scattered angles. We must to a large extent rely on interpretation of peak shapes and positions in the scattered distribution to arrive at insights about surface interactions. This restriction severely limits the type of information available on inelastic processes at surfaces; for the most part, only qualitative information is available on these processes.

Diffraction of a molecular beam was first observed by Stern and Estermann,<sup>2</sup> some 40 years ago, for H<sub>2</sub> and helium from lithium fluoride. This work confirmed the deBroglie hypothesis for atoms, coming only shortly after the diffraction of electrons was observed by Davisson and Germer.<sup>3</sup>

The experiments of Stern and co-workers also yielded information on gas-surface interactions, and provided a considerable stimulus for the early theories of surface behavior.

Despite the success of Stern and Estermann, relatively little work on the dynamics of gas-surface interactions was done using scattering methods. The development of molecular beam scattering as a surface technique had to await advances in vacuum and electronic technology. The 60's marked the beginning of modern work on the scattering of rare gases as well as hydrogenic molecules from both ionic<sup>4,5,6</sup> and metal<sup>7,8</sup> surfaces.

Much of this early work was concentrated on the diffraction of helium<sup>4,6</sup> from the alkali halide surfaces. However, diffraction of hydrogenic molecules<sup>4,6</sup> was also observed. In general, the angular distributions for D<sub>2</sub> were found to be broader than those for H<sub>2</sub>. This was believed to be the result of inelastic processes between rotational modes of the molecules and surface phonons. The rotational spacing of D<sub>2</sub> is approximately one-half that of H<sub>2</sub> and is nearer the Debye phonon energy of these surfaces. Because of the continuous energy range of the phonons, it was proposed the such inelastic processes would result in a smearing of the scattering features. There was, however, no direct evidence for this type of rotational energy exchange.

Quite another type of rotational energy transfer is possible. Logan<sup>9</sup> pointed out some time ago that rotational and translational energy could be directly interchanged in scattering at a surface. He noted that if such a process occurred, it would result in discrete peaks, shifted from the specular, containing only molecules of a given rotational state. The possibility of inelastic diffraction was not considered, however; only

transitions from the specular peak were considered. Little notice was taken of this work, as these peaks were not observed in the data available at the time.

Direct evidence for this type of process in gas-surface scattering was first obtained in 1974 by R. Grant Rowe<sup>10,11</sup> at Illinois and independently in Genoa by Boata, et al.<sup>12</sup> Rowe observed it for H<sub>2</sub>, D<sub>2</sub>, HD from MgO (001). In Genoa, H<sub>2</sub> from cold (80 K) LiF was studied. Distinct additional peaks in the scattering distribution were seen. Both experiments can be fit well to a model which postulates energy transfer between rotational and translational modes, without transfer to the surface. In simple terms, this model can be viewed as scattering of a rigid rotor from a rigid periodic surface. The phenomenon is known as rotational inelastic diffraction. The magnitude of the rotational transfer, as well as the sharpness of the resulting peaks, were striking in the early data on MgO (001) for incidence along the [100].<sup>10,11</sup> The experiments in this thesis were undertaken to extend these measurements to the [110] azimuth, and in particular to investigate the mechanism responsible for the sharpness of the rotational transitions. Singularities in the scattering probability have been found and explained. As a result, the peak shapes and positions for rotationally inelastic diffraction can now be accurately predicted. All our experimental work has been done on MgO (001). This surface is structurally similar to the LiF (001), which is more commonly used in beam scattering studies. We have found, however, that due to its higher Debye temperature, thermal inelastic scattering is considerably reduced. The diffraction features are thus more clearly defined.

Our primary emphasis is on the participation of rotational degrees of freedom in the scattering of molecules from a surface. We have also undertaken studies of helium scattering from these same surfaces, for comparison

with the more complex molecular scattering data. These data for helium, however, are not as simple to interpret as originally expected. We have therefore carried out calculations of the diffraction profiles using the semiclassical approximation.

Although several quantum mechanical formalisms<sup>13-16</sup> for gas-surface scattering have been proposed, most are cumbersome, if not impossible to use in realistic situations. The numerical calculations are extensive, and convey little feeling for the mechanics of the interaction. Theoretical chemists have in the past used semiclassical calculations for beam-beam scattering at low energies.<sup>17</sup> The semiclassical formalism is an outgrowth of the classic WKB method and has been extensively developed for scattering studies by Marcus<sup>18</sup> and by Miller.<sup>19</sup> In many cases, it gives quantitatively accurate results for intensities in gas-surface scattering.<sup>20-23</sup> The calculations are not difficult and, as a result, the formalism is ideal for fitting and interpreting experimental data. Our calculations will be done using a simple model potential, known as Steele's potential.<sup>24</sup> This model potential is sufficient, however, to allow identification of the essential features in the helium scattering data.

Although in the past, work in the area of gas-surface scattering was limited, there has been considerable activity in the last 5 years. A new generation of very sophisticated molecular beam scattering systems has been developed, with instrumentation and capabilities far surpassing those of our present apparatus. Thus, after these initial studies on MgO, we have modified our system for work in a new, relatively unexplored area. We have developed a method of using the unique capabilities of the molecular beam

to study surface diffusion of gaseous species on crystal surfaces, about which only little is known. This new technique will be discussed briefly in Chapter 6.

## CHAPTER 2

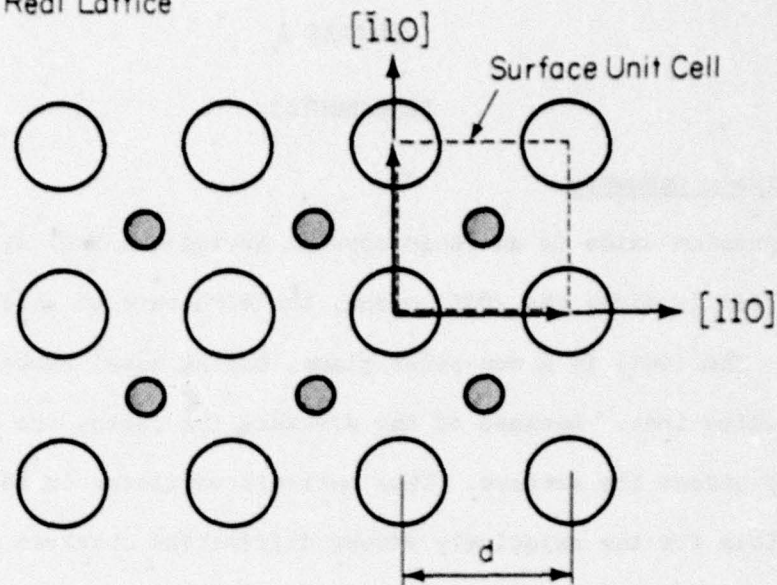
## FUNDAMENTALS

2.1 Surface Geometry

Magnesium oxide is an ionic crystal having the NaCl structure. It cleaves easily along the (001) plane, the structure of which is shown in Fig. 1. The (001) is a non-polar plane, having equal numbers of positive and negative ions. Because of the discrete ion cores, the potential varies strongly across the surface. This periodic variation in the potential is responsible for the relatively strong diffraction observed from these surfaces. The surface unit cell, shown in Fig. 1, is 2.97 Å on a side and is rotated 45° from the bulk unit cell. The surface reciprocal lattice vectors, also shown in Fig. 1, thus lie along the [110] directions. In these studies, we have, for the most part, investigated scattering along the [110] incident azimuth. In other words, the surface component of the incident wavevector lies along the [110] direction, the direction between nearest like neighbors.

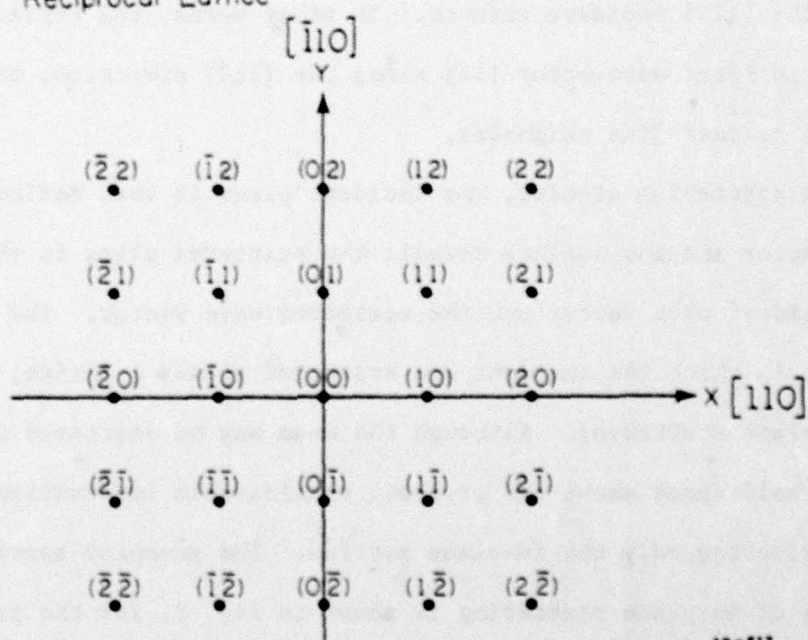
In scattering studies, the incident plane is that defined by the incident wave vector and the surface normal; the scattered plane is that defined by the incident wave vector and the scattered wave vector. The simplest case is that in which the incident and scattered planes coincide; this is known as in-plane scattering. Although the beam may be scattered into any portion of the half-space above the crystal, considerable information can be gained by considering only the in-plane portion. The geometry appropriate to these studies of in-plane scattering is shown in Fig. 2, for the particular case of incidence along the [110] azimuth. The incident and scattered angles, measured up from the surface, are denoted by  $\theta_0$  and  $\theta$  respectively; the

## Real Lattice



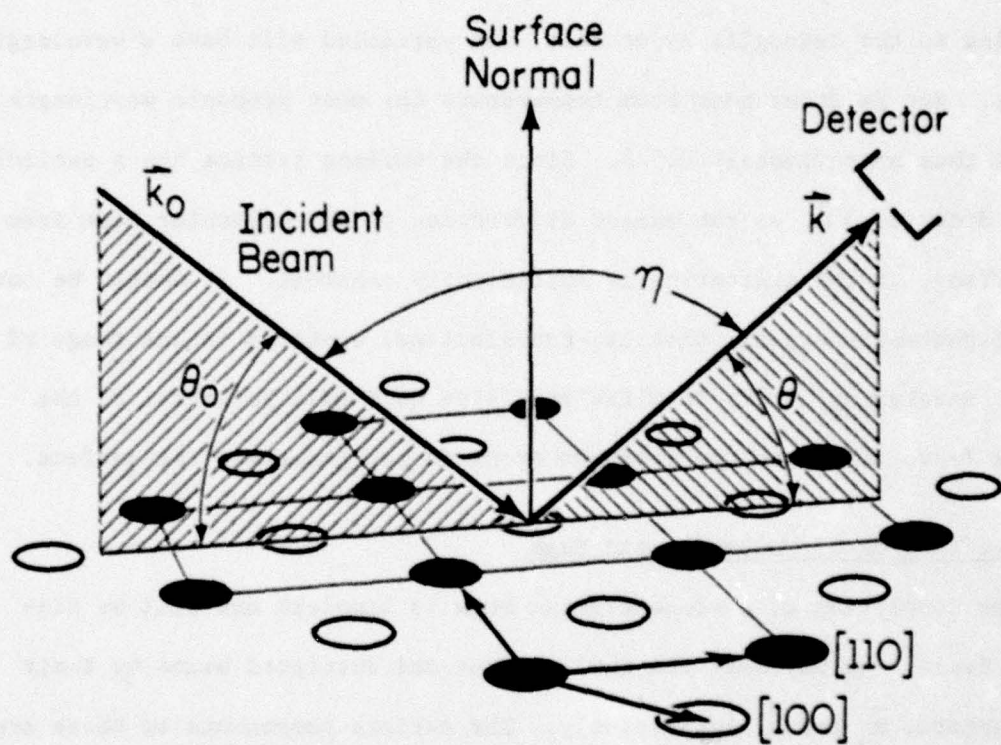
AP-517

## Reciprocal Lattice



AP-517

Fig. 1. The  $(001)$  plane of MgO and the associated reciprocal lattice.  
Surface unit cell is  $2.97 \text{ \AA}$  on a side.



AP-528

Fig. 2. Scattering geometry.  $\vec{k}_0$  and  $\vec{k}$  are incident and scattered wave vectors, respectively. The particular case of the [110] incident azimuth is shown.  $\theta_0$  and  $\theta$  are the incident and scattered angles, measured from the surface.

experimentally measured angle  $\eta$ , the angle between the incident and scattered beams, is therefore given by

$$\eta = 180 - \theta_0 - \theta. \quad (1)$$

## 2.2 Diffraction

In our scattering experiments, we are for the most part concerned with the diffraction of the molecular beam from the periodic surface potential. According to the deBroglie hypothesis, the particles will have a wavelength  $\lambda = h/p$ . For He atoms near room temperature the most probable wavelength,  $\lambda_{mp}$ , is thus approximately 0.5 Å. Since the surface lattice has a periodicity on the order of 3 Å, we can expect diffraction of the molecular beam from the surface, if the scattering is sufficiently coherent. It should be noted that at thermal energies, that is, translational energies in the range of 40 meV, scattering occurs from the repulsive hard wall potential of the surface layer of atoms; the incident atoms do not penetrate the surface.

## 2.3 Diffraction of Monoenergetic Beam

The scattering of a monoenergetic beam is simplest and will be discussed first. We may describe the incident and scattered beams by their wave vectors,  $\vec{k}_0$  and  $\vec{k}$ , respectively. The surface components of these are denoted by  $\vec{k}_0$  and  $\vec{k}$ , that is

$$\vec{k}_0 = (\vec{k}_0, \vec{k}_{0z}). \quad (2)$$

The Laue condition for a 2-D potential is thus

$$\vec{k} = \vec{k}_0 + \vec{G}_{nm}, \quad (3)$$

where  $\vec{G}_{nm}$  is a surface reciprocal lattice vector. For a square symmetric lattice,  $\vec{G}_{nm} = \frac{2\pi}{d} n\hat{x} + \frac{2\pi}{d} m\hat{y}$ . This condition, along with conservation

of energy  $k_o^2 = k^2$ , uniquely determines the positions of the diffracted peaks. For the particular case of in-plane scattering, we have

$$\cos \theta = \cos \theta_o + \frac{n\lambda}{d} . \quad (4)$$

The scattering distribution thus consists of a specular peak, that is the (0,0) diffraction peak, surrounded by a series of discrete diffraction peaks. This is the situation appropriate to the scattering of low energy helium atoms from an ionic surface.

#### 2.4 Inelastic Diffraction

In addition to elastic scattering, several types of inelastic events may occur. A molecule can exchange energy from either translational or internal modes with the surface by coupling to phonons. At the energies we are considering, electronic and vibrational excitations are forbidden; however, rotational degrees of freedom, having energies in the range 10 to 100 meV, can freely participate. Another type of inelastic event involves direct transfer of energy between translation and internal modes, without energy exchange with the surface. If this occurs during diffraction, we have rotationally inelastic diffraction.<sup>10-12</sup> For this we have

$$k^2 = k_o^2 + \frac{2M \Delta E}{\hbar^2} \quad (5a)$$

$$\vec{k} = \vec{k}_o + \vec{G}_{nm} , \quad (5b)$$

where  $\Delta E$  is the energy transferred from rotation to translation. Since the rotational energy levels are quantized, new discrete inelastic peaks are expected. Transitions in which energy is transferred from rotation to translation ( $\Delta E > 0$ ) are called gain transitions; if energy is transferred

from translation ( $\Delta E < 0$ ) they are called loss transitions. Confining ourselves again to in-plane scattering, the peak positions are given by

$$\cos \theta = \frac{\lambda}{\lambda_0} (\cos \theta_0 + n \lambda_0 / d) \quad (6a)$$

where

$$\lambda/\lambda_0 = [1 + 2\Delta E M_g \lambda_0^2 / h^2]^{-\frac{1}{2}}. \quad (6b)$$

For the symmetric rotors  $H_2$  and  $D_2$ , symmetry forbids transitions between even and odd rotational states, i.e., there is no ortho-para conversion.<sup>25</sup> The lowest allowed transitions are those in which the rotational quantum number  $J$  changes from  $0 \rightarrow 2$ , followed by  $1 \rightarrow 3$ , then  $2 \rightarrow 4$ . For HD, however, there is no such selection rule. Transitions between adjacent rotational states are allowed. The spacings of the rotational transitions for the hydrogenic molecules are given in Tables 1-3, along with the equilibrium population  $P(J_i)$ , of the initial state,  $J_i$ , at two beam temperatures, 300 K and 80 K. The transitions are labeled by  $I = \pm 1, \pm 2, \pm 3$  for gain (+) and loss (-) transitions, the integer denoting the relative magnitude of the energy change in the transition. An inelastic diffraction peak is thus fully described by  $(n, m) \pm I$ . The energy change in the lowest allowed transition for HD is seen to be 255 cal/mole, compared to 512 cal/mole and 1012 cal/mole for  $D_2$  and  $H_2$  respectively. By comparison, the mean translational energy of these molecules in a beam at 300 K is 1190 cal/mole. Considerable changes in the positions of the diffracted peaks can therefore be expected due to these rotational transitions.

## 2.5 Diffraction of a Thermal Beam

We have discussed the diffraction of a monoenergetic beam of molecules. All beams, however, have a distribution of velocities. A fairly mono-

TABLE 1  
Rotational energies and allowed rotational transitions for HD.

Rotational Energy Levels (HD)

J	$E_{ROT}$
0	0.0 cal/mole
1	255.06
2	763.44
3	1521.65
4	2524.6

Allowed Transitions (HD)

I	$J_i \rightarrow J_f$	$\Delta E(I)$ cal/mole	P( $J_i$ ) 300 K	P( $J_i$ ) 80 K
+1	$1 \rightarrow 0$	+ 255.06	0.39	0.37
+2	$2 \rightarrow 1$	+ 508.38	0.28	0.025
+3	$3 \rightarrow 2$	+ 758.21	0.11	---
-1	$0 \rightarrow 1$	- 255.06	0.20	0.61
-2	$1 \rightarrow 2$	- 508.38	0.39	0.37
-3	$2 \rightarrow 3$	- 758.21	0.27	0.025
-4	$3 \rightarrow 4$	-1002.95	0.11	0.025

TABLE 2  
Rotational energies and allowed rotational transitions for D<sub>2</sub>.

Rotational Energy Levels (H<sub>2</sub>)

J	E <sub>ROT</sub>
0	0.0 cal/mole
1	338.68
2	1012.93
3	2016.64
4	3340.89

Allowed Transitions (H<sub>2</sub>)

I	J <sub>i</sub> → J <sub>f</sub>	ΔE cal/mole	P(J <sub>i</sub> ) 300 K	P(J <sub>i</sub> ) 80 K
+1	2 → 0	+ 1012	0.117	0.002
+2	3 → 1	+ 1678	0.091	---
+3	4 → 2	+ 2327	0.004	---
-1	0 → 2	- 1012	0.128	0.248
-2	1 → 3	- 1678	0.658	0.750
-3	2 → 4	- 2327	0.117	0.002

TABLE 3

Rotational energies and allowed rotational transitions for H<sub>2</sub>.

Rotational Energy Levels (D<sub>2</sub>)

J	E <sub>ROT</sub>
0	0.0 cal/mole
1	170.8
2	511.7
3	1021.1
4	1696.6

Allowed Transitions (D<sub>2</sub>)

I	J <sub>i</sub> → J <sub>f</sub>	ΔE(I) cal/mole	P(J <sub>i</sub> ) 300 K	P(J <sub>i</sub> ) 80 K
+1	2 → 0	+512	0.38	0.111
+2	3 → 1	+850	0.11	0.003
+3	4 → 2	+1185	0.09	---
-1	0 → 2	-512	0.181	0.554
-2	1 → 3	-850	0.204	0.329
-3	2 → 4	-1185	0.38	0.111
-4	3 → 5	-1514	0.01	0.003

energetic beam of neutrals can be obtained by aerodynamic expansion from high pressure, a so-called nozzle beam.<sup>26,27</sup> With such a source, velocity half-widths on the order of 1% can be obtained from room temperature beams. A much broader velocity distribution is obtained in a beam formed by effusion.<sup>28,29</sup> Molecules are allowed to effuse from a low pressure source into vacuum through a small hole or channel. If the mean free path in the gas behind the source is much longer than the diameter of the hole, the distribution of velocities in the beam will reflect the equilibrium velocity distribution of gas in the source. The beam will have a modified Maxwell-Boltzman distribution, given by

$$g(v)dv = 2\left(\frac{M}{2kT}\right)^{\frac{1}{2}} v^3 \exp\left(-\frac{Mv^2}{2kT}\right), \quad (7)$$

where T is the temperature of the source. The mean translational energy of the beam molecules is  $2kT$ . Recalling that  $\lambda = h/Mv$ , the wavelengths in the beam are distributed according to

$$f(\lambda)d\lambda = -2\left(\frac{\lambda}{\lambda_0}\right)^5 \exp\left(-\frac{\lambda^2}{\lambda_0^2}\right) d\left(\frac{\lambda}{\lambda_0}\right), \quad (8)$$

where  $\lambda_0^2 = \frac{h^2}{2kTM_g}$ . The most probable wavelength  $\lambda_{mp}$  is thus given by

$$\lambda_{mp} = \sqrt{\frac{h^2}{5kTM_g}}. \quad (9)$$

The diffraction of a molecular beam from the 2-D surface potential is in many ways analogous to the diffraction of X-rays from the bulk crystal. For the latter we have the 3-D Laue condition for constructive interference of the scattered waves,

$$\vec{k} = \vec{k}_o + \vec{G}_{nm} . \quad (10)$$

For a given set of incident angles, only certain wavelengths will diffract; all others destructively interfere. Because of this, one can do X-ray diffraction from a crystal with a broad wavelength source and still get sharp diffraction spots. The crystal filters out the other wavelengths.

The diffraction condition in 2-D is much less strict. Only the two equations  $\vec{k} = \vec{k}_o + \vec{G}_{nm}$  and conservation of energy must be satisfied. As a result, all wavelengths will be diffracted from the surface, but each will be scattered to a different angle. For a beam with a narrow velocity distribution, this presents no problem. For a beam with a significant wavelength distribution, as in Eq. (8), the situation is more complex. Broad diffraction peaks are then expected, reflecting the wavelength distribution of the incident beam. This is shown schematically in Fig. 3, where calculated profiles for typical  $(\pm 1, 0)$  diffraction peaks are shown, assuming that the diffraction probability is independent of wavelength. It should be noted that even in this simple case, the peak does not correspond to the most probable wavelength, or to any other simple characteristic of the beam. The wavelength distribution, the transition probability, and a geometrical factor,  $d\lambda/d\theta$ , all interact to determine the peak of the scattered distribution. The situation is even more complex for inelastic scattering. It is precisely this geometrical factor which will have a significant effect on the detectability of the rotational inelastic events we wish to study. This will be fully investigated in Chapter 5.

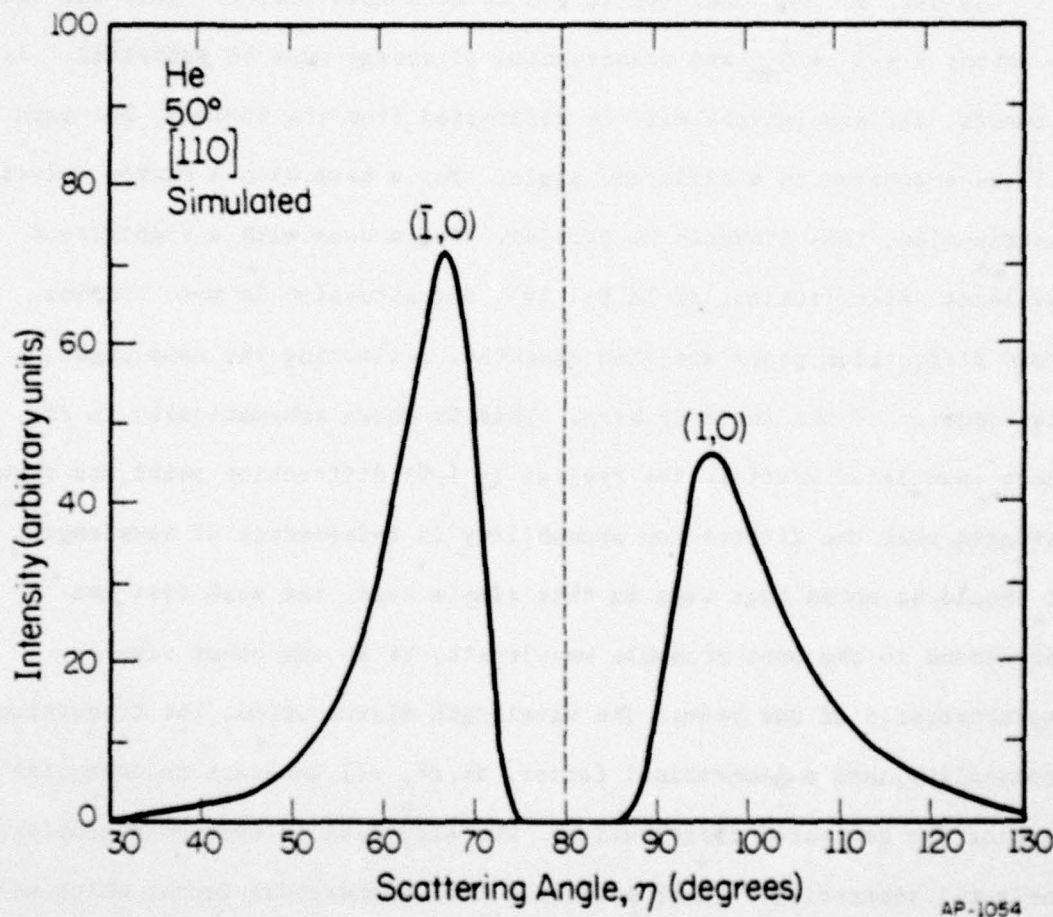


Fig. 3. Calculated first order helium diffraction peaks for thermal velocity distribution at 300 K, assuming constant diffraction probability. The broad peaks reflect the broad initial wavelength distribution.

## CHAPTER 3

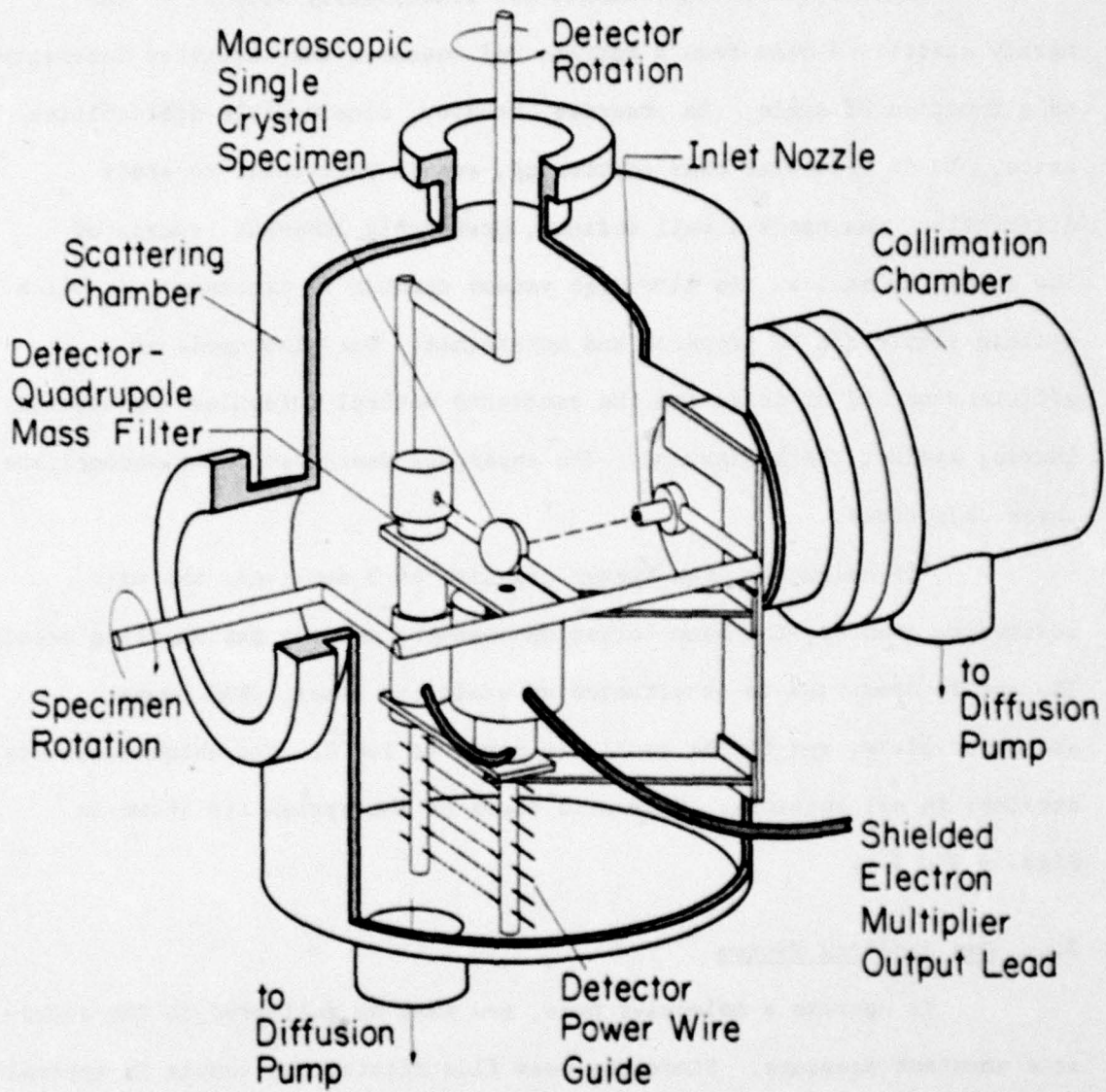
## EXPERIMENTAL APPARATUS AND TECHNIQUE

Molecular beam experiments are conceptually simple.<sup>30</sup> One merely scatters a beam from a surface and measures the scattered intensity as a function of angle. In practice, however, considerable difficulties arise. To do molecular beam scattering, and in particular to study diffraction, one needs a well defined, preferably coherent, source of low energy molecules. An ultrahigh vacuum chamber is necessary, in which a clean sample can be prepared and maintained. One also needs an efficient method of detecting the scattered neutral molecules and discriminating against the background. The apparatus described below accomplishes these objectives.

Our molecular beam system consists of 3 sections; the main scattering chamber, the beam formation chamber, and the gas handling section. The entire apparatus is constructed of stainless steel, OFHC copper, and pyrex glass, and can be routinely baked to 300°C. Ultrahigh vacuum is attained in all sections. Schematic views of the system are shown in Figs. 4 and 5.

### 3.1 Gas Handling System

To operate a molecular beam, gas must be delivered to the source at a constant pressure. Since the beam flux hitting the sample is typically a monolayer/sec, even small amounts of impurities could cause contamination. A system is therefore required both to purify the gas and establish a constant pressure. A schematic of the apparatus built for this purpose is shown in Fig. 6. This section is constructed entirely of pyrex, with



Scattering Chamber Schematic

Fig. 4. Cut-away schematic view of main scattering chamber.

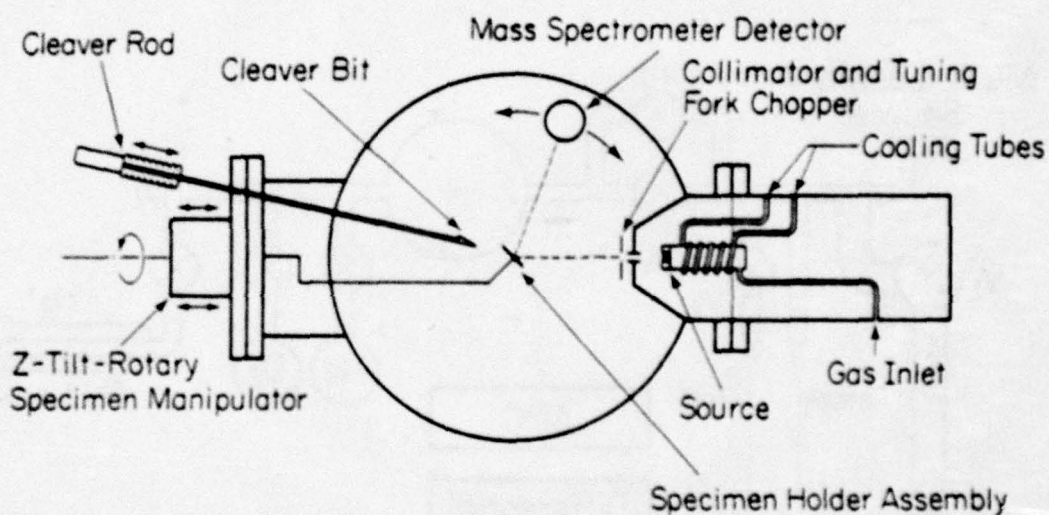
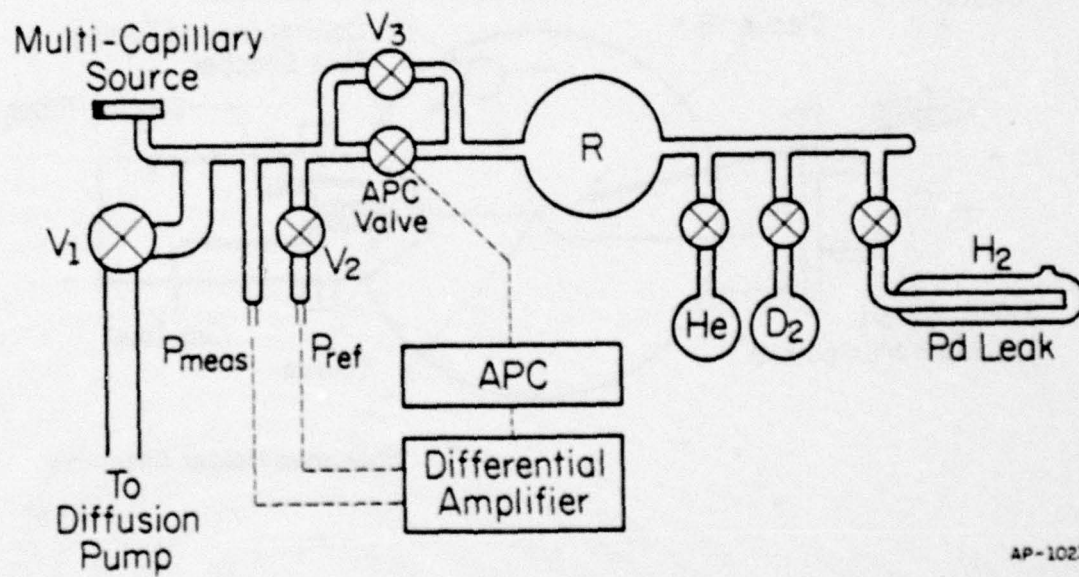


Fig. 5. Top view schematic of Molecular Beam Scattering System.

30



AP-1023

Fig. 6. Diagram of gas handling system with automatic pressure control (APC).  $P_{meas}$  and  $P_{ref}$  are the measuring and reference (dummy) Pirani gauges, respectively. Gas is stored in the reservoir, R.

metal sealed UHV valves (Granville-Phillips, type C and series 204) and is evacuated by a mercury diffusion pump (Kontes-Martin). Deuterium and helium are drawn from analyzed reagent grade flasks (Airco). H<sub>2</sub> is obtained by diffusion through a palladium leak (K & B Apparatus, Schenectady, NY). HD is made by equilibrating a 50/50 H<sub>2</sub>-D<sub>2</sub> mixture over a hot tungsten filament, resulting in a mixture of H<sub>2</sub>, D<sub>2</sub>, and HD. These gases are stored in the reservoir at a pressure of several hundred torr.

For proper operation, the source requires a constant pressure of about 1 torr. It is necessary to control this pressure over periods of hours to  $\pm$  1%. This is accomplished by a servo valve (Granville-Phillips, Series 216) using two Pirani gauges (LKB, 3596) as a differential pressure sensor. One Pirani gauge is blanked off at the desired pressure. The other measures the pressure delivered to the source. The outputs of the two are compared using the bridge circuit shown in Fig. 7. This arrangement is necessary to compensate for fluctuations in room temperature, which severely affect the reading of any heat conductivity gauge, such as a Pirani.

### 3.2 Beam Source and Beam Chamber

The molecular beam is formed by effusion from a multicapillary array (Brunswick Corp., Collimated Hole Structure). To form a beam by effusion, it is necessary to operate in the region where the mean free path, L<sub>mfp</sub>, is greater than d, the diameter of the channel. Because of this restriction, more intensity can be achieved by using an array of small channels rather than a large channel. This is the rationale behind the multicapillary source.<sup>31</sup> The source consists of about 100 parallel

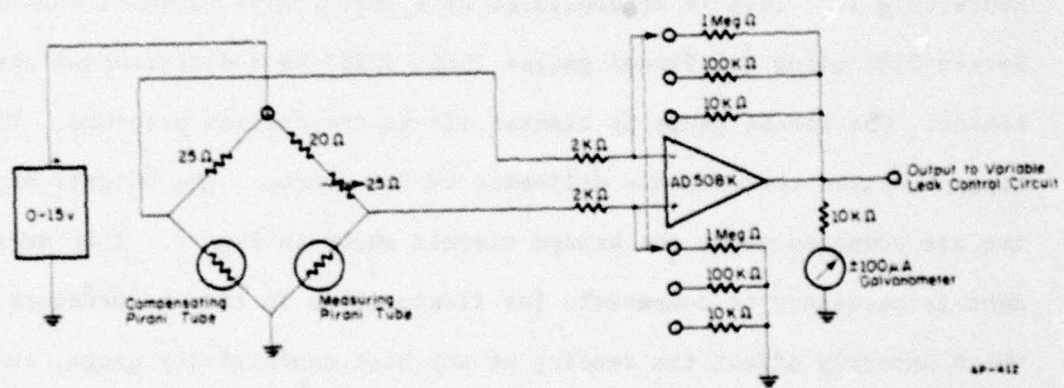


Fig. 7. Schematic diagram of differential Pirani bridge circuit.

channels, each 3 mm long and .05 mm in diameter, through a stainless steel disc. The channels are close-packed in a circular array about 1 mm in diameter. A diagram of the source assembly is shown in Fig. 8. The source disc is brazed in the end of the source tube, forming a small effusion chamber. Gas is supplied to this chamber at constant pressure by the gas handling system previously described. The source tube can be cooled to change the velocity distribution of the beam. This is accomplished by flowing cold nitrogen gas through the coils around the source tube. A window is provided at the rear of the source tube for alignment of the source and target with a laser.

The molecular beam for our experiments is formed by gas effusing through the source channels into the vacuum. It thus has a velocity distribution given by Eqn. (7) and is peaked in the forward direction. A collimator hole, 0.7 mm in diameter, approximately 1 cm downstream from the source, allows only a small portion of these molecules to enter the main scattering chamber. The rest of the gas is rejected back into the beam chamber, where it is removed by differential pumping with an ultra-high vacuum diffusion pump stack, (Edwards High Vacuum, UHVM2A and EM2). When the beam is on, the pressure in the beam chamber is typically  $10^{-6}$  torr. Typically, the beam flux at the sample is  $10^{13}$ /sec into a spot 1 mm in diameter.

As previously discussed, this beam has a broad velocity distribution. The alternative source, an aerodynamic nozzle,<sup>26,27</sup> is characterized by a much narrower velocity distribution. However, this source is somewhat more difficult to fabricate and operate than a conventional effusion source; moreover, the beam is more prone to contamination,

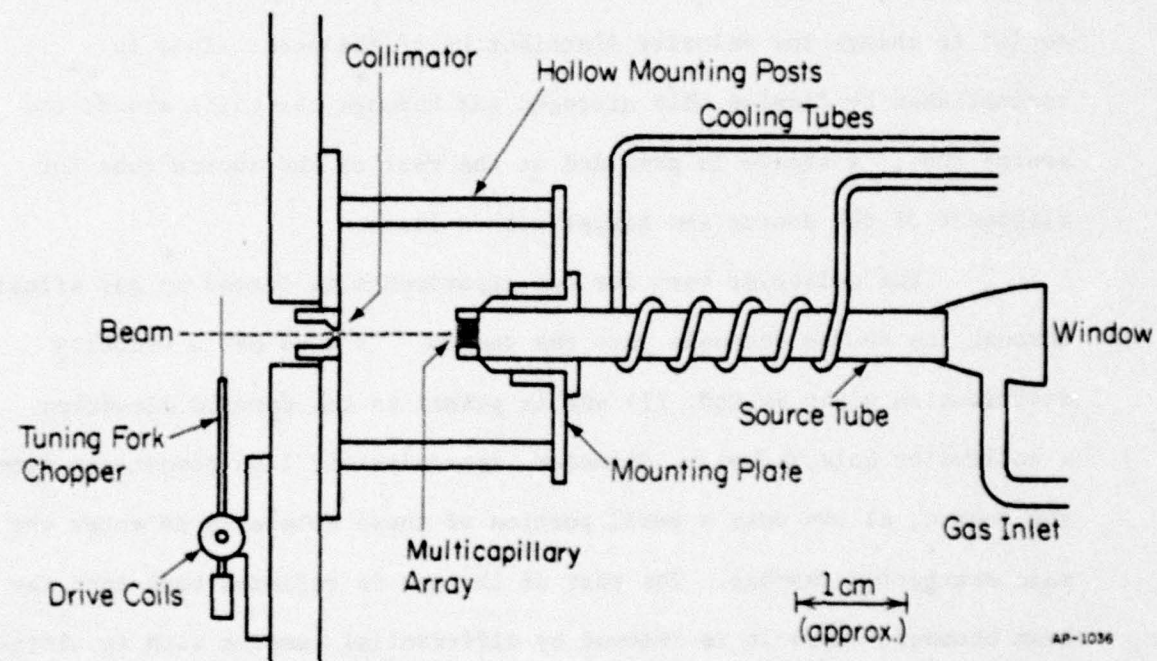


Fig. 8. Schematic diagram of molecular beam source assembly.

due to the high pressure ( $\sim 2\text{-}10$  atm) at which it is operated. Several stages of high speed differential pumping would be needed to handle the large gas loads which accompany this source. Furthermore, since we are interested in studying the participation of the internal degrees of freedom of molecules in the scattering process, the nozzle sources have a serious disadvantage. The rapid expansion into vacuum from high pressure lowers the random velocities, that is the translational temperature, of the molecules. This energy goes into uniform translation of the bulk gas, resulting in a fairly monoenergetic beam. In the same manner, the internal degrees of freedom are to some extent frozen out in the expansion. The resulting internal energy distribution is cold<sup>32,33</sup> and is not well characterized. In contrast, the internal energy distribution of an effusive beam is well established at all temperatures. For these reasons, there appeared to be some advantage to using an effusive source for these studies.

In order to facilitate signal processing, the beam is chopped by a 25 Hz magnetic tuning fork (American Time Products, L40C) as it enters the main chamber. This allows the use of lock-in detection of the scattered signal. The tuned feedback amplifier,<sup>34</sup> shown in Fig. 9, drives the chopper at its resonant frequency and provides a reference signal for the lock-in amplifier.

### 3.3 Main Chamber

The scattering chamber consists of a stainless steel bell jar 30 cm in diameter. It is evacuated by two separate pumping systems. Main pumping is by a mercury diffusion pump stack (Edwards High Vacuum, UHVM2A and EM2, having a pumping speed of 70 liters/sec for air.

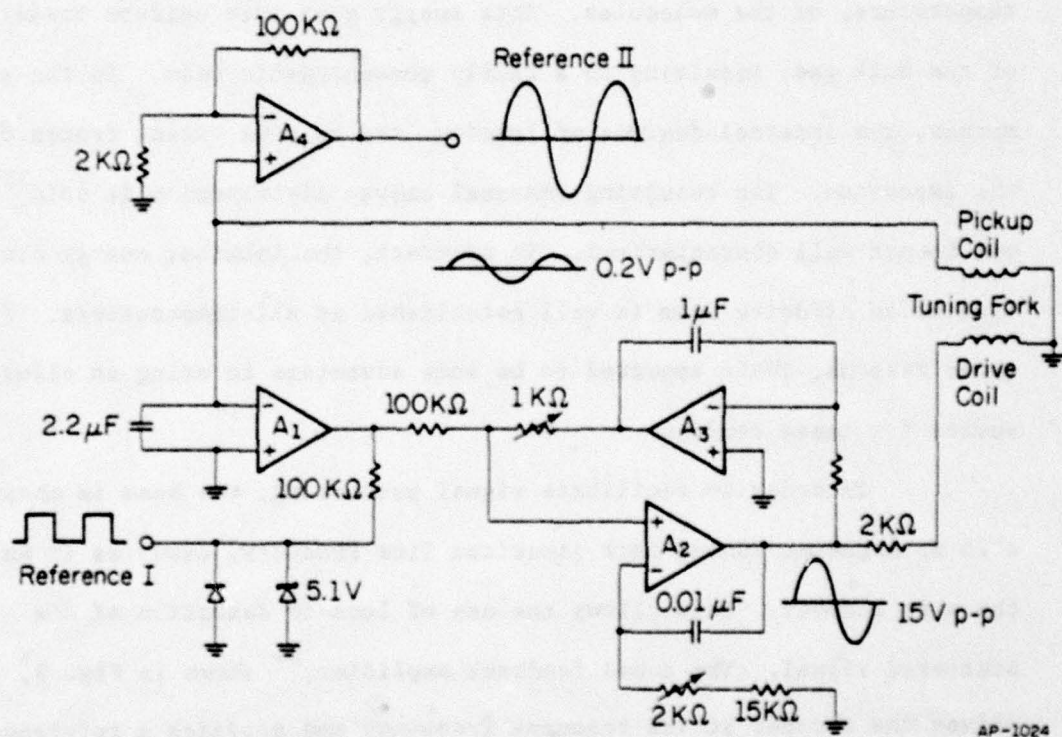


Fig. 9. Schematic diagram of drive circuit for tuning fork chopper.

AP-1024

When the molecular beam is turned on, additional pumping is required to maintain a good vacuum and a clean sample. For this reason, a liquid helium cryo-sorption pump (Excalibur CVV-2010) is built into the bottom of the scattering chamber. When cooled to 4 K, it provides an additional pumping speed of 2000 liters/sec for helium. With this pump activated, the base pressure is below  $10^{-10}$  torr, and remains below  $10^{-9}$  torr with the beam on.

The molecules scattered from the crystal are detected by a quadrupole mass spectrometer (Extranuclear 324-9). This allows scattering experiments with mixed isotopes such as HD, which cannot be prepared in pure form. The mass spectrometer rotates in an arc around the sample. The entrance aperture of this detector determines the angular resolution of our experiments. This aperture may be adjusted from the outside during a run to be either 1.6 or 3.25 degrees. The rotation of the detector is controlled, from the outside, by a stepping motor through a bellows sealed rotary feedthrough. Since the quadrupole mass filter can only analyze ions, the neutral molecules from the beam must first be ionized. This is accomplished with an electron impact ionizer atop the mass filter. Molecules in the ionization region are ionized by a beam of low energy electrons and then electrostatically focused into the quadrupole filter section. A 21 stage Cu-Be electron multiplier (EMI, Ltd.) at the exit of the mass filter amplifies the ion signal by a factor of approximately  $10^5$  before it is fed through the vacuum envelope.

### 3.4 Crystal Holder and Specimens

The sample holder is shown in Fig. 10. The crystal (A) is mounted in a square hole within a stainless steel block (B) in which it is free to slide. It is held in place by small spring loaded stainless steel balls. This allows the crystal to be moved forward in the block for multiple cleavages. Translation is accomplished by pushing with the cleaver rod (C). The entire crystal block is mounted inside a ball bearing (D), with the face of the crystal flush with the surface of the race. This allows the crystal to be rotated about the surface normal, so that the incident azimuth can be changed. This degree of freedom, however, cannot be accurately measured. Stops are therefore provided so that the [110] and [100] azimuths are reproducible.

The entire assembly is again mounted on two small ball bearings (E), to allow rotation about an axis in the plane of the sample. In this manner,  $\theta_0$ , the incident angle, can be adjusted by pushing the cleaver rod. The assembly is held at a fixed incident angle by pressure from small spring loaded balls.

The crystal holder assembly is mounted on a bellows sealed rotary feedthrough (F), coaxial with the beam. By rotation of the sample holder about the beam axis, the surface normal can be rotated out of the horizontal plane. This is essentially a rotation, about the beam, of the crystal coordinate system with respect to the laboratory system. This degree of rotational freedom allows us to bring any scattered vector into the horizontal plane without changing the incident conditions in the crystal coordinate system. In this manner, much of the scattered solid angle can be scanned, while avoiding the difficult task of moving

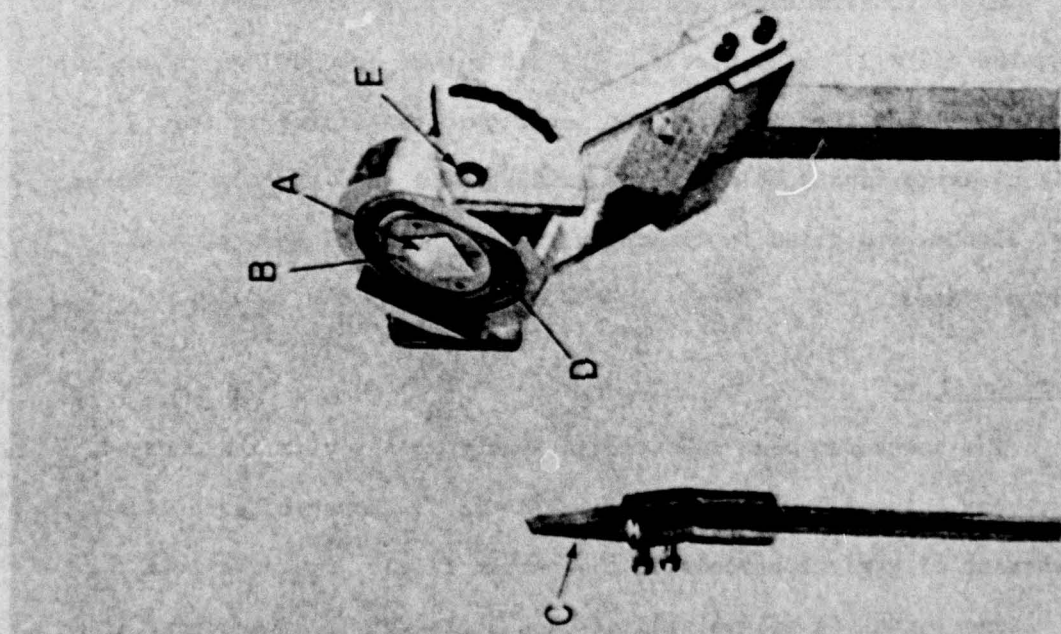


Fig. 10. Crystal holder and manipulator. MgO crystal (A). Stainless steel block (B). Cleaver rod and cleaver bit (C). Large bore bearing (D) to allow rotation around surface normal. Bearing (E) for  $\theta_i$  rotation. Rotary feedthrough (F).

the plane of detector rotation.

For meaningful results, it is necessary to do experiments on a clean surface. It has been standard procedure in beam scattering experiments to cleave the crystal external to the system,<sup>4-6,35,36</sup> and lightly heat it under vacuum to obtain a clean surface. This procedure is at best shaky. The true state of such surfaces is still open to considerable controversy.<sup>37,38</sup> Furthermore, there is recent evidence that the MgO (001) surface undergoes an irreversible reconstruction upon heating to greater than 450 K.<sup>39</sup> To avoid such problems the crystal in our experiments is cleaved *in situ* along the (001) plane. Although this is the preferred and rigorously clean approach, it severely limits flexibility. Heating and cooling the crystal are for the most part precluded. As a result, these experiments are conducted with the surface at room temperature, resulting in an unfortunately large background of thermal inelastic events.

The magnesium oxide specimens were obtained from the Norton Co., in the form of 1 × 1 × 5 cm blocks. The sides were ground down to uniform size, using silicon carbide paper, to permit smooth sliding in the multiple cleavage sample holder. The samples were then thoroughly washed in ethyl alcohol and dried in flowing nitrogen, prior to insertion in the vacuum system.

### 3.5 Data Handling

The scattered beam is detected synchronously with the chopped incident beam using a lock-in amplifier (PAR 186). However, even with a time constant of several seconds on the output filter, the signal is noisy. Since signal is accumulated at each angle for 10-30 seconds, it

would be desirable to integrate the signal over this entire time interval to reduce the noise. To accomplish this, and to control the experiment, a signal integrator and digitizer was constructed. A function block diagram of this instrument is shown in Fig. 11. The main section of this instrument is a gated integrator. After the detector is in its desired position, the integrator is enabled. It integrates the output of the lock-in for a preset interval while the detector sits at one position. This period may be adjusted from 5-60 seconds. At the end of an interval, the input to the integrator is disabled, and the accumulated signal is digitized. Simultaneously, the angular position of the detector, as measured with a potentiometer, is digitized. Both pieces of information are then printed onto a teletype and punched on paper tape for later computer analysis. Finally, the integrator is reset to zero and the detector is automatically stepped  $0.45^\circ$ . The sequence then begins again with the input of the integrator being enabled. This sequence continues under digital control until the entire scan is completed.

### 3.6 Experimental Procedure

To do an experiment, it is first necessary to obtain an ultrahigh vacuum. The entire system is baked to  $300^\circ\text{C}$  for approximately 12 hours. After about 24 hours, the system has cooled to room temperature and the vacuum is typically  $5 \times 10^{-10}$  torr. At this point, however, there is still considerable gas coming from the large surface area of the porous adsorbent in the cryopump. Upon cooling the cryopump to  $\text{LN}_2$  temperature, it ceases to be a source and begins to pump. The pressure goes to  $2 \times 10^{-10}$  torr. Once the pump is cooled to liquid helium temperature the pressure drops below  $10^{-10}$  torr. By periodically refilling the helium Dewar

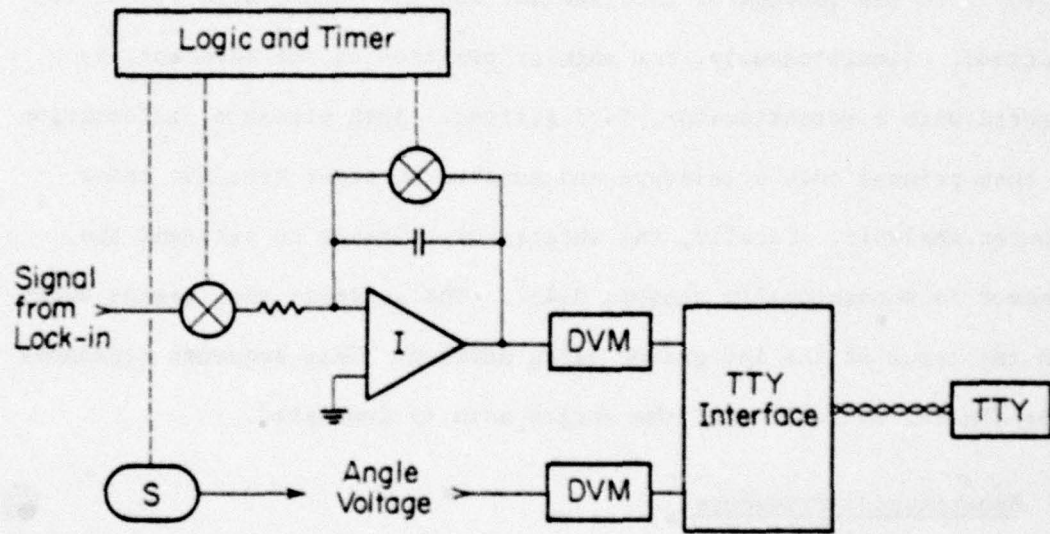


Fig. 11. Functional block diagram of automated signal integrator and digitizer showing integrator amplifier (I), stepping motor and angle indicator (S), and digital volt meters (DVM).

(at the rate of 20 liters every 4 days) it is possible to keep the system below  $10^{-10}$  torr for several months. The system is now ready for an experiment.

The surfaces we are interested in are formed by cleavage in ultrahigh vacuum. The cleaving bit is a  $30^{\circ}$  wedge ground from tool steel. It is connected to the outside by a flexible metal bellows coupling. A sharp tap of the bit against the side of the crystal is sufficient to produce a clean, relatively flat surface which gives reproducible data. The surfaces obtained are quite immune to contamination. Nonetheless, for the most part, a new surface was cleaved every day. This presented no problem as the crystal could be advanced along its length in the holder, permitting as many as 15 cleavages per crystal.

To proceed with a run, the pressure controller in the gas handling system is activated to provide a constant beam intensity. The intensity of the beam can be measured with the scattering detector by moving the sample out of the way. The sample is then returned to the center of the vacuum system, and the incident angle and azimuth are set. The data handling system can then be activated, and the experiment runs automatically, scanning the region from  $50^{\circ}$  to  $180^{\circ}$  from the beam. We are constrained by the geometry of the vacuum system from measuring the scattered flux at less than  $50^{\circ}$  from the beam. When a run is completed, in approximately 30 minutes, new incident conditions are set and another run begins. The data collected on paper tape are then fed into a separate computer and plots are generated.

## CHAPTER 4

## HELIUM SCATTERING FROM MgO (001)

4.1 Experimental Results: Helium Scattering

As a background for our examination of molecular diffraction, we will present data for the scattering of He from the (001) plane of MgO. Both the [110] and the [100] incident azimuths have been investigated. Only the in-plane scattering data are presented, as these are the ones of interest for comparison with our subsequent studies on hydrogen. All of the data in this section were taken with both the beam and the surface at 300 K. At these low energies, internal excitation of the helium atoms is forbidden. The atoms should scatter as structureless particles. This will provide us with a reference to compare with the scattering of hydrogenic molecules, where we expect the internal degrees of freedom to be important.

4.1.1 [110] Azimuth

Data for several incident angles along the [100] azimuth are shown in Figs. 12-17. The differential scattering intensity is plotted against the angle  $\eta$  between the incident beam and the detector. As previously mentioned, only that portion of the distribution scattered to  $\eta > 50^\circ$  is experimentally accessible. All data in this thesis have been normalized to a direct beam intensity of 1000 units. Measurements were taken at 0.5 degree intervals. In the figures, every data point is marked by a "+", with a line connecting each point. To reduce the noise to a low level, all data were collected using the integrator described in Chapter 3.

It is apparent that the in-plane distribution consist of a strong specular peak, flanked by broad diffraction lobes on either side. Recall that the specular peak occurs at  $\eta = 180 - 2\theta_0$ . Positive order diffraction

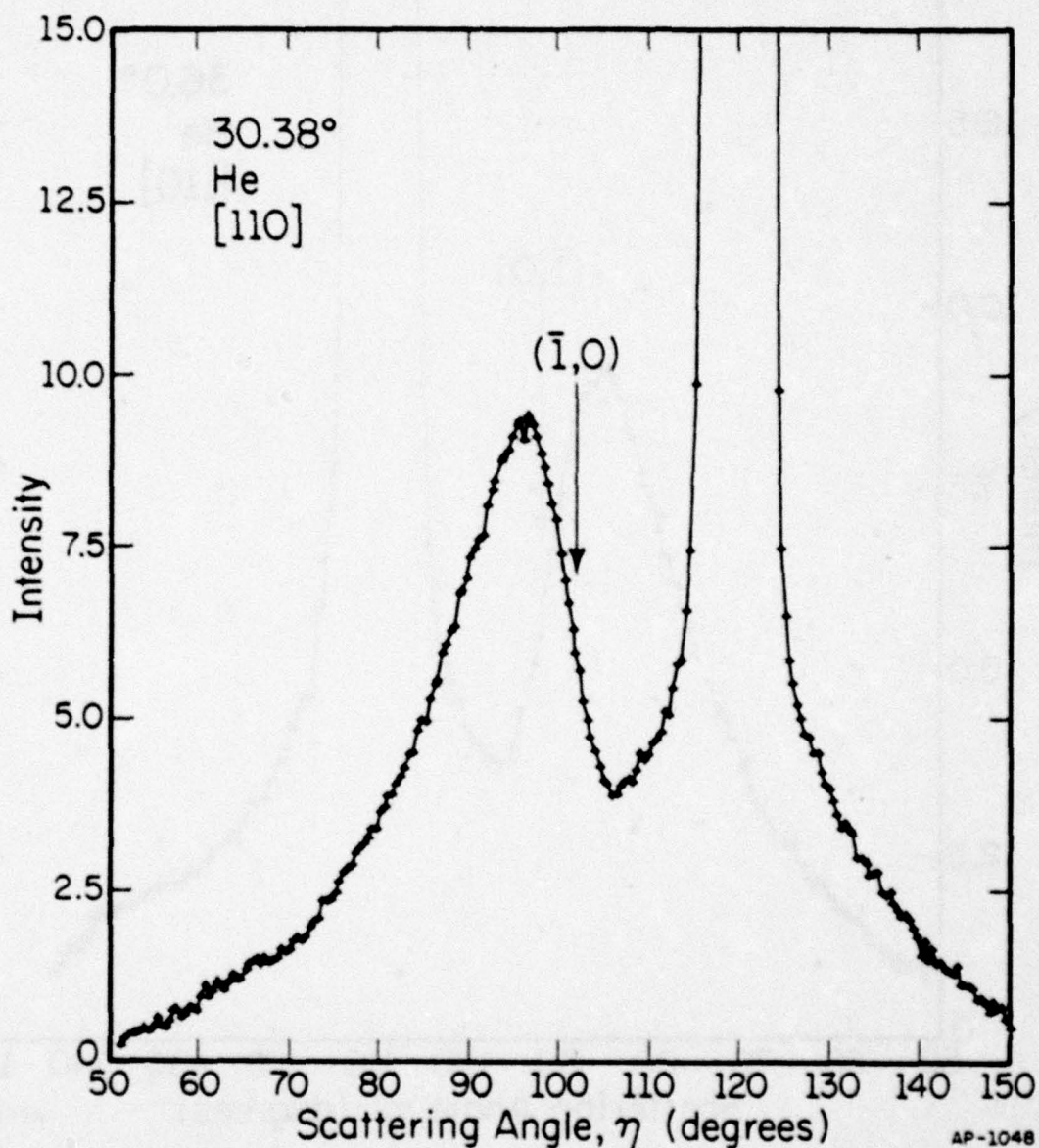


Fig. 12. Helium scattering from MgO (001), [110] azimuth. 30.38° incident angle. Specular intensity = 183 units. Data normalized to 1000 units direct beam intensity. Data points every .45 degrees, each connected with line. Beam and surface at 300 K. Expected peak position denoted by arrow.

AP-1048

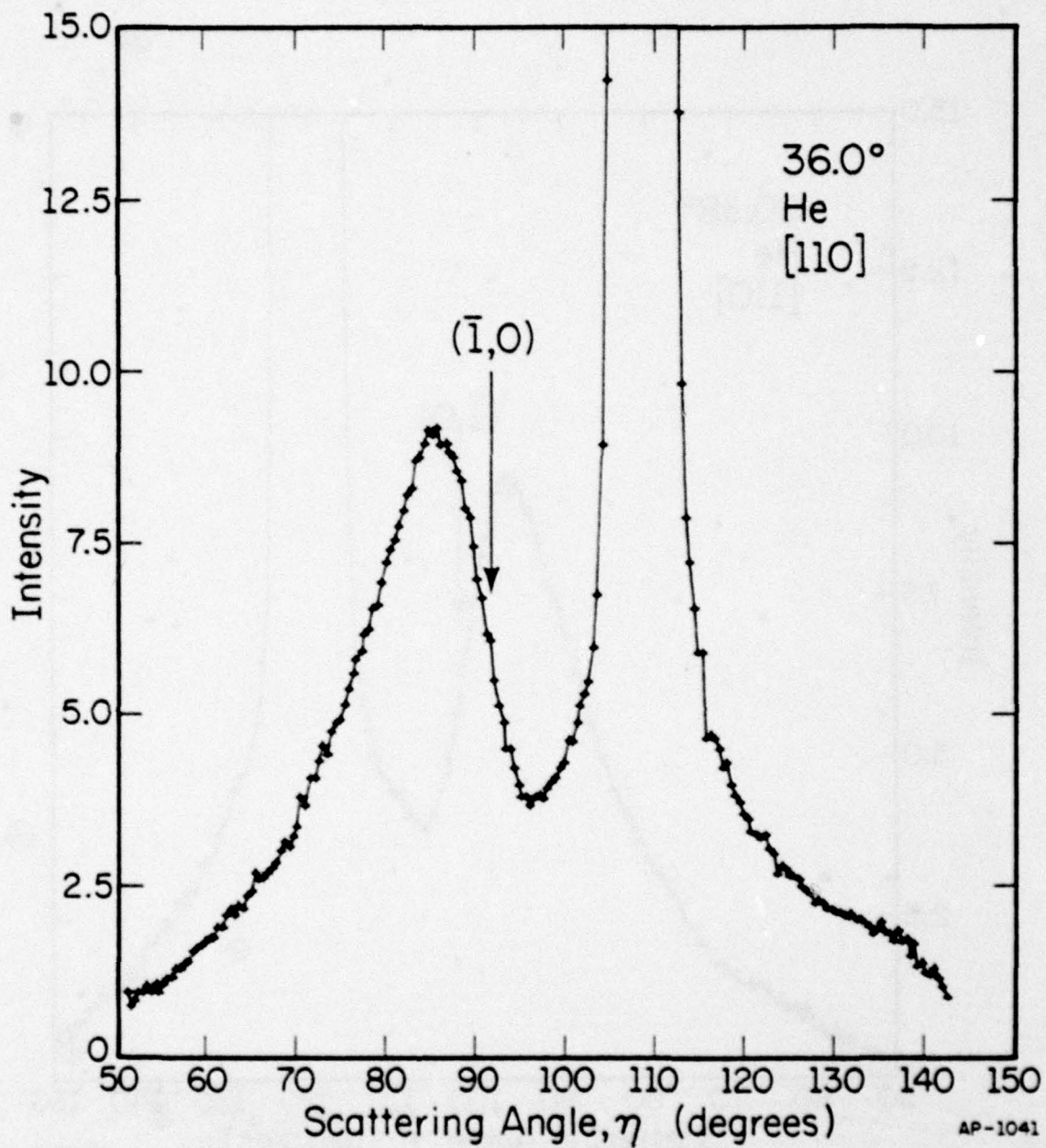


Fig. 13. Helium scattering from MgO (001), [110] azimuth,  $\theta_0 = 36.0$  degrees. Specular intensity = 144 units.

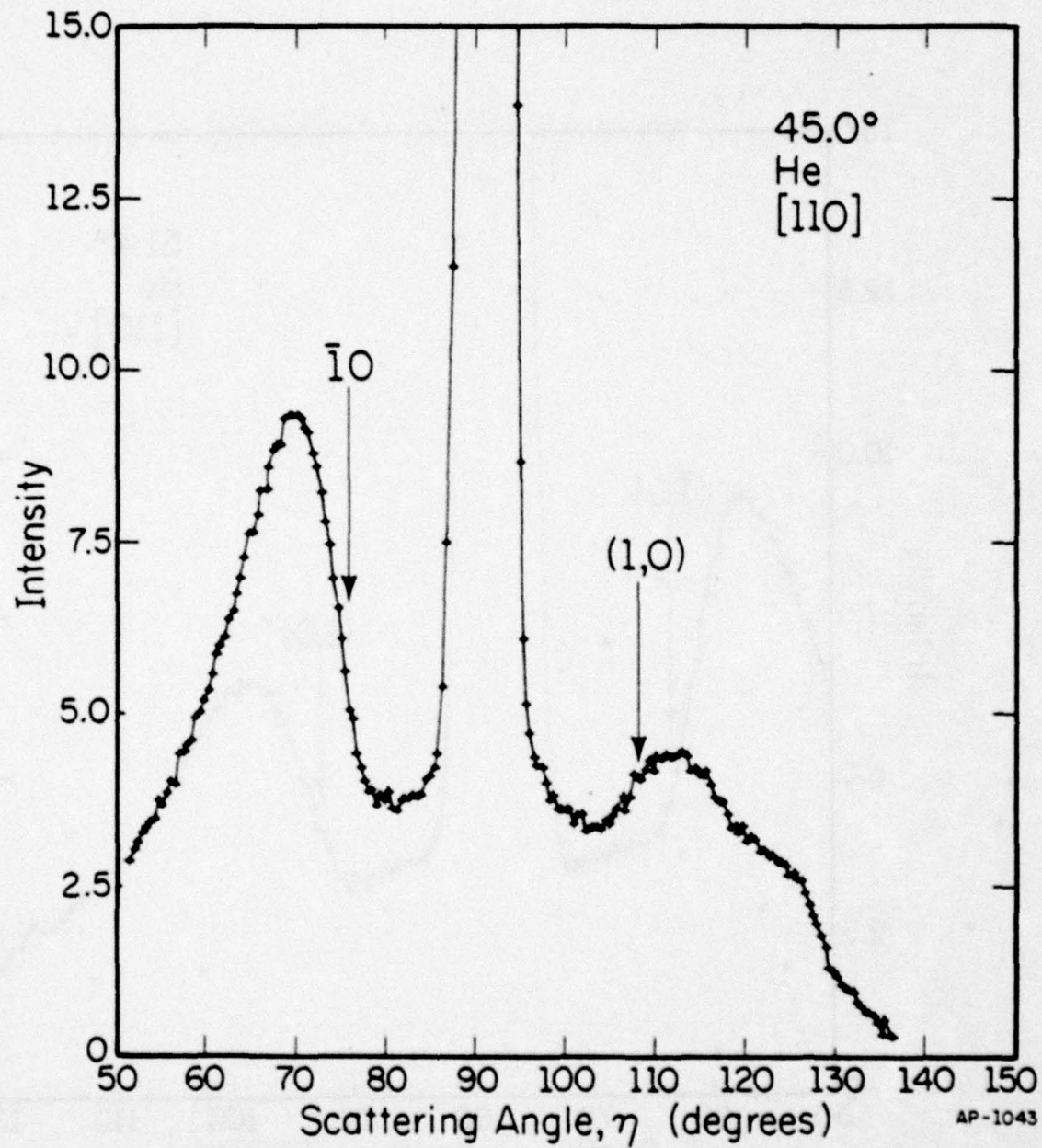


Fig. 14. Helium scattering from MgO (001), [110] azimuth. 45.0° incident angle. Beam and surface at 300 K. Specular intensity = 84.9 units. Direct beam = 1000 units.

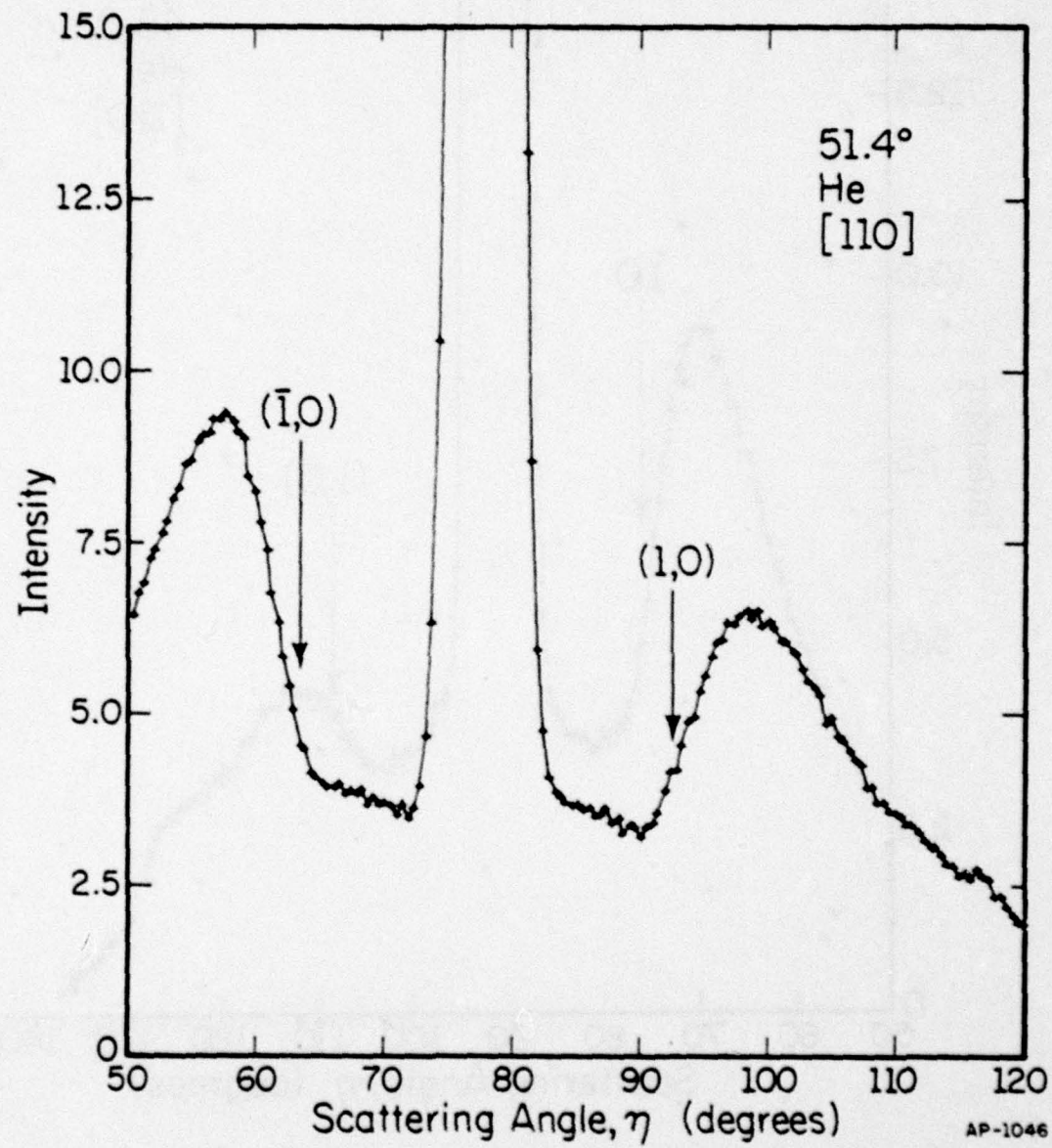


Fig. 15. Helium scattering [110] azimuth. 51.4 degrees incident angle.  
Specular = 60.4 units.

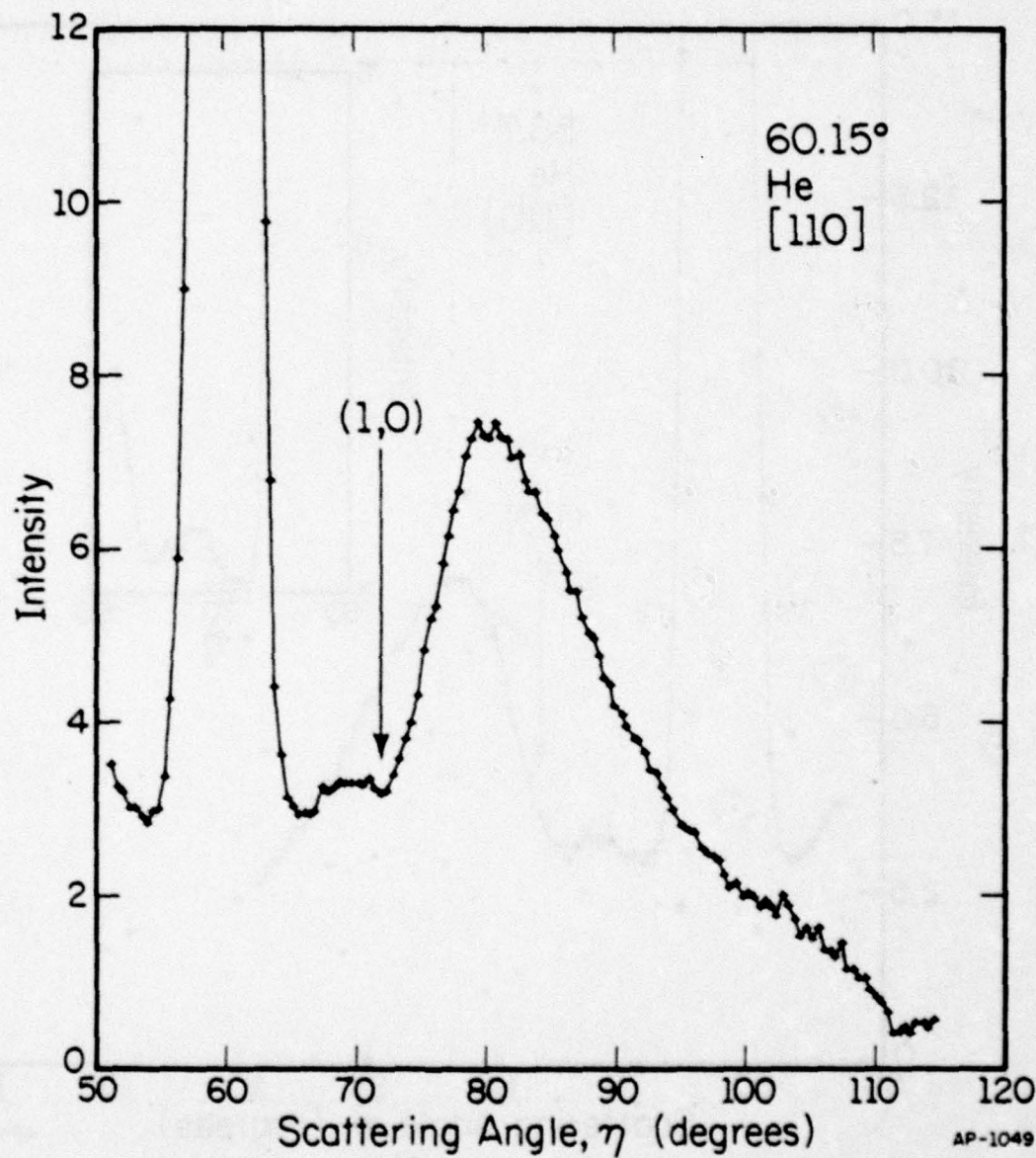


Fig. 16. Helium, MgO (001), [110] azimuth. 60.15 degrees incident angle. Specular intensity = 37.7 units.

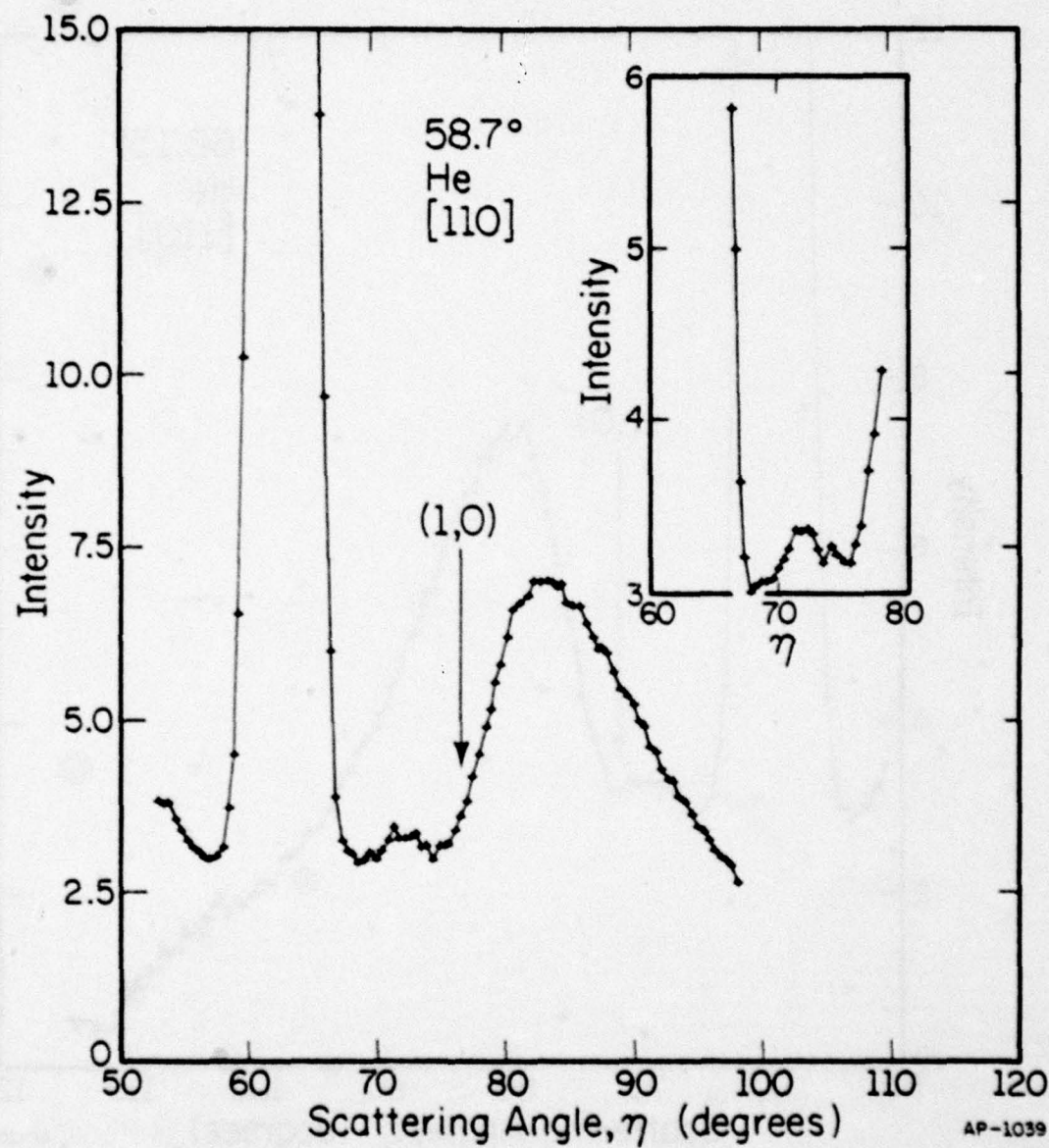


Fig. 17. Helium scattering from MgO, (001), [110] azimuth. Incident angle = 58.7 degrees. Specular intensity = 44.3 units. Complete regular scan taken at 10 sec. per point, 10 sec. time constant; inset, low noise blow up of selected portion showing the small peak near  $\eta$  = 70°. Taken at 60 sec. per point, 60 sec. time constant on integrator.

peaks will occur at angles  $\eta$  greater than the specular angle; negative order diffraction peaks will occur at  $\eta$  less than the specular angle. At first glance these lobes appear to be simply the first order diffraction peaks. This is, however, incorrect. The expected positions of the low order diffraction peaks are also indicated in the figures. As discussed in Chapter 2, it is not sufficient to calculate the angle to which the most probable wavelength is scattered. The positions shown in the figures were obtained from peak shapes calculated for a beam with a velocity distribution conforming to Eq. (7), assuming that the transition probability is independent of wavelength. Despite that, a considerable discrepancy between the positions calculated in this manner and the peak positions actually observed is apparent. The experimental peaks in all cases occur farther from the specular direction than expected. In fact, for several of the curves, the predicted peak lies near the bottom of the valley between the specular and the diffraction peak. In addition, at high  $\theta_0$ , that is, toward normal incidence, there is evidence for a small additional peak at the bottom of the valley. Although this peak is only slightly above the noise level, it is quite reproducible. It can be seen for all incident angles greater than  $50^\circ$ ; below that, it disappears into the baseline. The additional peak can be seen near  $\eta = 70^\circ$  in Figs. 16 and 17.

To examine this anomalous peak more closely, several scans of the selected area were taken using the integrator at its maximum setting to optimize signal to noise. The typical runs shown in this chapter were taken using  $\approx 1$  mv sensitivity on the lock-in, and integrating for 10 seconds at each angle, with a 10 second time constant on the integrator. For these short, low noise scans, the lock-in was operated at 50 or 100  $\mu$ V sensitivity,

while integrating for 60 seconds at each point, with a 60 second time constant on the integrator. With this improvement in signal to noise, the detailed structure in the scattered distribution can be seen clearly. An example is shown in the inset in Fig. 17. The additional peak is clearly not due to background noise.

#### 4.1.2 [100] Azimuth

R. Grant Rowe has previously presented data for the scattering of He from MgO (001) along the [100] incident azimuth.<sup>10</sup> Neither a displacement of the diffraction peaks from the expected positions, nor any additional peaks were observed. In an attempt to clarify the situation, measurements along the [100] were repeated on the same surfaces on which the [110] data above were obtained. For the most part, the [100] and [110] data were taken in pairs for a given incident angle, a measurement on one azimuth immediately following the other on the same surface.

Along the [100], the in-plane diffraction peaks have indices (n,n); the lattice periodicity along this direction is 4.20 Å. In Figs. 18-21 the data for the [100] azimuth can be seen for comparison with the data along the [110] presented earlier in this chapter. The expected positions of the first order diffraction peaks is also shown. For the [100] the agreement between the expected and observed positions is much better than for the [110]. The [100] data presented here also agree well with previous data on this surface. The anomalies observed with He diffraction along the [110] azimuth are clearly not artifacts of the experiment. Rather they must be indicative of the interactions between He and MgO.

There are two aspects of the [110] data which require examination;

- a) the systematic displacement of the peaks from the expected positions,

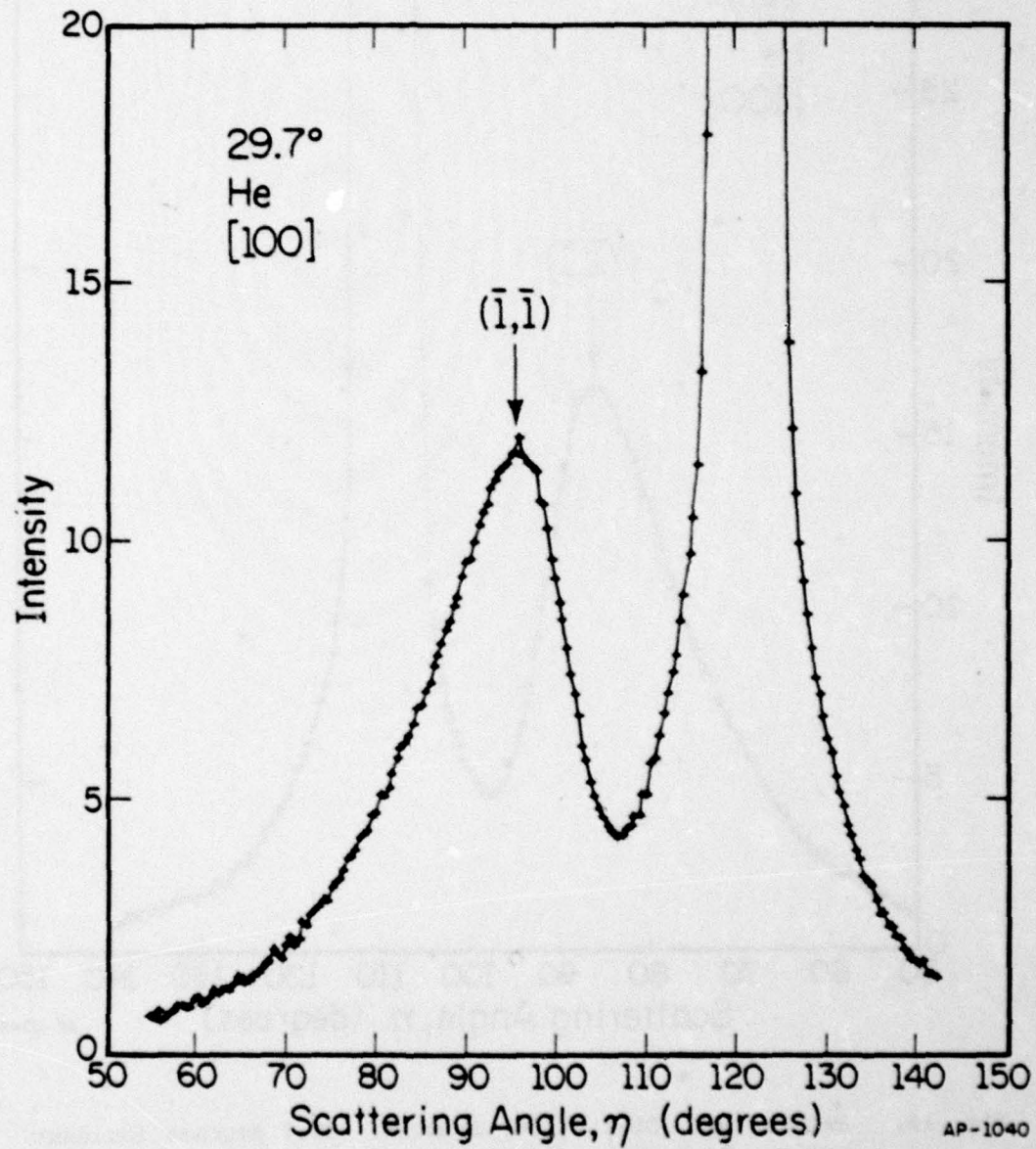


Fig. 18. Helium scattering, from MgO (001), [100] incident azimuth. 29.8 degrees incident angle. Specular intensity = 29.4 units. To be compared to Fig. 12 for the [110] azimuth. Expected peak position denoted by arrow.

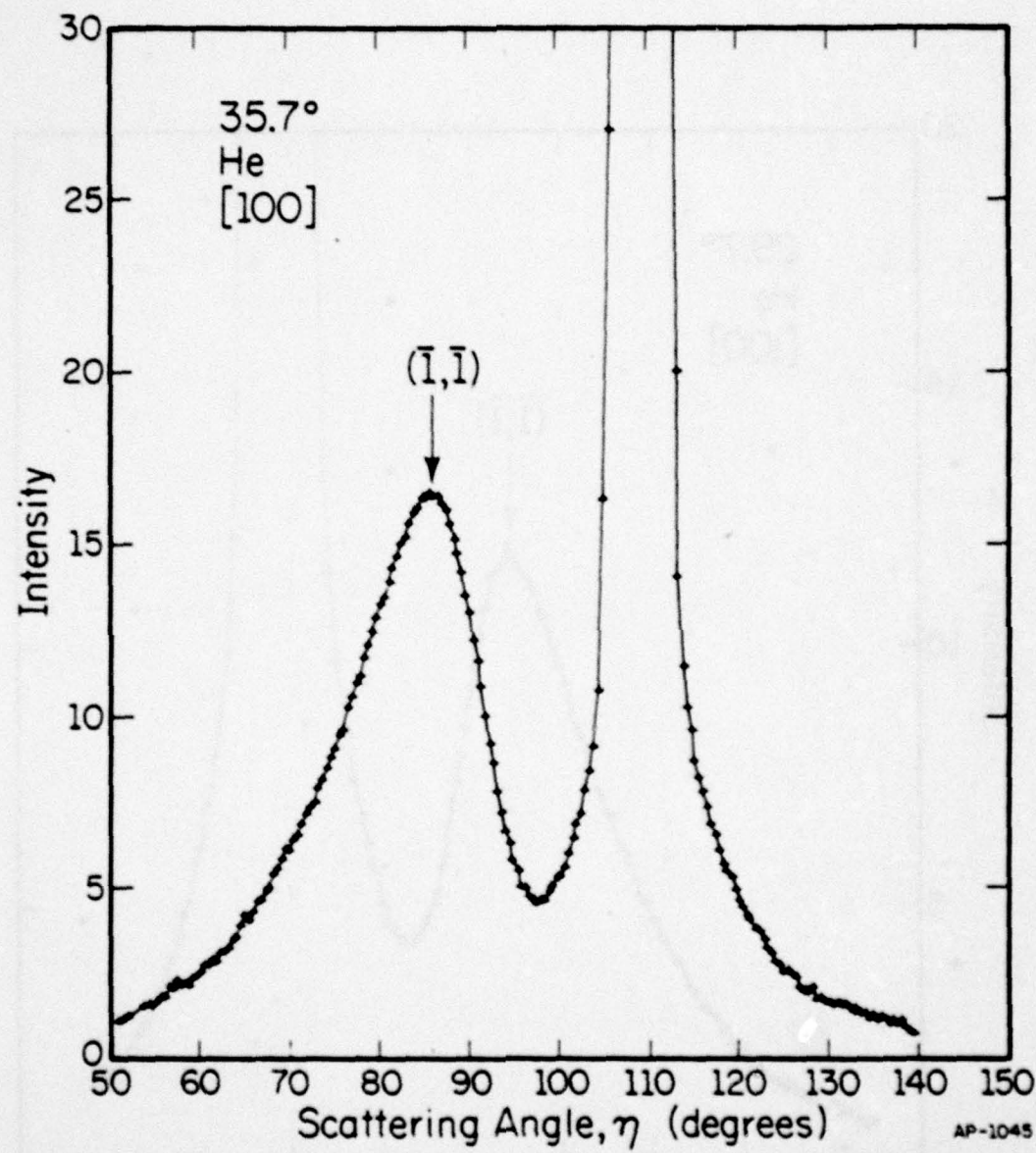


Fig. 19. Helium, MgO (001), [100] azimuth. 35.7 degrees incident angle. To be compared to Fig. 13, for the [110] azimuth.

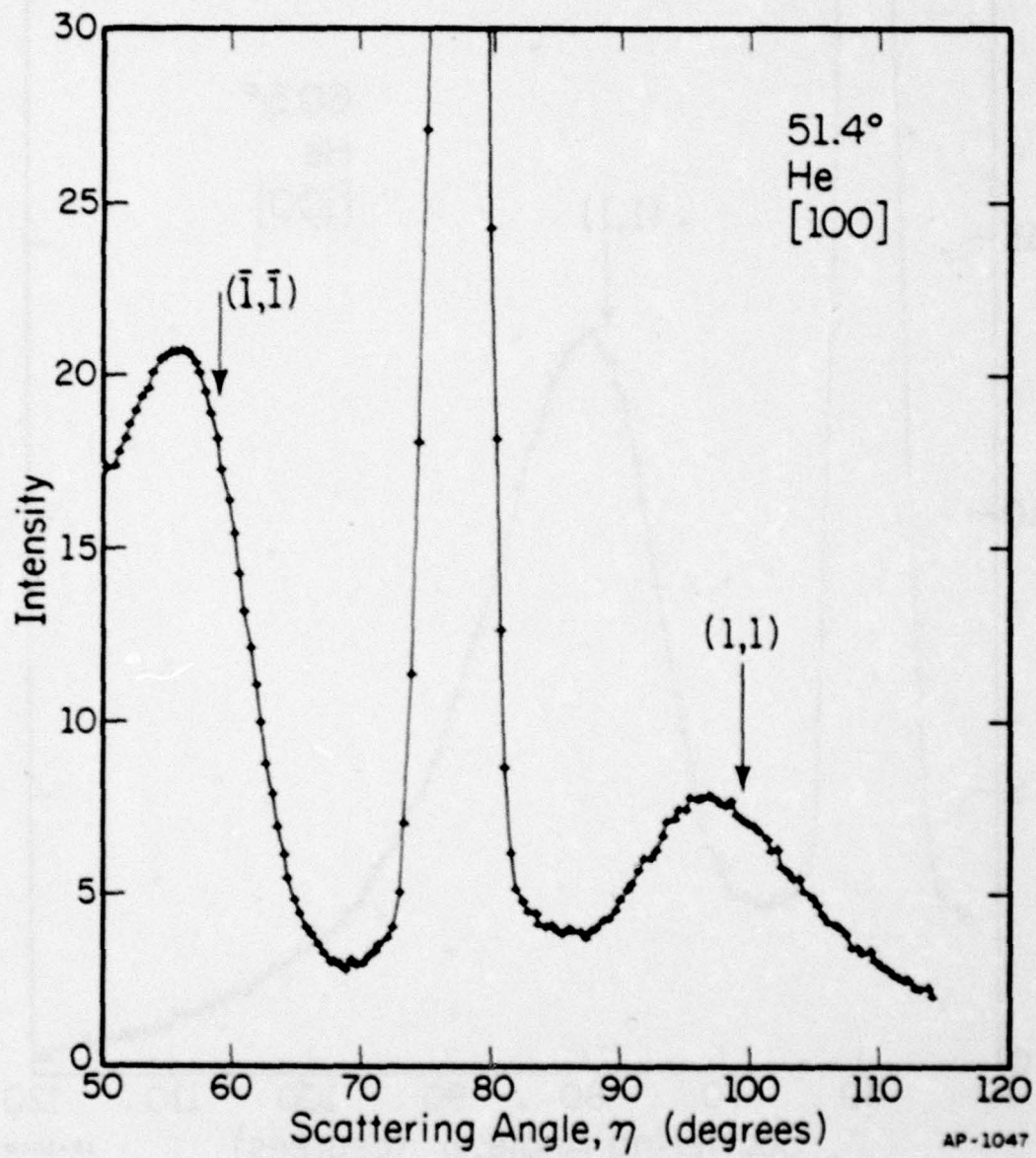


Fig. 20. Helium, MgO (001), [100] incident azimuth.  $\theta = 51.4^\circ$ .  
65.5 units specular intensity. To be compared to Fig. 15  
for [110] azimuth.

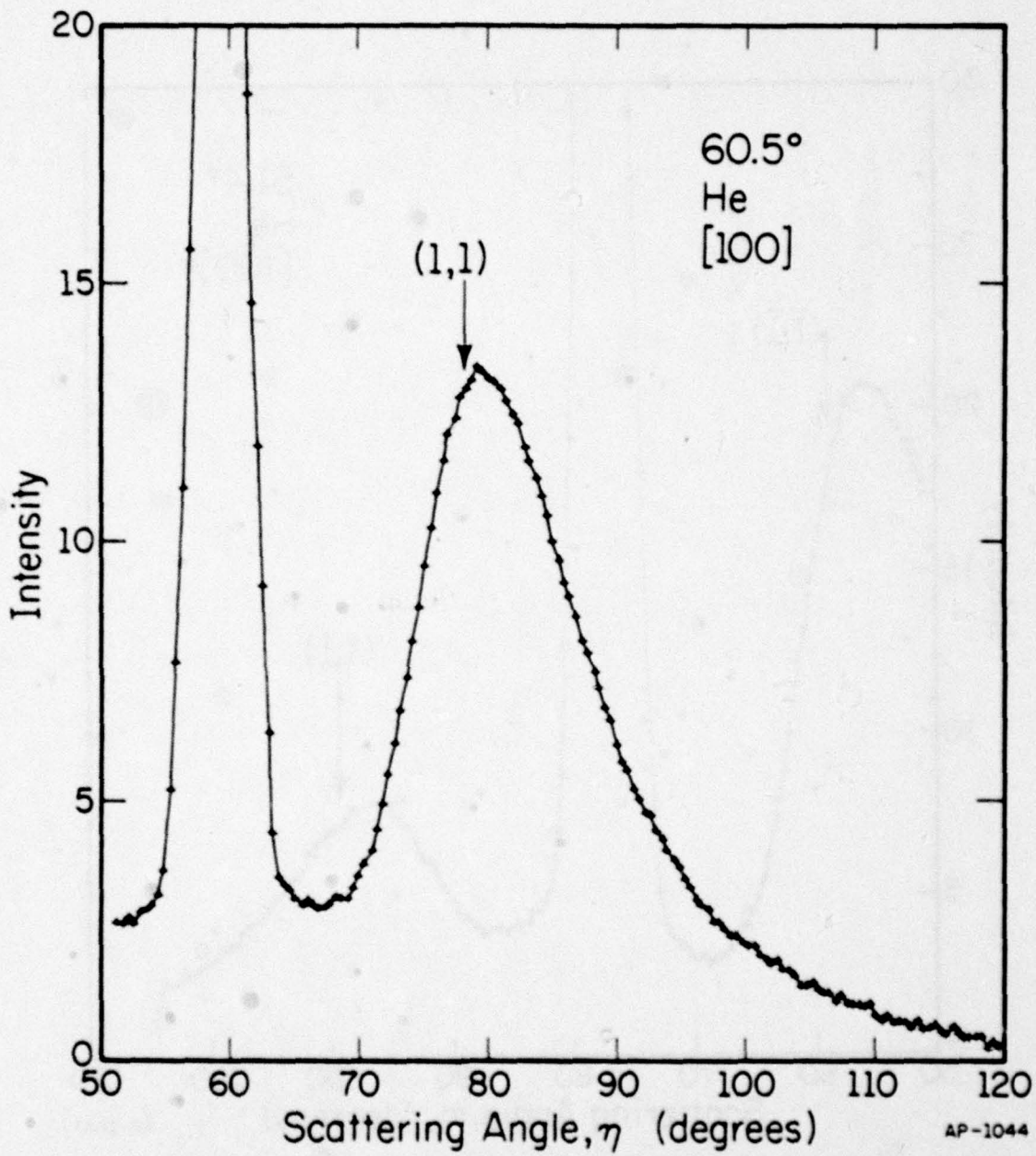


Fig. 21 Helium scattering from MgO (001), [100] azimuth.  $\theta = 60.5$  degrees. 38.8 units specular intensity. To be compared with Fig. 16 for [110] azimuth.

AP-1044

and b) the presence of small additional peaks. Neither effect is apparent on the [100] azimuth. The small peaks do not appear at the  $\frac{1}{2}$  order diffraction positions. This might be expected if the surface were to reconstruct to a periodicity twice the bulk lattice. The displacement could result from a straightforward superposition of higher order diffraction peaks. However, since the expected first order peak often occurs near the bottom of the valley, a very large intensity in the higher orders relative to the first order would be required. This appears unlikely.

A possible explanation for the peak displacement is a diffraction probability which is strongly a function of wavelength. Since the high energy, short wavelength particles are diffracted closest to the specular, it is necessary to severely attenuate these in order to move the peak outward. If these particles were preferentially diffracted into the higher order peaks, the diffraction profile would shift outward. Furthermore, if the transition probability were not monotonic, but oscillatory in wavelength, this might produce the small anomalous peak. It remains to make these arguments quantitative. To this end we have carried out calculations of the diffraction intensity.

#### 4.2 Semiclassical Calculations of Scattering

We wish to calculate diffraction probabilities as a function of wavelength, in such a manner as to facilitate comparison with the experimental data. The semiclassical approximation has proved useful in calculations of low energy elastic as well as inelastic collisions in the gas phase,<sup>18,19</sup> and has recently been extended to elastic collisions at surfaces.<sup>20-23</sup>

Basically, the approach is to use classical mechanics for the collision dynamics, but quantum mechanical superposition of the resulting scattering

amplitudes. One can show that in the classical limit, only those points on the surface which lie on a classical path between the initial and final states will contribute strongly to the scattering amplitude. Only these trajectories are included in the semiclassical calculation. A brief derivation of the semiclassical formalism follows.<sup>40</sup>

#### 4.2.1 Review of Semiclassical Theory

We begin by writing

$$\psi(r) = A(r)e^{iS(r)/\hbar} = e^{iS(r)/\hbar} + \sigma(r) . \quad (11)$$

We assume the Hamiltonian is independent of time. Substituting Eq. (11) into the time independent Schrödinger equation and separating into real and imaginary parts yields

$$(\nabla S)^2 = [p(r)]^2 + \frac{\hbar^2 \nabla^2 A}{A} \quad (12)$$

and

$$\nabla^2 S = -\frac{2\nabla S}{A} \cdot \nabla S , \quad (13)$$

where

$$p(r) = \hbar k(r) = \sqrt{2M_g(E-V(r))} \quad (14)$$

is the local momentum. Recalling that the flux of particles  $j_s$  is equal to

$$j_s = \frac{\hbar}{2im_g} \operatorname{Im} \psi^* \nabla \psi , \quad (15)$$

it is apparent that Eq. (13) is just the continuity equation

$$\nabla \cdot j_s = \nabla \cdot (A^2 \nabla S) = 0 . \quad (16)$$

We obtain the classical limit by dropping the last term in Eq. (12). This will be valid whenever

$$\frac{\hbar^2 \nabla^2 A}{A} \ll [p(r)]^2 . \quad (17)$$

Using Eq. (16), this implies in one dimension that  $|\frac{d\lambda}{dx}| \ll 1$ , that is, the wavelength does not change appreciably over a distance comparable to the wavelength. In other words, over small distances the motion is plane wave like. Under these conditions, Eq. (12) becomes

$$\frac{1}{2Mg} (\nabla S(r))^2 = E - V(r). \quad (18)$$

This is just the Hamilton-Jacobi equation of classical mechanics, where  $S(r)$  is Hamilton's characteristic function.<sup>41</sup> Equation (18) can be integrated to give

$$S(r) = \vec{p}_i \cdot \vec{r}_i + \int_{r_i}^r \vec{p} \cdot d\vec{s}, \quad (19)$$

the integral being along the classical path through the potential. We see that, in the classical limit, the "phase" of our wavefunction is just the action along the classical path in units of  $\hbar$ . In a straightforward manner we can derive a relation for the amplitude of the wavefunction using the continuity equation Eq. (16), to yield

$$A(r) = e^{\sigma(r)} = \frac{1}{\sqrt{\frac{v}{z}}} \left[ \frac{\partial(x,y)}{\partial(x_0,y_0)} \right]^{-\frac{1}{2}}. \quad (20)$$

The term in brackets is the Jacobian of the transformation from the final coordinates  $(x,y)$  to the initial coordinates  $(x_0,y_0)$ .

Our semiclassical wavefunction thus becomes

$$\psi(r) = \frac{1}{\sqrt{\frac{v}{z}}} \left[ \frac{\partial(x,y)}{\partial(x_0,y_0)} \right]^{-\frac{1}{2}} \exp(ik_0 \cdot r_0 + i \int_{r_0}^r k(r) \cdot ds). \quad (21)$$

60

It remains to use quantum superposition in the proper manner to find the scattering amplitudes. In general there will exist several classical paths through the potential connecting the initial and final states. All of the quantum effects in the semiclassical approximation come from the superposition of these trajectories.

We will write the wavefunction in a Fourier series with coefficients

$$F_{n,m}(z) = \frac{1}{a_x a_y} \iint_{\substack{\text{x,y unit cell}}} \psi(x,y,z) \exp(-i(\vec{k}_o + \vec{G}_{n,m}) \cdot \vec{R}) dx dy , \quad (22)$$

where we have made use of the periodic nature of the surface potential. The diffraction intensities will be given by  $v_z |F_{n,m}|^2$ . Substituting our semiclassical wavefunction, we obtain

$$F_{n,m}(z) = \frac{1}{a_x a_y} \iint_{\substack{\text{x,y unit cell} \\ z}} \frac{1}{v_z} \left[ \frac{\partial(x,y)}{\partial(x_o, y_o)} \right]^{-\frac{1}{2}} \exp[i(\frac{S}{\hbar} - (\vec{k}_o + \vec{G}_{n,m}) \cdot \vec{R})] dx dy . \quad (23)$$

We are interested in Eq. (23) only in the limit  $z \rightarrow \infty$ , that is, far from the surface. The integral in Eq. (23) is over  $(x,y)$ , that is, over different starting points for the trajectories. It is thus an integral over all the possible trajectories. If  $S/\hbar$  is large, the phase of the integrand varies rapidly as a function of  $(x,y)$ . Integrals of this type are usually evaluated in the stationary phase approximation.<sup>42</sup> In one dimension, the method of stationary phase applies to integrals of the form

$$I = \int g(x) e^{if(x)} dx ,$$

where  $f(x)$  is a rapidly varying function of  $x$ . The stationary phase approximation is

$$I \approx \sum_i g(x_i) \left( \frac{2\pi i}{f''(x_i)} \right)^{\frac{1}{2}} e^{if(x_i)} , \quad (24)$$

where the  $x_i$  are solutions to  $f'(x_i) = 0$ , that is, they are the points of stationary phase. The stationary phase condition applied to Eq. (23), however, is precisely the diffraction condition, Eq. (3),

$$\vec{k} = \vec{k}_0 + \vec{g}_{n,m} \quad (3)$$

The diffraction condition is thus obtained in a very natural way within the semiclassical approximation.

We have concluded that only those points on the surface which lie along the classical trajectories will contribute to scattering, and, furthermore, that only those trajectories for which Eq. (3) is satisfied will contribute. The primitive semiclassical approximation to the scattering intensities results from a straight quantum superposition of the several (two) contributing amplitudes. We thus have the primitive semiclassical approximation for the scattering amplitude

$$F_{n,m} = \frac{1}{a^2} \sum \left[ \frac{(2\pi/i)^2}{\delta(p_x, p_y)} \right]^{\frac{1}{2}} , \quad (25a)$$

where

$$\phi = - \int x \dot{p}_x dt + y \dot{p}_y dt + z \dot{p}_z dt \quad (25b)$$

and the sum is over all the classically allowed trajectories in the unit cell satisfying Eq. (3), the diffraction condition.

The stationary phase formula, Eq. (24), was derived by expanding the phase,  $f$ , in a quadratic expression. It becomes invalid if  $f''$  is small. This will occur whenever two points of stationary phase,  $x_1$ , and  $x_2$ , coalesce. The trajectories for which this occurs are of considerable interest in scattering calculations. To avoid the singularity which occurs in using

Eq. (24) when  $f''$  is small, the uniform semiclassical approximation was developed.<sup>19b</sup> By expanding  $f(x)$  near the points of stationary phase as a cubic, a new stationary phase formula, involving Airy functions, can be derived which is well behaved in this critical region. The scattering intensities in the uniform semiclassical approximation become<sup>22,19b</sup>

$$P_{n,m} = (|\Omega_1|^{\frac{1}{2}} + |\Omega_2|^{\frac{1}{2}})^2 \pi q^{\frac{1}{2}} A_i^2(-q) + (|\Omega_1|^{\frac{1}{2}} - |\Omega_2|^{\frac{1}{2}}) \pi q^{\frac{1}{2}} B_i^2(-q) \quad (26)$$

$$\text{where } q = (3/4|\varphi_1 - \varphi_2|)^{2/3} \quad (27)$$

and

$$\Omega_i = \frac{\hbar}{a^2} \frac{\partial(p_x, p_y)}{\partial(x_0, y_0)} \quad (28)$$

The phases  $\varphi_i$  for the two trajectories are given by Eq. (25b). We will use the semiclassical approximation in this form.

There is an alternative derivation of the semiclassical approximation which proceeds not from the Schrödinger equation, but from the Feynman path integral<sup>43</sup> formulation of quantum mechanics. It is mentioned here briefly for the insight it provides to the nature of the approximation.

In the path integral formulation, the quantum propagator  $K(q_1, q_2)$  is given by

$$K(q_1, q_2) = \langle q_2 | e^{i \frac{H(t_2 - t_1)}{\hbar}} | q_1 \rangle \approx \int_{q_1}^{q_2} e^{i \frac{S(q_2, q_1)}{\hbar}} dq, \quad (29)$$

where the integral on the right side is over all the possible paths connecting the initial and final states, and  $S$  is again the classical action associated with a given path. This is exact quantum mechanics. It says all paths

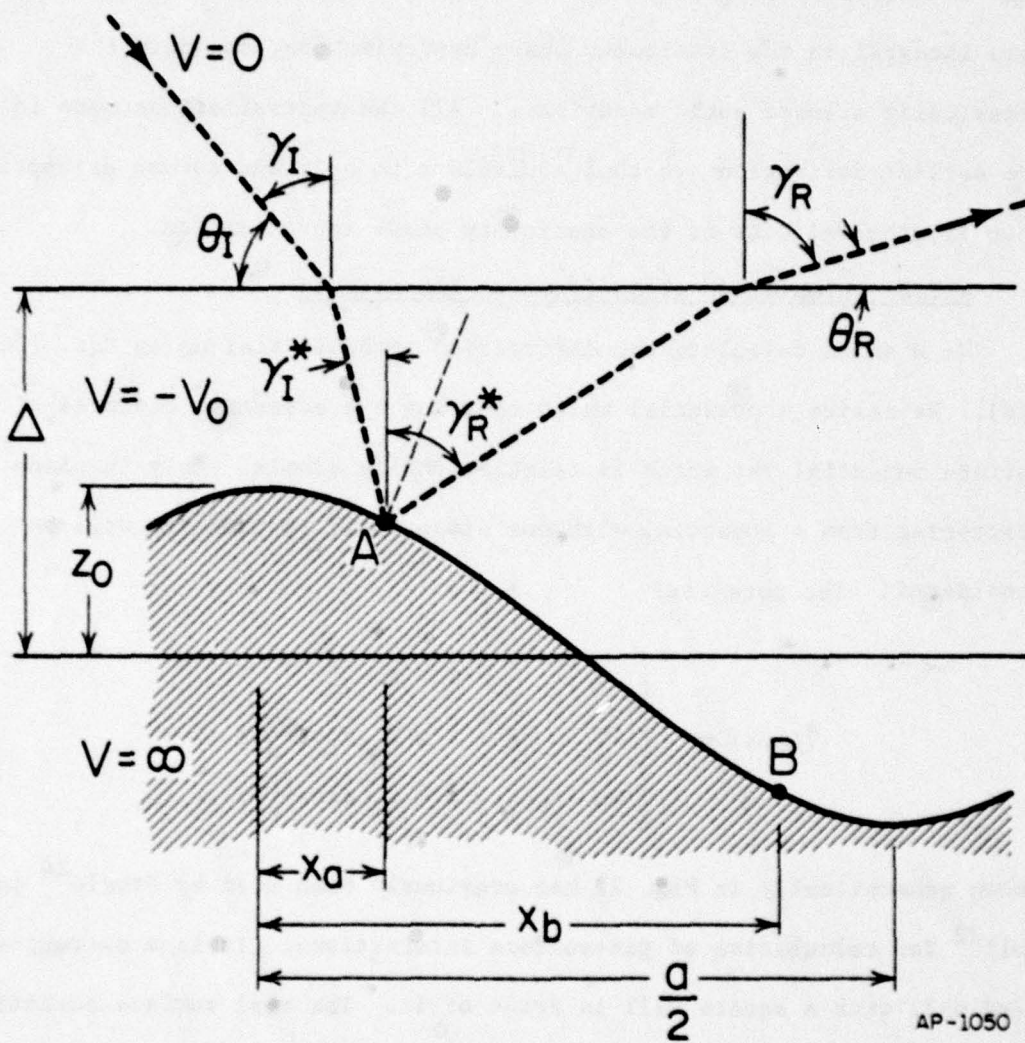
contribute to the scattering amplitude, each with its own phase. All that is necessary to get to the semiclassical approximation is to evaluate this integral in the stationary phase approximation; now only the classically allowed paths contribute. All the approximations made in the earlier derivation are thus equivalent to only one common assumption, that is, the validity of the stationary phase approximation.

#### 4.2.2 Calculation of Diffraction Intensities

We wish to calculate the diffraction probabilities using Eqs. (26)-(28). We desire a potential which contains the essential features of the surface potential yet which is calculationally simple. Only in plane scattering from a potential with one dimensional periodicity will be considered. The potential

$$V(x,z) = \begin{cases} 0 & z > \Delta \\ -V_0 & \Delta > z > Z_0 \cos\left(\frac{2\pi x}{a}\right) \\ +\infty & z < Z_0 \cos\left(\frac{2\pi x}{a}\right) \end{cases} \quad (30)$$

shown schematically in Fig. 22 has previously been used by Steele<sup>24</sup> and Doll<sup>22</sup> for calculation of gas-surface interactions. It is a corrugated hard wall with a square well in front of it. The real surface potential has a gentle long range attractive part and a short range, fairly hard repulsion. The long range attraction, however, has been shown to have little effect on the scattering.<sup>44,45</sup> Only the hard, short range potential is important. Thus, although this model potential is crude, it contains the essential features of the interaction, and has been adopted for our calculations.



AP-1050

Fig. 22. Steele's potential, showing one of the classical paths. An equivalent path strikes the wall at  $x_b$ . The lattice spacing is "a".  $Z_0/a$  exaggerated for clarity.

Our semiclassical approximation should be most appropriate for short wavelengths and for gradually changing potentials. Masel,<sup>20d</sup> however, has compared the semiclassical solution to an exact quantum solution for normal incidence in a simple corrugated hard wall potential. This hard wall should be an extreme test of the semiclassical theory. Essentially exact agreement between the quantum and semiclassical results was obtained down to wavevectors  $ka = \frac{2\pi a}{\lambda} \approx 10$ , that is, up to wavelengths  $\lambda \approx 1.8 \text{ \AA}$ . Since this is more than three times the most probable wavelength in a thermal beam at  $300^\circ\text{K}$ , the semiclassical approximation should give excellent results, even for this simple potential.

The classical trajectories in this piecewise constant potential are straight lines. One such trajectory is shown in Fig. 22. There are two equivalent trajectories per unit cell, corresponding to the two points of equal slope. These are denoted by A and B in the figure. For this case, considerable simplification of Eq. (26) results. We obtain<sup>22,46</sup>

$$P_n(\theta, E) = 4\pi q^{\frac{1}{2}} |Ai(-q)|^2 \quad , \quad (31)$$

where

$$\Omega = \Omega_1 = -\Omega_2 = \frac{(1-\tan \gamma_I^* \tan \alpha)(1+\tan \alpha)}{8\pi^2 Z_o^2 \cos \gamma_R^* \cos(\frac{2\pi x_1}{a}) (\frac{2m(E+V)}{h})^{\frac{1}{2}}} \quad . \quad (32)$$

The angles are given by  $\gamma = 90 - \theta$  and  $\sin \gamma = \sqrt{1+V/E} \sin \gamma^*$ , the \* referring to the corresponding angle measured inside the well.  $x_1$  is the x coordinate at which the trajectory intercepts the hard wall and  $\alpha$  is the slope of the corrugation at that point.  $P_n(\theta, E)$  is the probability of a particle of energy E being diffracted into diffraction peak n at  $\theta$ .<sup>46</sup>

Using the semiclassical formalism just described we have undertaken the calculation of the diffraction peak profiles, closely following the procedure of Doll.<sup>22</sup> The semiclassical intensities  $P_{n,0}(\theta, E)$  for  $-5 < n < 5$  were thermally averaged over the energy distribution of a thermal beam

$$F(E)dE = (kT)^{-2} E \exp(-E/kT)dE . \quad (33)$$

The intensity at any angle (except the specular) is given by<sup>20c</sup>

$$I(\theta) = \left| \frac{2 \sin \theta}{\cos \theta - \cos \theta_0} \right|^2 \sum_n E_n F(E_n) P(\theta, E_n) , \quad (34)$$

where  $E_n = E(n, \theta_0, \theta)$  is the energy of the atoms diffracted from  $\theta_0$  to  $\theta$  in diffraction channel  $n$ , subject to Eq. (3) and conservation of energy. The  $P(\theta, E_n)$ 's are the uniform semiclassical intensities given by Eq. (31). The term in front of the summation arises from  $\frac{dE}{d\theta}$  for elastic scattering. Within this model the calculations are straightforward and can be done for a range of parameters. The variable parameters in the model are the depth of the square well,  $V_0$ , and the amplitude of the hard wall,  $Z_0$ . Calculated distributions for a range of parameters for scattering along the [110] are shown in Figs. 23-32, where  $V_0$  is given in degrees Kelvin and  $Z_0$  in units of the lattice parameter,  $a$ .

The effect of variation of  $V_0$  at constant  $Z_0$  is shown in Figs. 23-26. The major effect of  $V_0$  is to refract the trajectories as they exit the well. This shifts the sharp cutoff at high and low angles away from the specular. These cutoffs occur at the so-called rainbow angles, a carryover from classical scattering. Classically, there exists a maximum and minimum

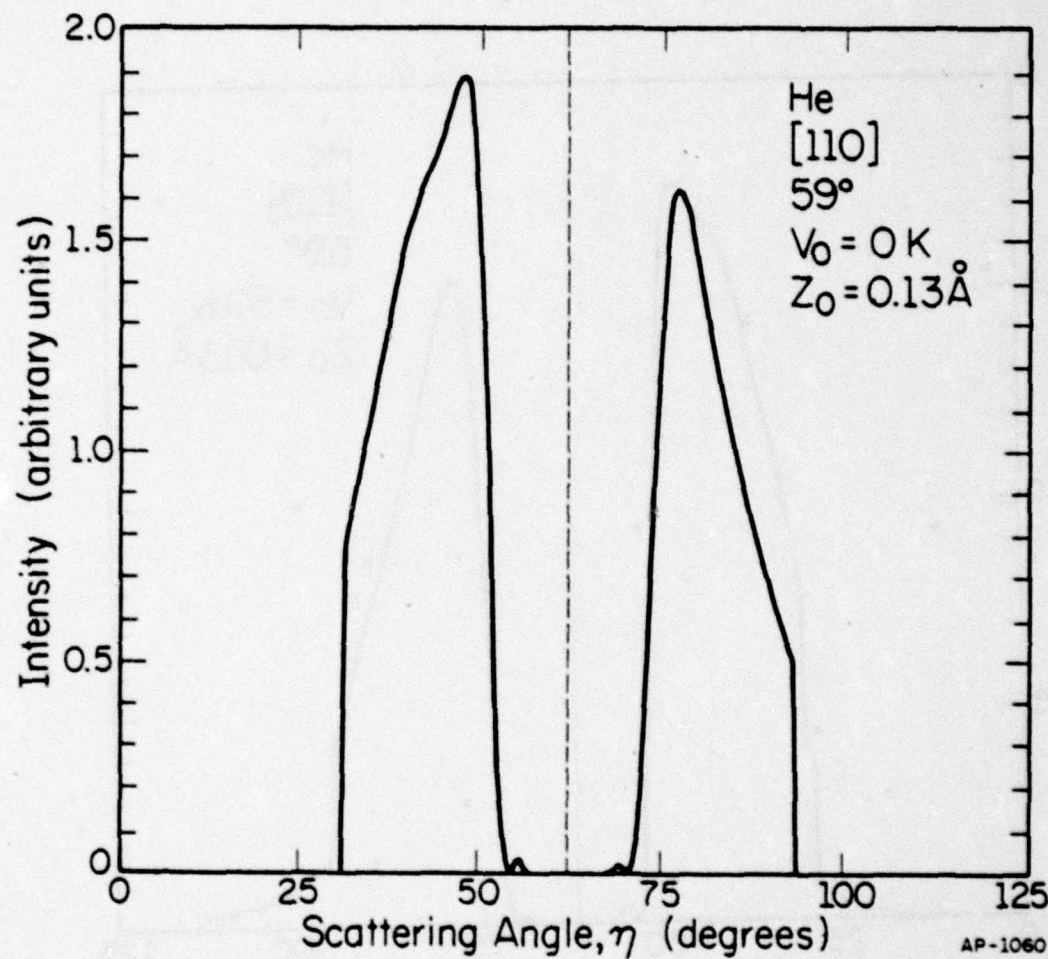


Fig. 23. Helium semiclassical scattering calculations. 300 K beam.  
 $V_0 = 0 \text{ K}$ ,  $Z_0 = 0.13 \text{ \AA}$ . Arbitrary units. [110] azimuth.

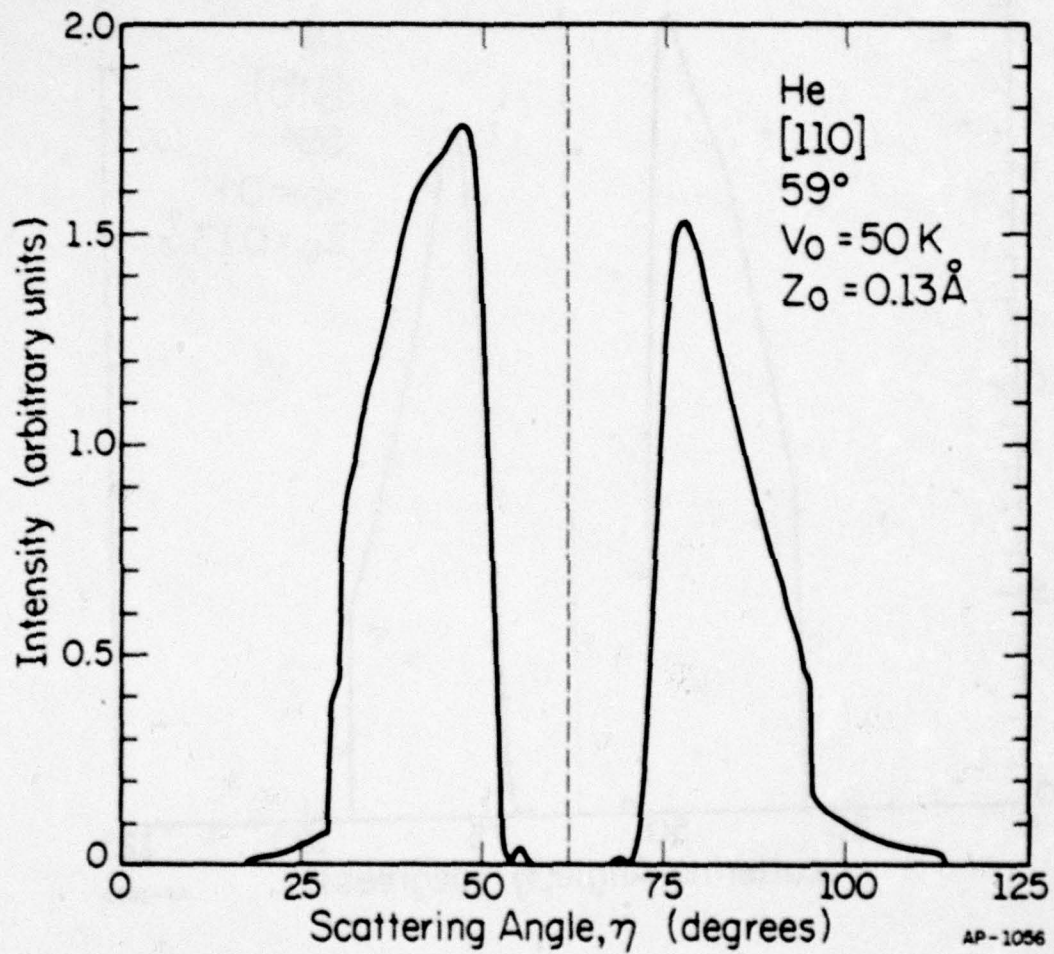


Fig. 24. Semiclassical scattering distribution for  $\theta_0 = 59^\circ$ , [110] azimuth. Helium from MgO (001).  $V_0 = 50$  K,  $Z_0 = 0.13 \text{ \AA}$ , Beam = 300 K.

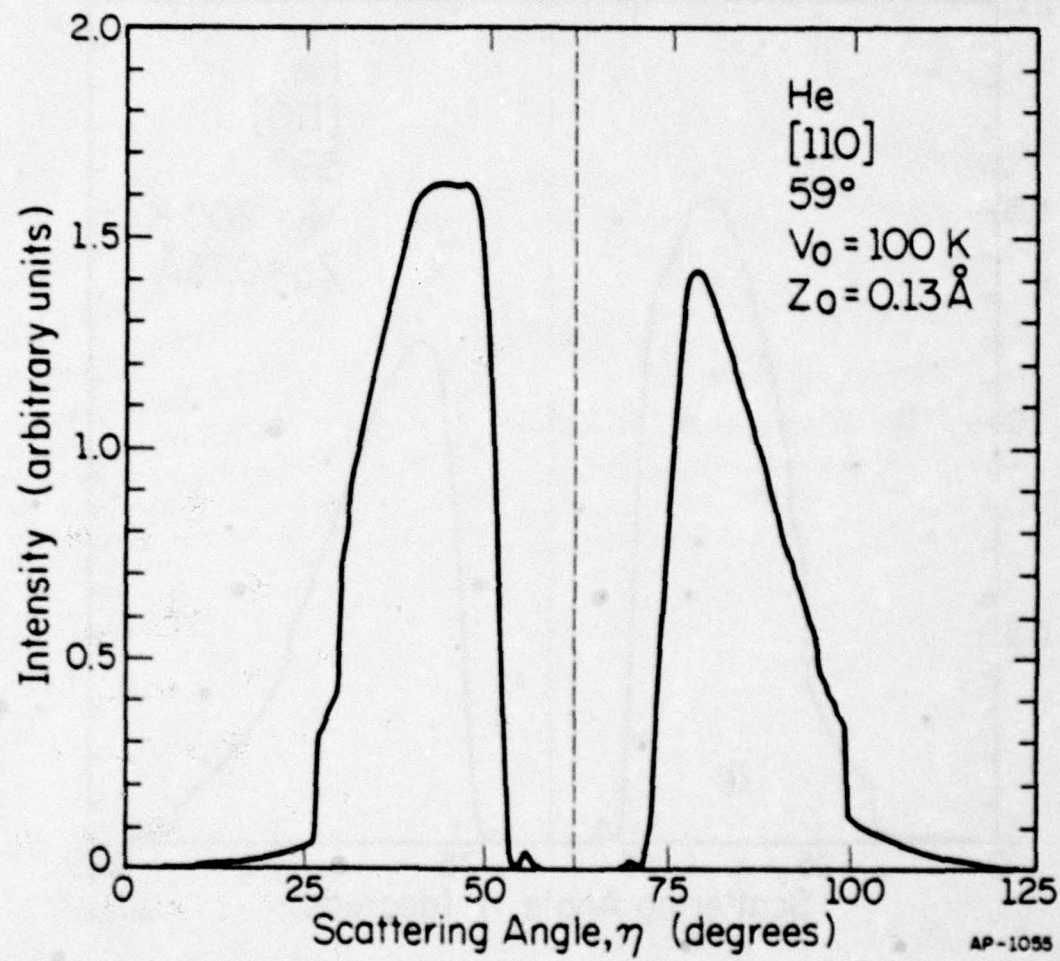


Fig. 25. Same as Fig. 23 except  $V_0 = 100 \text{ K}$ .

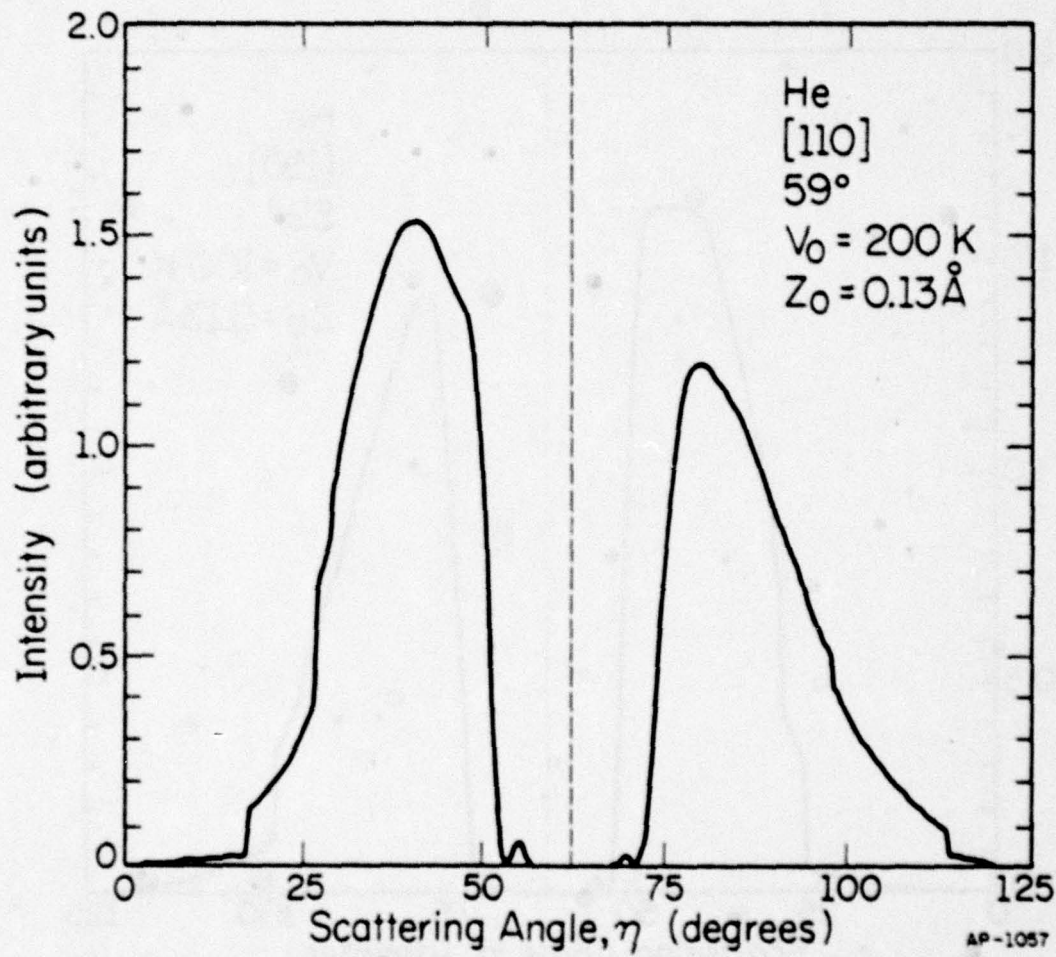


Fig. 26. Semiclassical calculation for helium scattering.  
 $Z_0 = 0.13 \text{ \AA}$ ,  $V_0 = 200 \text{ K}$ . [110] azimuth.

angle at which scattering from a periodic potential can occur; for our case this corresponds to trajectories which strike the inflection points on the hard wall, the points of maximum slope. Trajectories which require a deflection larger than this cannot occur. This classical factor enters our semiclassical formalism through the Jacobian,  $\Omega$ . The sharp cutoff is entirely the result of our hard wall potential. For a realistic potential, the inclusion of complex (tunneling) trajectories softens this sharp edge. For our hard wall potential, no such complex trajectories exist. Rainbow scattering, however, is not just a classical effect. The same cutoffs, albeit not as sharp, appear in a full quantum treatment of surface scattering.<sup>48</sup>

We are for the most part interested only in that portion of the scattering distribution closer to the specular. As  $V_0$  appears to have little effect on this part we will continue these calculations with  $V_0$  fixed at 100 K. This corresponds to a well depth of 8.62 meV, or about 16 per cent of the particle's incident kinetic energy. By comparison, the Morse potential well depth for helium on LiF, derived from experiment,<sup>49</sup> is 7.59 meV. The MgO well depth can be expected to be of the same order of magnitude.

Variation of  $Z_0$  has a significant effect upon the calculated profiles. Shown in Figs. 27-30, as well as Fig. 25, are the distributions calculated for various  $Z_0$  for  $\theta_0 = 59^\circ$  and  $V_0 = 100$  K, as well as the experimentally observed positions from Fig. 17. It is apparent that the broad lobes observed in the experiments are the sum of up to 5 diffraction peaks. Significant shifts in the peaks take place as a function

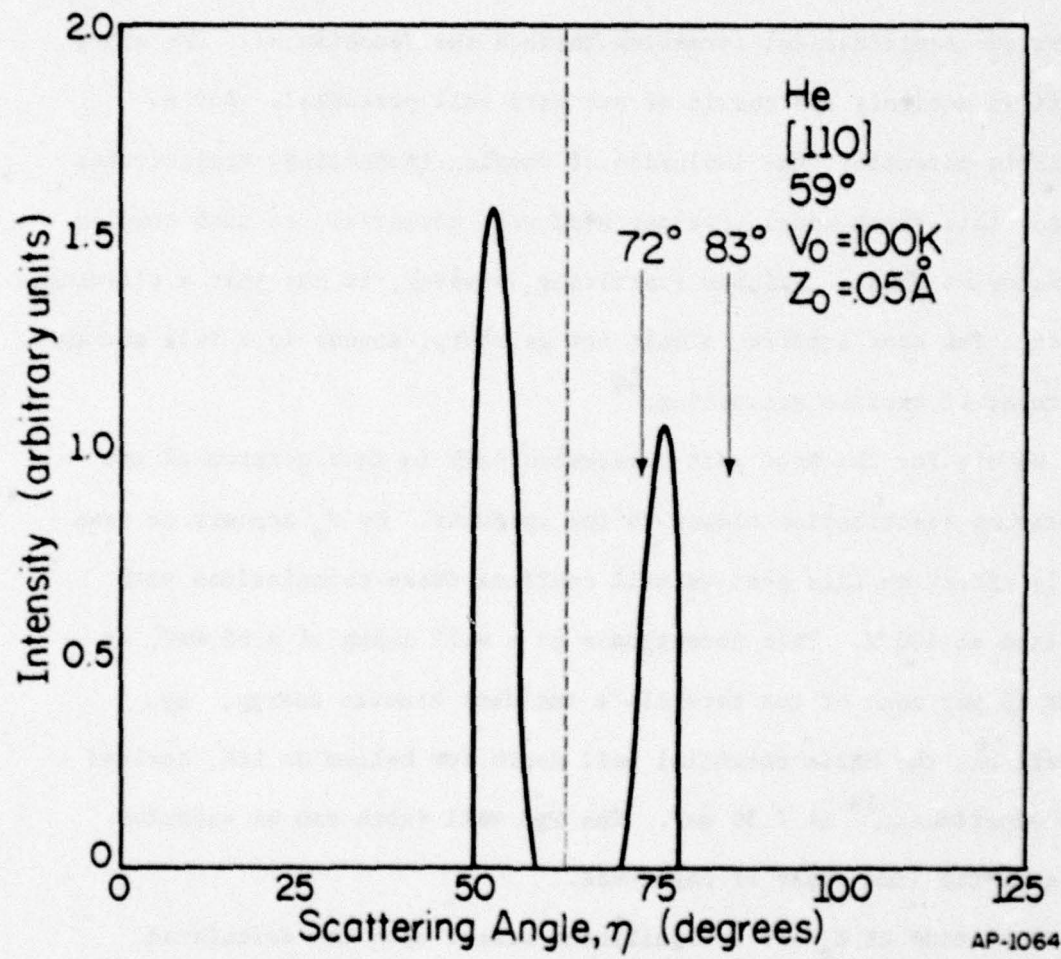


Fig. 27. Semiclassical scattering calculations for helium,  $Z_0 = .05 \text{\AA}$ ,  $V_0 = 100 \text{ K}$ ,  $\theta_0 = 59^\circ$ . For comparison with experimental data in Fig. 17. The specular position indicated by dashed line.

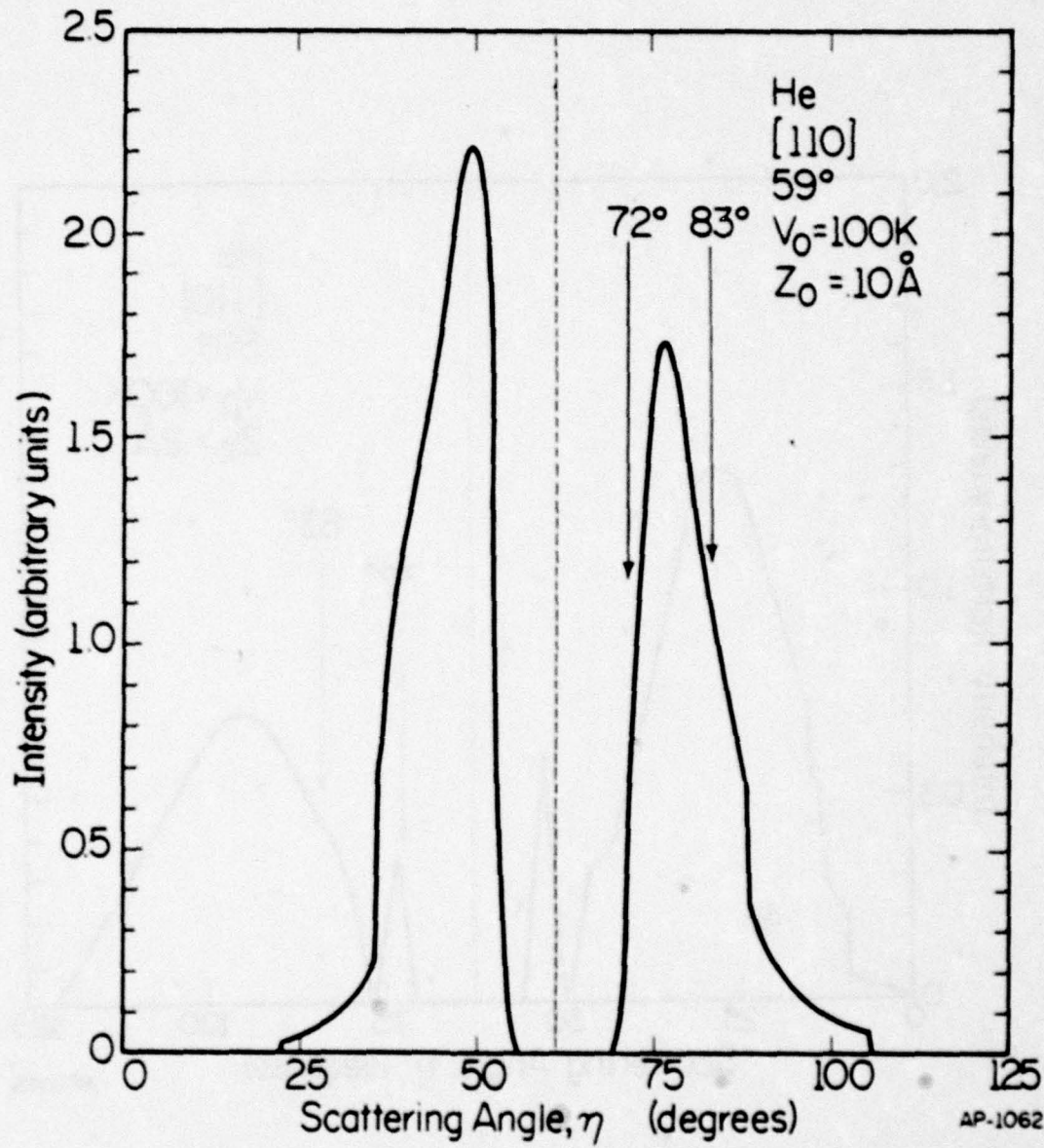


Fig. 28. Semiclassical scattering distributions for helium,  $Z_0 = .1\text{\AA}$ ,  $V_0 = 100\text{ K}$ ,  $\theta_0 = 59^\circ$ . Lattice spacing =  $2.97\text{\AA}$ . Average over thermal beam at  $300\text{ K}$ , diffraction channels  $|n| \leq 5$ . Experimental peak positions taken from Fig. 17.

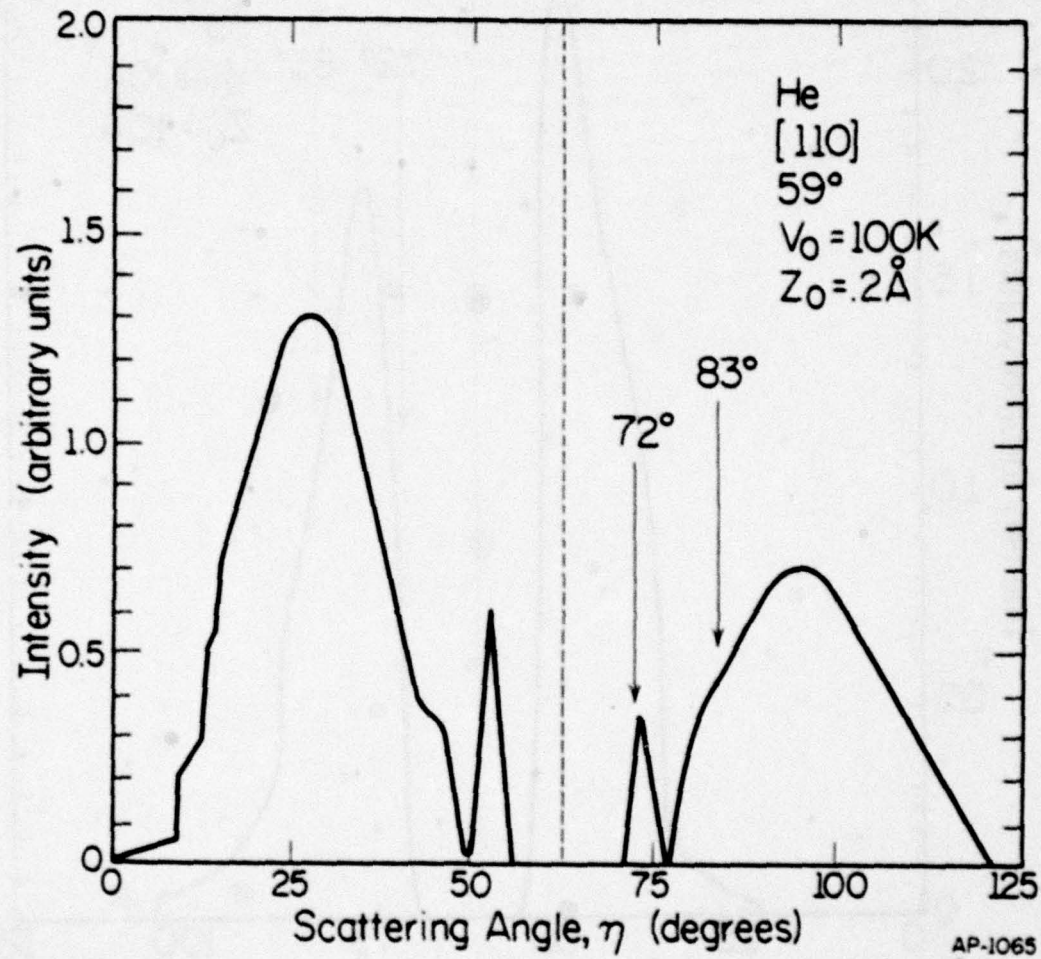


Fig. 29. Calculated semiclassical distributions for Helium, [110] azimuth MgO (001).  $\theta_0 = 59^\circ$ ,  $V_0 = 100\text{ K}$ ,  $Z_0 = .2\text{ \AA}$ . Thermal averaged profile for  $T_{\text{Beam}} = 300\text{ K}$ . Compare to data in Fig. 17. Experimental peaks indicated by arrows.

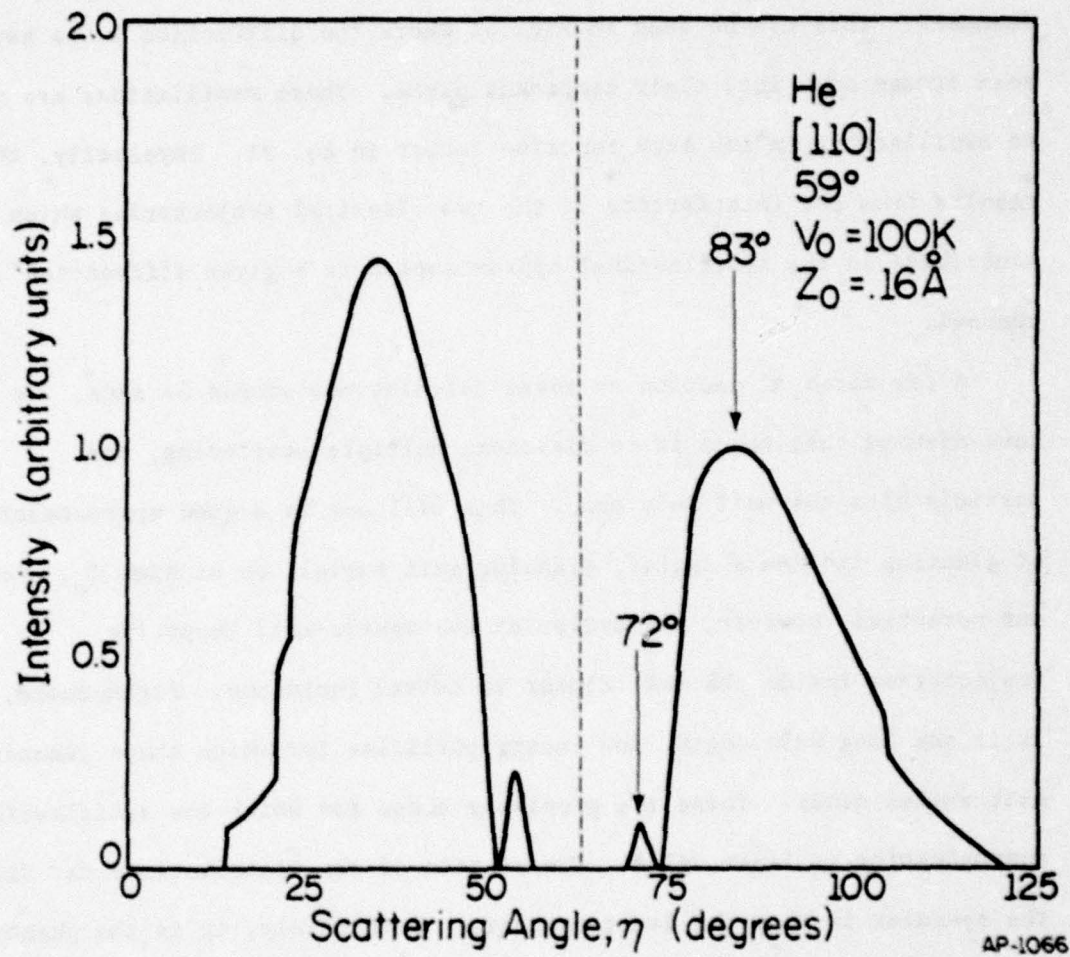


Fig. 30. Calculated semiclassical diffraction profile at  $59^\circ$  incident angle.  $Z_0 = 0.16 \text{ \AA}$ ,  $V_0 = 100 \text{ K}$ . Thermal beam at  $300 \text{ K}$ . Experimental peaks indicated by arrows. See Fig. 17. Only portion  $\eta > 50^\circ$  is experimentally accessible, arbitrary units. [110] azimuth.

of  $Z_o$ ; for large  $Z_o$ , the lobe splits into several peaks. Significant oscillations also appear in the intensity of the individual diffraction channels. This can be seen in Fig. 31 where the diffraction lobes have been broken down into their component peaks. These oscillations are due to oscillations in the Airy function factor in Eq. 31. Physically, this results from the interference of the two classical trajectories which contribute in the semiclassical approximation to a given diffraction channel.

A few notes of caution on these calculations should be made. We have assumed that there is no classical multiple scattering; the particle hits the wall only once. This will not be a good approximation at glancing incidence angles, glancing exit angles, or at high  $Z_o$ . For our potential, however, refraction at the square-well keeps the trajectories inside the well closer to normal incidence. Furthermore, it is the long wavelength, low energy particles for which these glancing exit angles occur. These are precisely those for which the semiclassical approximation is least valid. The section of the distributions far from the specular is thus the least accurate. Fortunately, it is the phenomena which occur far from this region, near the specular, we are interested in.

#### 4.3 Discussion

Qualitatively, both the anomalous features in the [110] data can be explained at  $\theta_o = 59^\circ$  with  $V_o = 100$  K and  $Z_o = 0.16 \text{ \AA}$ . The small peaks near  $\eta = 55^\circ$  and  $\eta = 70^\circ$  generally disappear below  $Z_o = 0.14 \text{ \AA}$ . Similar calculations at  $\theta_o = 30^\circ$  and  $\theta_o = 51^\circ$  for these potential parameters are

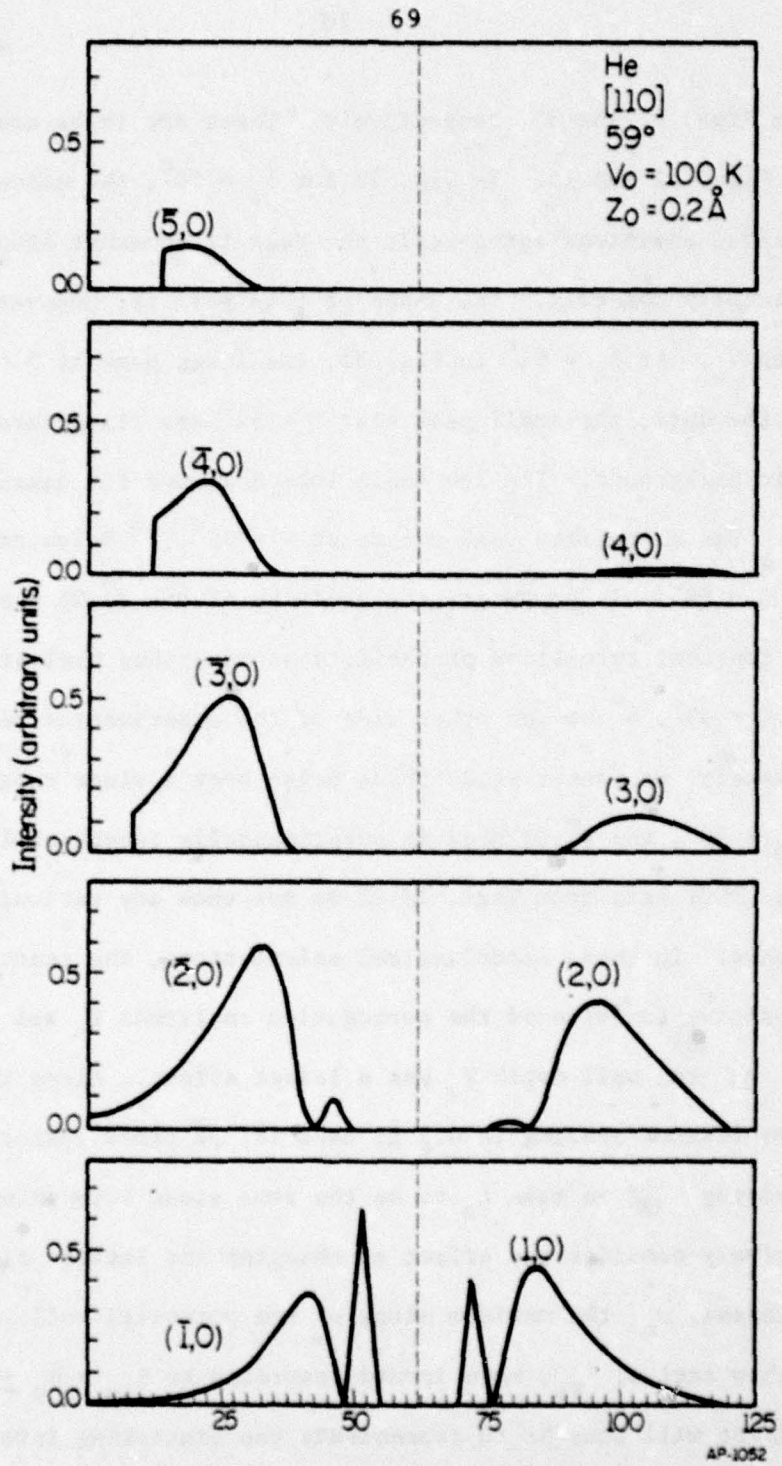


Fig. 31. Calculated semiclassical diffraction peak profiles for MgO (001), [110] azimuth. Helium scattering averaged over thermal beam at 300 K. The individual diffraction peaks up to  $|n| = 5$  are shown for  $V_0 = 100$  K,  $Z_0 = .2 \text{ \AA}$ , at  $\theta_0 = 59^\circ$ . The total profile, as displayed in previous figures, is the sum of these individual distributions.

shown in Figs. 32 and 33, respectively. These are to be compared to the data in Figs. 12 and 15. In Fig. 32 for  $\theta_o = 30^\circ$ , the calculated and experimental positions agree well; the peak is somewhat broader than experimentally observed. The shape of this peak is, however, quite sensitive to  $V_o$ . At  $\theta_o = 51^\circ$  in Fig. 33, the large peak at  $\eta = 99^\circ$  fits well to the data; the small peak near  $\eta = 89^\circ$  has disappeared into the inelastic background. The low angle lobe does not fit nearly as well, however. The calculated peak occurs at  $\eta = 52^\circ$ ,  $7^\circ$  below the experimental peak at  $\eta = 59^\circ$ . In contrast, the position of the  $(\bar{1}, 0)$  peak calculated using a constant transition probability as described earlier gives a peak at  $\eta = 63^\circ$ ,  $4^\circ$  to the other side of the experimental peak. Unfortunately, we cannot study these peaks over a wider range of  $\theta_o$ ; above  $\theta_o = 50^\circ$ , the  $(\bar{1}, 0)$  peak is experimentally inaccessible.

The [100] data from Figs. 18-21 do not show any serious shifts of extra peaks. In these semiclassical calculations, the scattering profile is a sensitive function of the corrugation amplitude  $Z_o$  and the lattice spacing  $a$ ; the well depth  $V_o$  has a lesser effect. Along the [100] the effective lattice spacing is  $4.2 \text{ \AA}$ , that is,  $\sqrt{2}$  times longer than the [110] spacing. If we take  $Z_o$  to be the same along both azimuths, we can qualitatively consider the effect of changing the lattice dimension. As  $a$  increases,  $\alpha_m$ , the maximum slope of the potential wall, decreases. The rainbow angles,  $\theta_{Rm}$ , move inward according to  $\theta_{Rm} = \theta_o \pm \alpha_m$ . A major effect will thus be to concentrate the scattering into a narrower angular region; all other things equal, we would thus expect the scattered distribution to become sharper and taller.

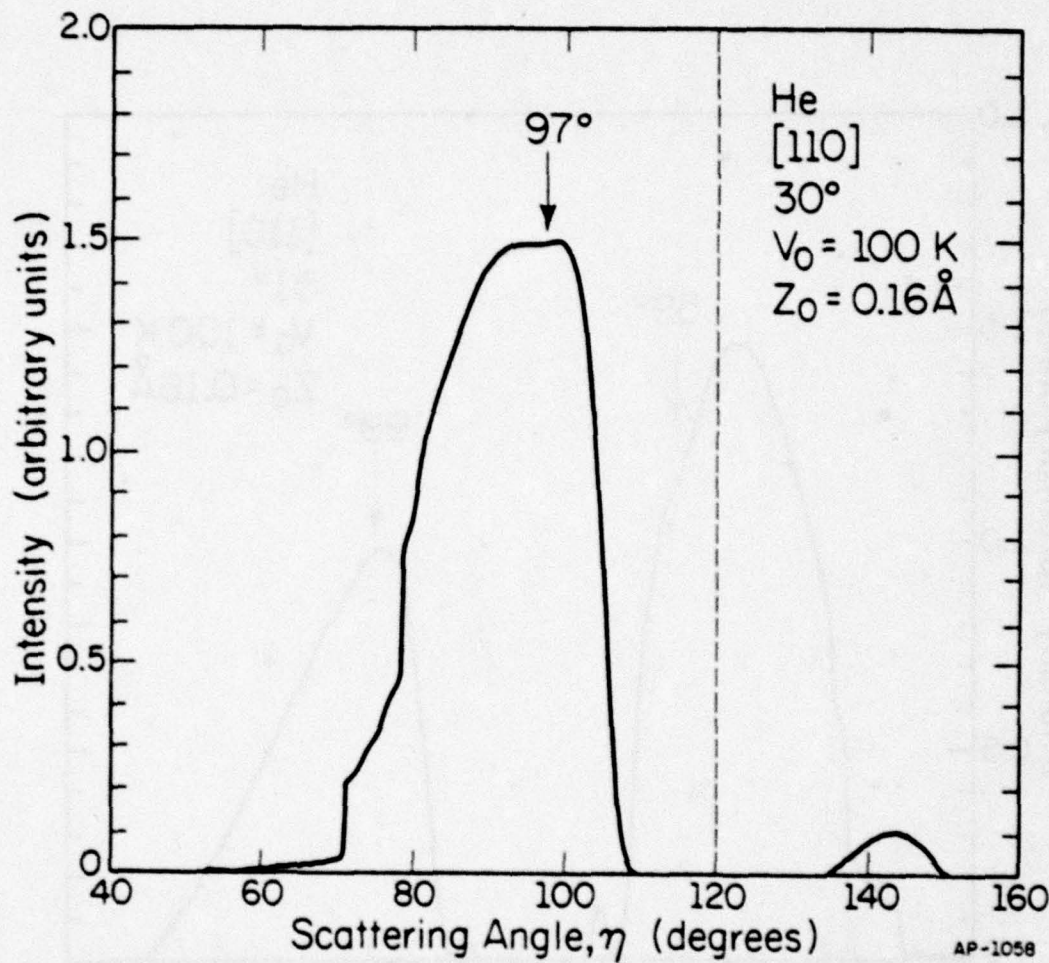


Fig. 32. Calculated semiclassical distribution for helium scattering at  $\theta_0 = 30^\circ$ .  $Z_0 = .16 \text{ \AA}$  and  $V_0 = 100 \text{ K}$ . The experimental peak position from Fig. 12 is indicated. The small bump near  $\eta = 140^\circ$  is the  $(1,0)$  diffraction peak which is energetically closed to most of the beam molecules.

80

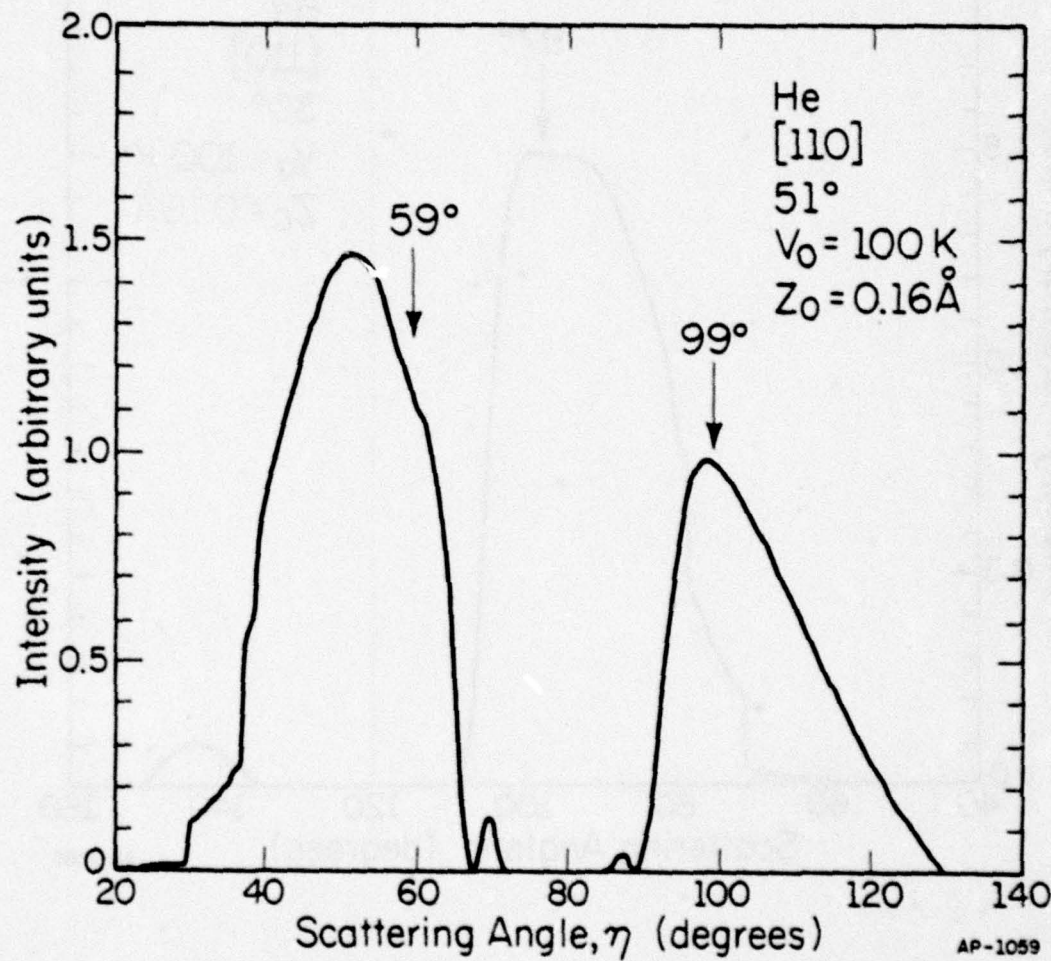


Fig. 33. Semiclassical distribution for  $\theta = 51^\circ$ ,  $Z_0 = .16 \text{ \AA}$ ,  $V_0 = 100 \text{ K}$ .

For comparison with experimental data in Fig. 15. Experimentally observed peaks indicated by an arrow. Only the portion at  $\eta > 50^\circ$  is experimentally accessible.

Semiclassical calculations have been done along the [100] azimuth using the same procedure as for the [110]. It was not possible, however, to fit the experimental peak positions to the calculations using the same potential parameters as determined for the [110]. The same corrugation amplitude,  $Z_0 = 0.16 \text{ \AA}$ , was used but a much deeper well,  $V_0 = 200 \text{ K}$  was required. Calculated distributions using these parameters for  $\theta_0 = 60^\circ$  and  $\theta_0 = 30^\circ$  are shown in Figs. 34 and 35 for comparison with the data in Figs. 21 and 18. The positions of the major peaks fit well. However, for  $\theta_0 = 60^\circ$  in Fig. 34, the small peak near  $\eta = 67^\circ$  is not visible in the data even though a similar peak was clearly visible in the [110] data. We can only conclude that it has become lost in the inelastic tail of the specular peak. The peak at  $\eta = 96^\circ$  for  $\theta_0 = 30^\circ$  in Fig. 35 also fits well to the data. The small lobe to the right of the specular angle, near  $140^\circ$ , is the high energy tail of the  $(\bar{1}, 0)$  diffraction peak. This channel is energetically closed to a significant fraction of the beam molecules. This small lobe is not observed in the data.

It should not be surprising that a different potential is required along the [100] than along the [110]. As shown in Fig. 1, the [110] is the direction between nearest like ions on the surface, whereas the [100] direction passes through alternate positive and negative ion cores.

Tsuchida<sup>50</sup> has calculated the helium-LiF potential by summation of pairwise interactions. The He-MgO interaction should be qualitatively similar. The  $V = +1000 \text{ cal/mole}$  equipotential surface of this potential is shown schematically in Fig. 36. One quarter of the unit cell is shown.

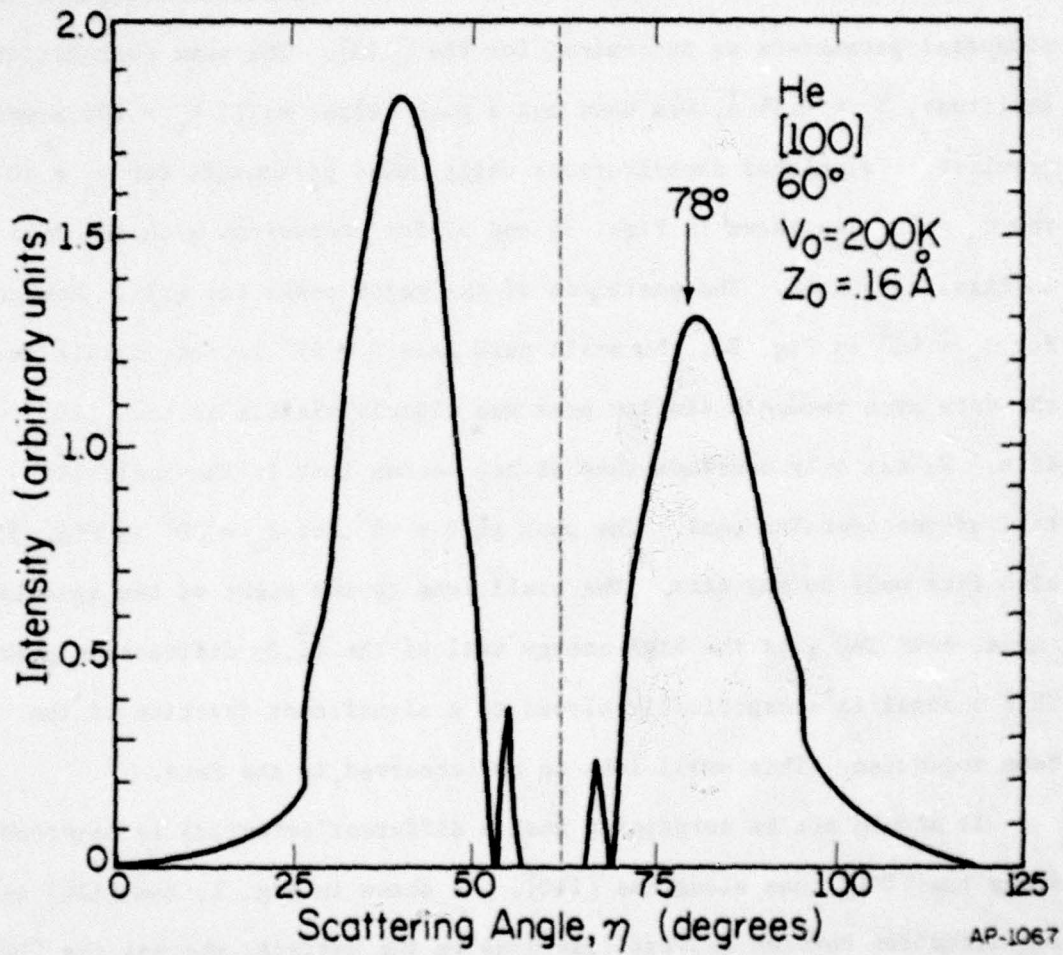


Fig. 34. Semiclassical calculation for [100] azimuth.  $\theta_0 = 60^\circ$   
 $Z_0 = 0.16\text{ \AA}$ ,  $V_0 = 200\text{ K}$ . Experimental peak denoted  
by arrow.

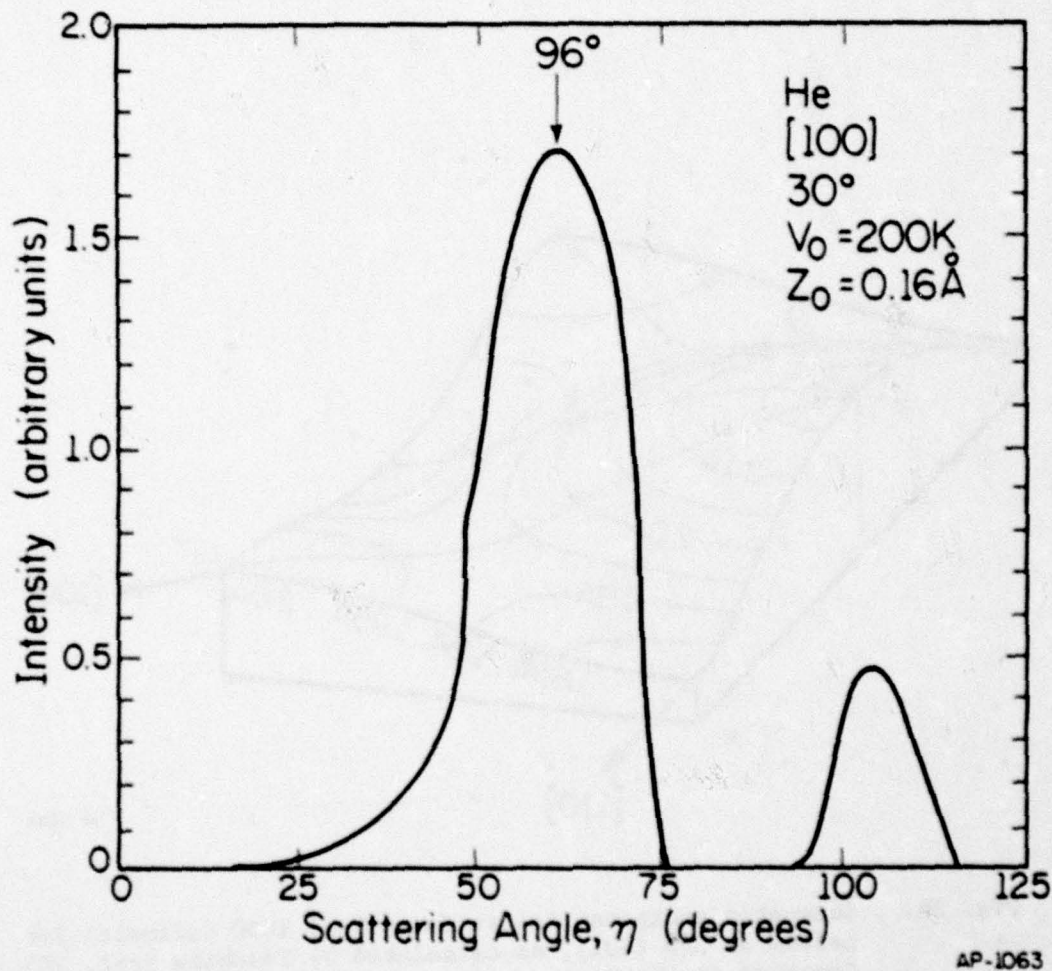


Fig. 35. Semiclassical calculation for [100] azimuth. Experimental peak denoted by arrow.  $Z_0 = 0.16\text{ \AA}$ ,  $V_0 = 200\text{ K}$ ,  $\theta_0 = 30^\circ$

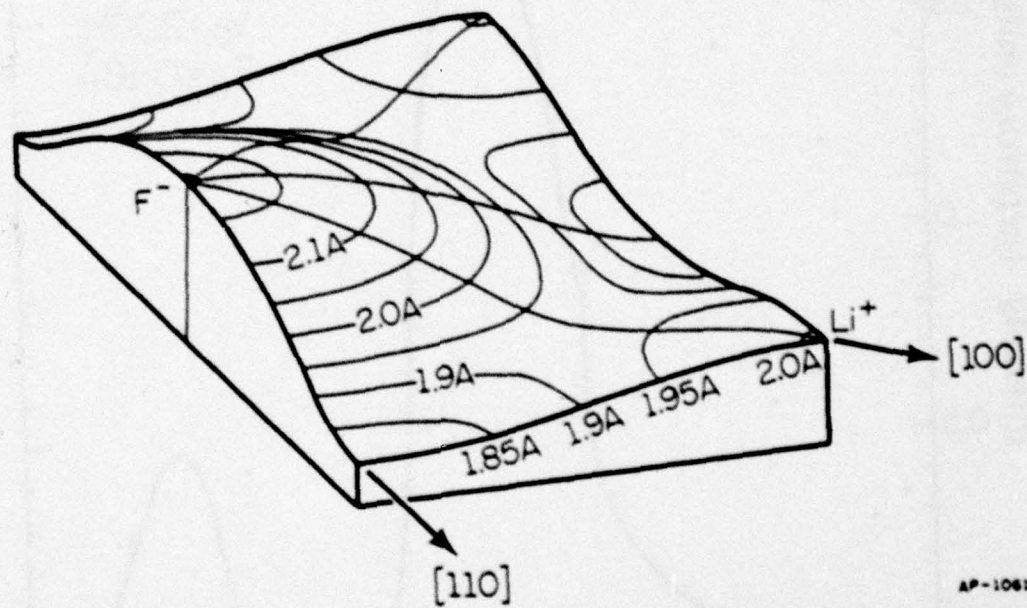


Fig. 36. Schematic equipotential surface ( $V = +1000$  cal/mole) for helium on LiF (001), as calculated by Tsuchida (ref. 50). Contours denote distance from surface in angstroms.

The contours represent the distance from the surface plane to the equipotential. Since the mean energy in a beam at 300 K is 1192 cal/mole, this surface approximates the classical turning point surface and can be roughly compared to our hard wall. Along the [110] the equipotential appears to be a simple sinusoidal function of distance, with the valley midway between the like ions. In fact, the effective roughness of Tsuchida's potential, similar to our  $Z_o$ , is 0.17 Å along the [110], in excellent agreement with our 0.16 Å. This is, however, perhaps fortuitous. Along the [100] azimuth, the potential is more complex with 2 maxima per unit cell. Thus it may be that our model potential is too simple to handle scattering along the [100] azimuth. A more realistic potential, such as Tsuchida's, could be handled by the same semiclassical formalism we have used. It would require, however, numerical integration of the classical equations of motion through the potential. Note that since there are 4 inflection points per unit cell along the [110] for this potential, there will in general be 4 contributing trajectories instead of the two in our calculation. This could significantly change the interference structure in the scattered distributions. Although such a calculation could be done, it would be extensive and it thus would defeat one of our main purposes, that is, to have as simple calculational scheme to aid in experimental interpretation.

The potential parameters determined here should be considered only an approximation. The model is not intended to be quantitative. Although the calculation works well for most of the data, the position of the low  $\overline{I}$  peak at  $\theta_o = 51^\circ$  on the [110] as well as the absence of the small

peaks in the data  $\theta_0 = 60^\circ$  on the [100] remain troublesome. This should not, however, be due to a deficiency in the semiclassical approximation but rather due to inadequacies in the model potential and the artificial limitation to in-plane scattering. The primary purpose of these calculations has, however, been served; that is to qualitatively explain the experimental peak positions and fine structure. We conclude that the transition probability for elastic diffraction,  $T_n(\lambda)$ , is a strong function of wavelength. In addition, there is considerable intensity in the higher order diffraction peaks up to  $|n| = 5$ . It is the superposition of these peaks, each having its own structure dictated by  $T_n(\lambda)$ , which results in the experimentally observed distributions.

A comment on the use of a thermal beam for elastic diffraction studies is in order. Our calculations indicate significant diffraction intensity out to  $|n| = 5$ . Not only are the individual diffraction peaks broad due to the distribution of velocities in the beam distribution, but there is also extensive peak overlap. The fine structure and intensities of the individual peaks are thus not observable with a thermal beam. Considerable information is lost. It is clear that quantitative studies of the gas-surface potential through elastic diffraction of molecular beams require a monoenergetic beam.

## CHAPTER 5

## SCATTERING OF HYDROGENIC MOLECULES

5.1 Experimental Results: HD

In this chapter we will present the scattering of the hydrogenic molecules H<sub>2</sub>, D<sub>2</sub>, and HD from the (001) plane of MgO along the [110] incident azimuth. We wish to investigate the participation of rotational modes of simple molecules in gas surface scattering. Particular emphasis will thus be placed on the scattering of HD, as the rotational modes of this molecule most strongly couple to the surface. Data were taken with the surface at 300 K, for beam temperature at both 300 K and 80 K.

The results of scattering experiments with HD at a beam temperature of 300 K are shown in Figs. 37-41. Upon comparison with the helium measurements presented earlier, several differences are immediately apparent. There is considerably more inelastic scattering for HD than for the helium; the specular peak has been severely attenuated, and the diffraction lobes are less well defined. However, despite the large background due to thermal inelastic events and peak overlap, the features are clearly marked. Instead of the smooth, broad diffraction peaks which we observed for helium, the HD distribution is dominated by a series of sharp and very narrow peaks. It is immediately clear that these peaks result from a different process than the essentially elastic diffraction observed for helium scattering. Recalling our discussion in Chapter 2, it appears these peaks are due to rotationally inelastic diffraction processes.

Of particular interest in these distribution is the sharpness of many of the peaks. Although only the tops are visible, they appear to be

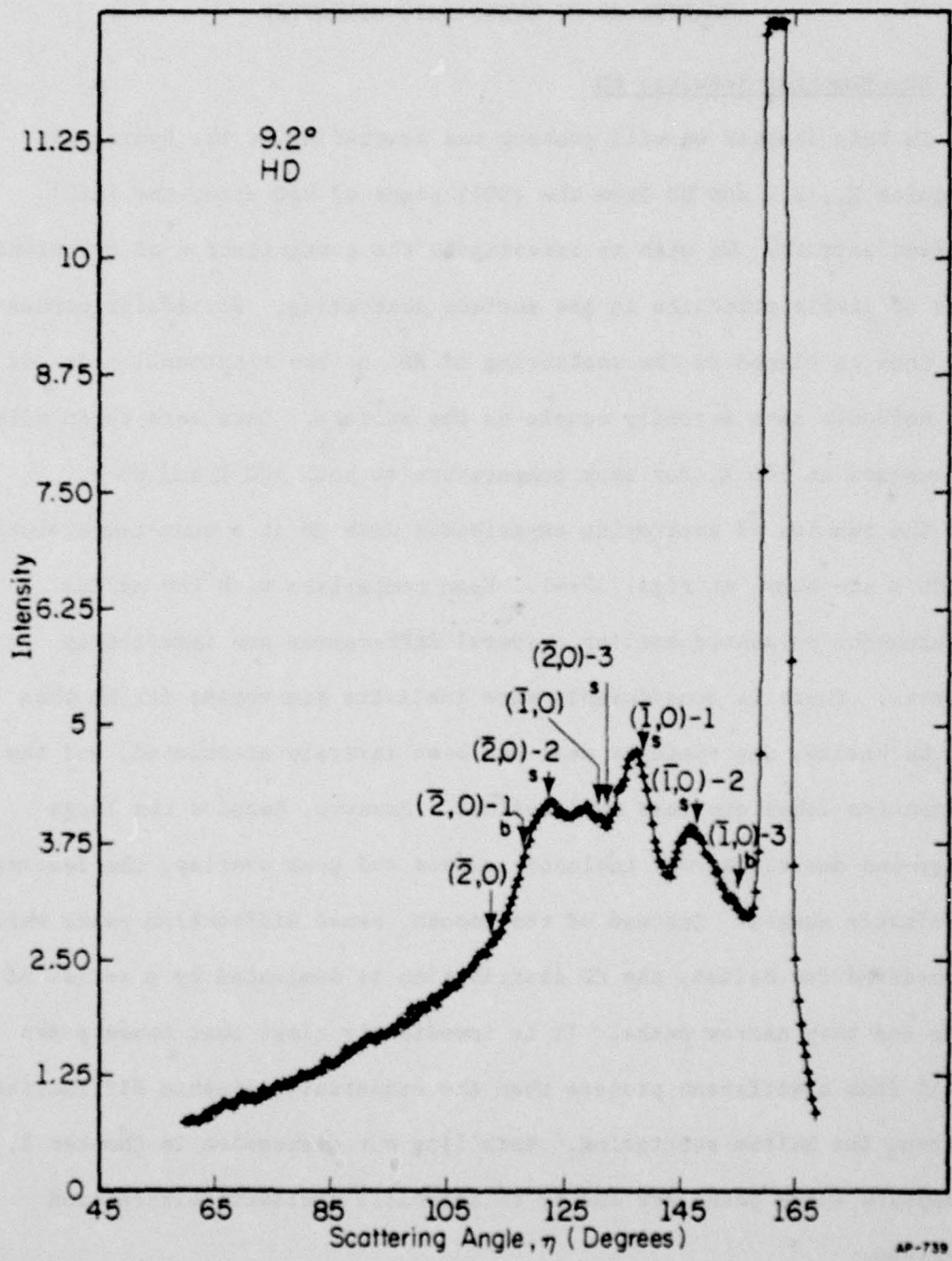


Fig. 37. HD scattering, MgO (001), [110] azimuth, 300 K beam.  
9.2° incident angle. Specular = 26.3 units.

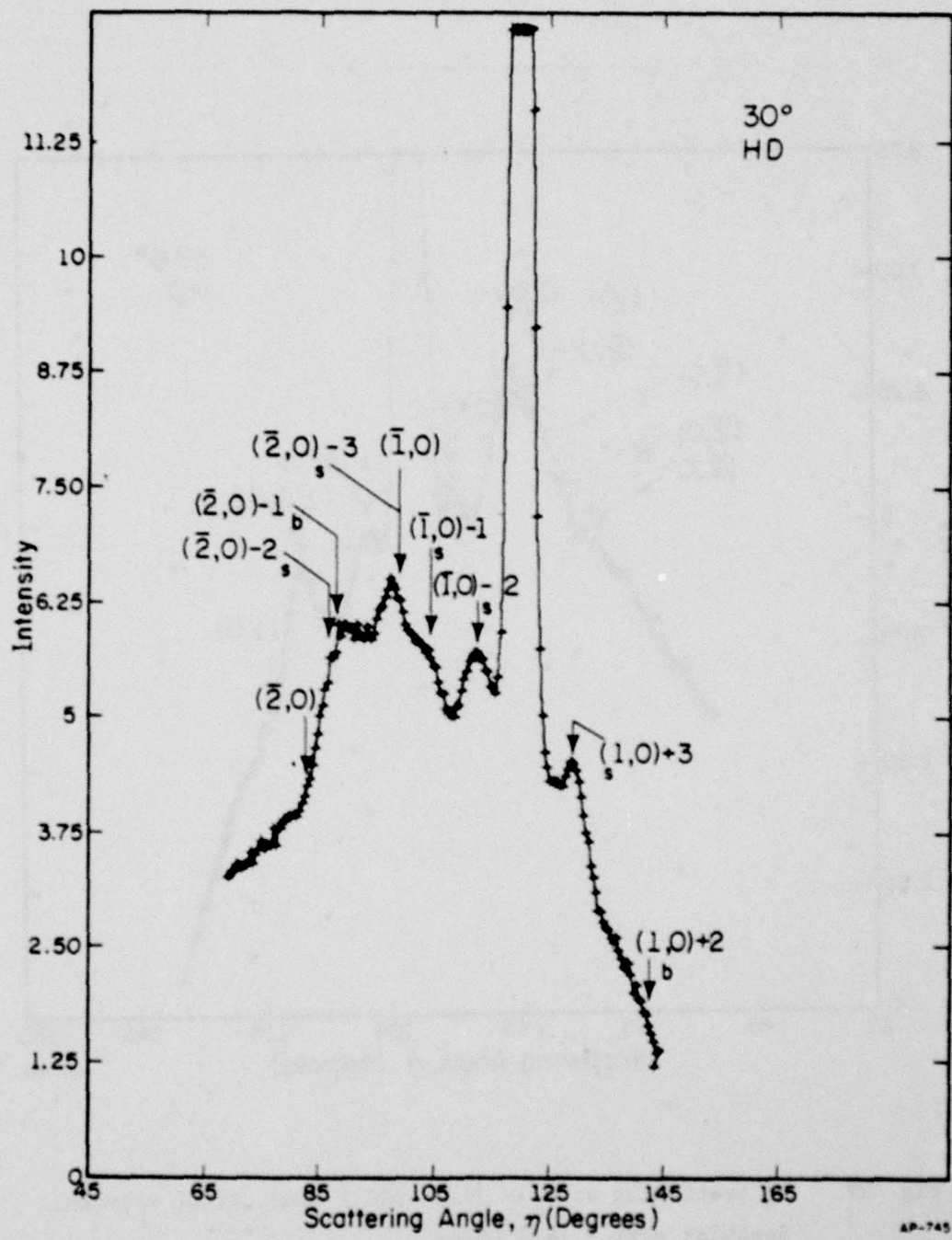


Fig. 38. HD scattering, MgO (001), [110] azimuth,  $\theta_0 = 30^\circ$   
300 K beam. Specular = 21.7 units.

70

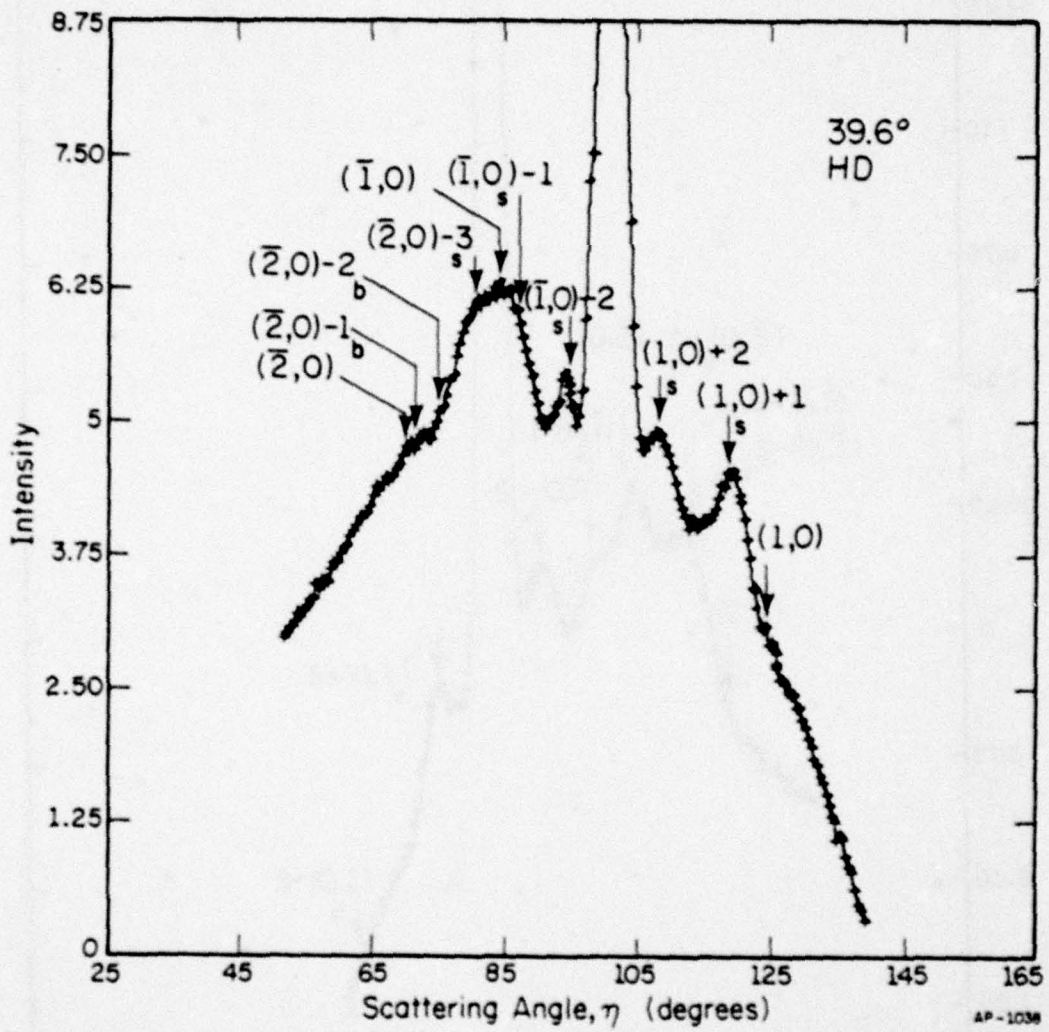


Fig. 39. HD scattering at  $\theta_0 = 39.6^\circ$  300 K beam, [110] azimuth.  
Specular peak = 16.2 units.

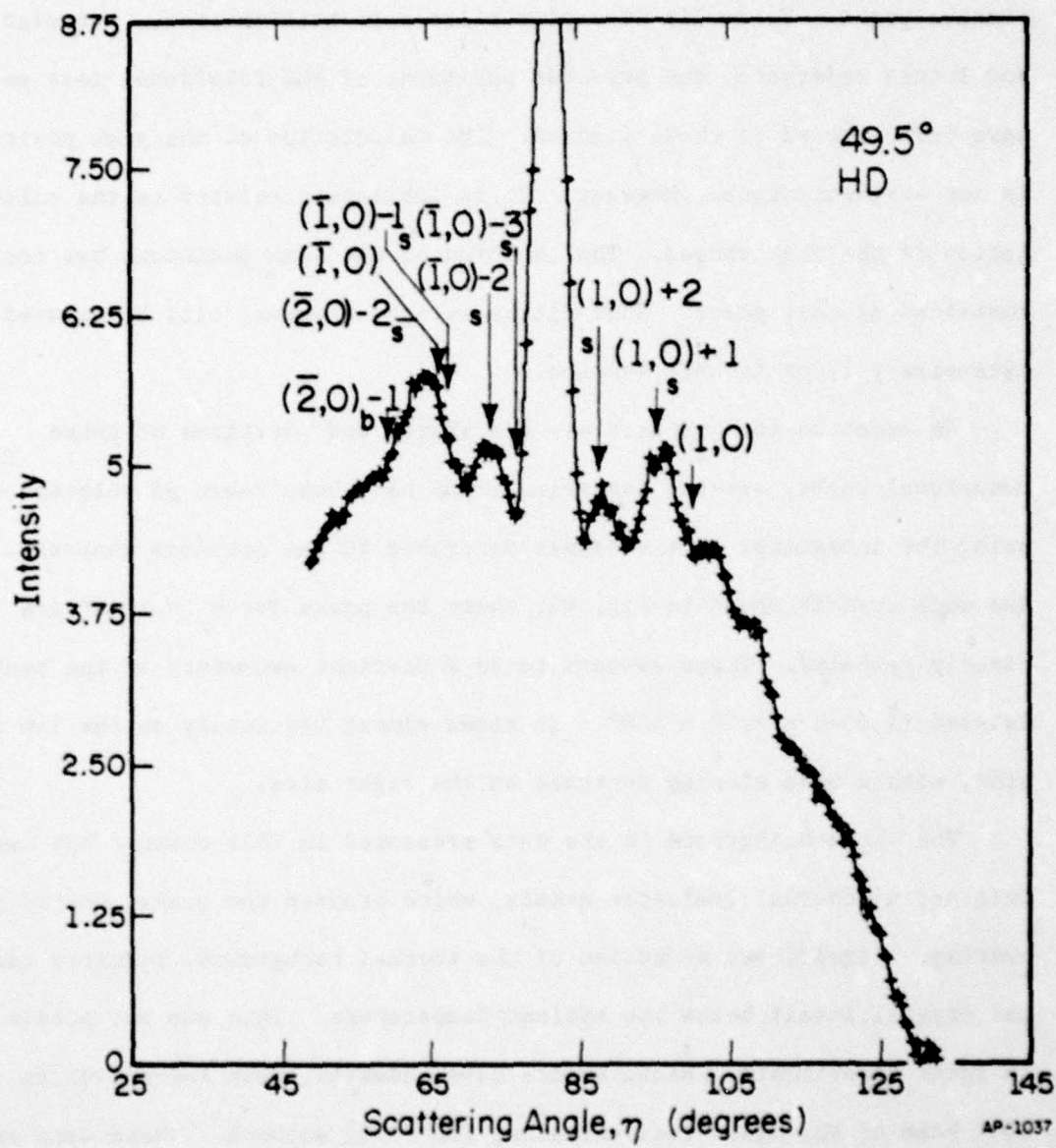


Fig. 40. HD scattering,  $\theta_0 = 49.5^\circ$ , [110] azimuth. Specular peak = 11.9 units.

considerably narrower than the elastic peaks we saw for helium. This raises a question: why should the inelastic peaks be narrower than the elastic peaks. This will be explored later in this chapter. For clarity and future reference, the expected positions of the rotational loss peaks have been labeled in these figures. The calculation of the peak positions is not straightforward, however. It is intimately related to the calculation of the peak shapes. The labeling of the peak positions has not been justified at this point. This entire matter, however, will be covered extensively later in this section.

In order to more clearly see the shapes and positions of these rotational peaks, several low noise scans have been taken of selected areas, using the integrator in the manner described in the previous chapters. One such scan is shown in Fig. 41, where the peaks for  $\theta_0 = 13.2^\circ$  are clearly revealed. There appears to be a distinct asymmetry in the peak labeled  $(\bar{1},0)-1$  near  $\bar{\eta} = 130^\circ$ . It rises almost vertically on the low angle side, with a more sloping decrease on the right side.

The large background in the data presented in this chapter has two origins; a) thermal inelastic events, which broaden the peaks, and b) peak overlap. Significant reduction of the thermal background, requires cooling the crystal itself below the ambient temperature. This was not possible in these experiments. Measurements have, however, been taken with an 80 K beam of HD, again incident along the [110] azimuth. These data are shown in Figs. 42-44. Recalling that  $\lambda = h/p \approx h/\sqrt{2M_g kT}$ , and

$$\cos\theta = \cos\theta_0 + n\lambda/d, \quad (4)$$

we expect the elastic diffraction peaks to move outward, away from the specular, as the temperature of the beam is lowered. By lowering T,

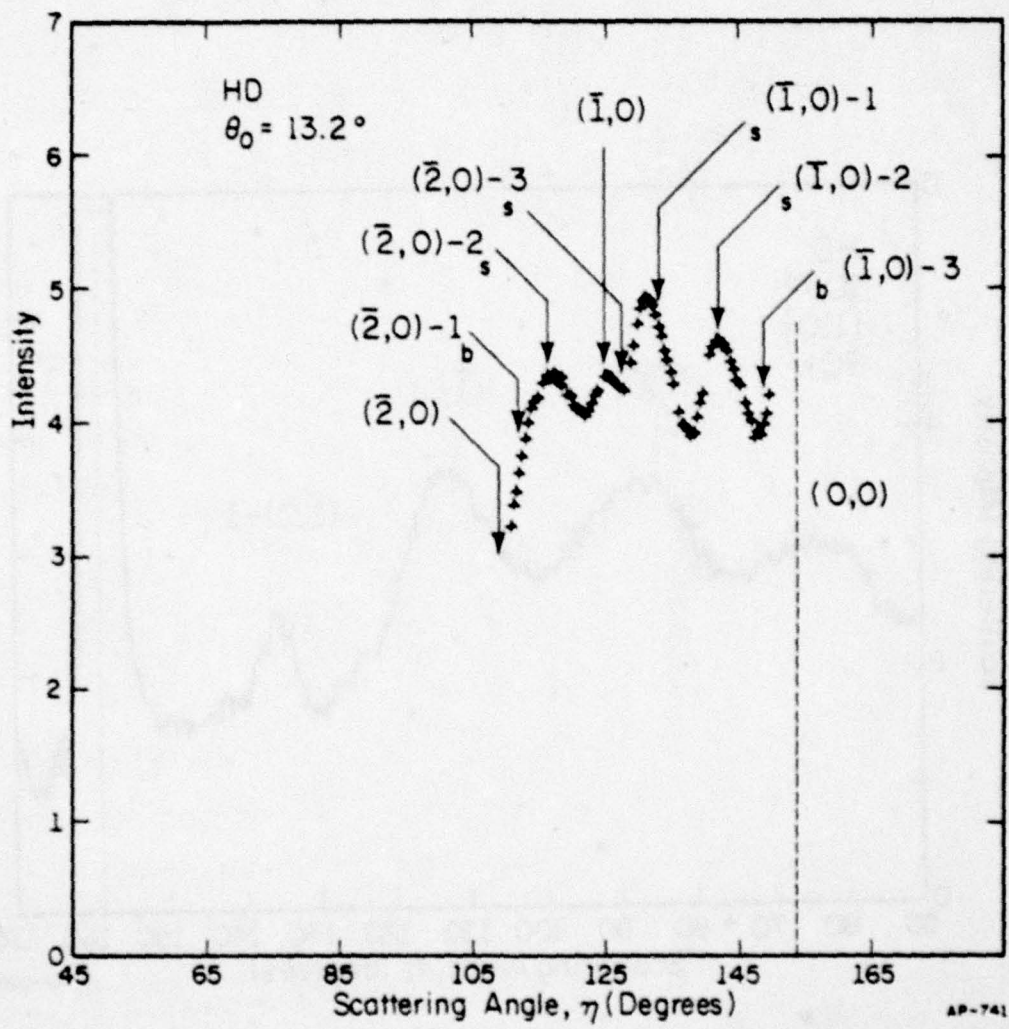


Fig. 41. Slow, low noise scan of selected portion of distribution showing sharp rotational peaks.  $\theta_0 = 13.2^\circ$  for HD, [110] azimuth. Data taken at 60 sec. time constant, 60 sec. per point.

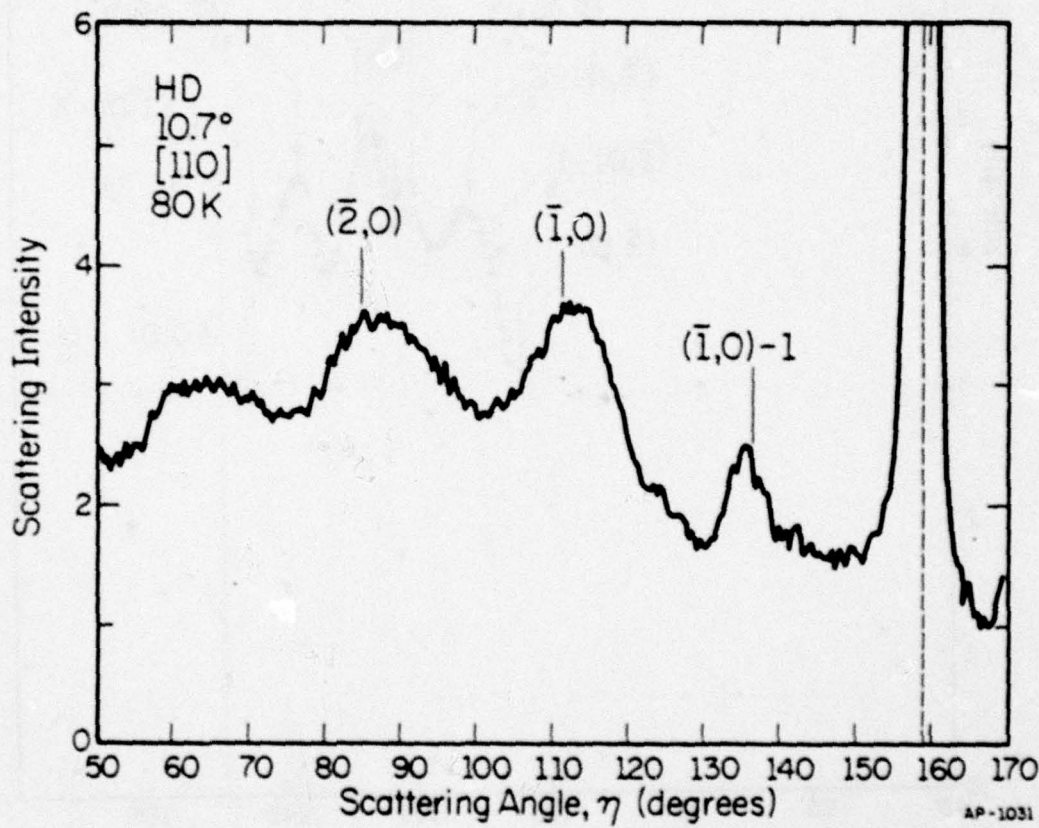


Fig. 42. HD scattering at 80 K. [110] azimuth.  $10.7^\circ$  incident angle.

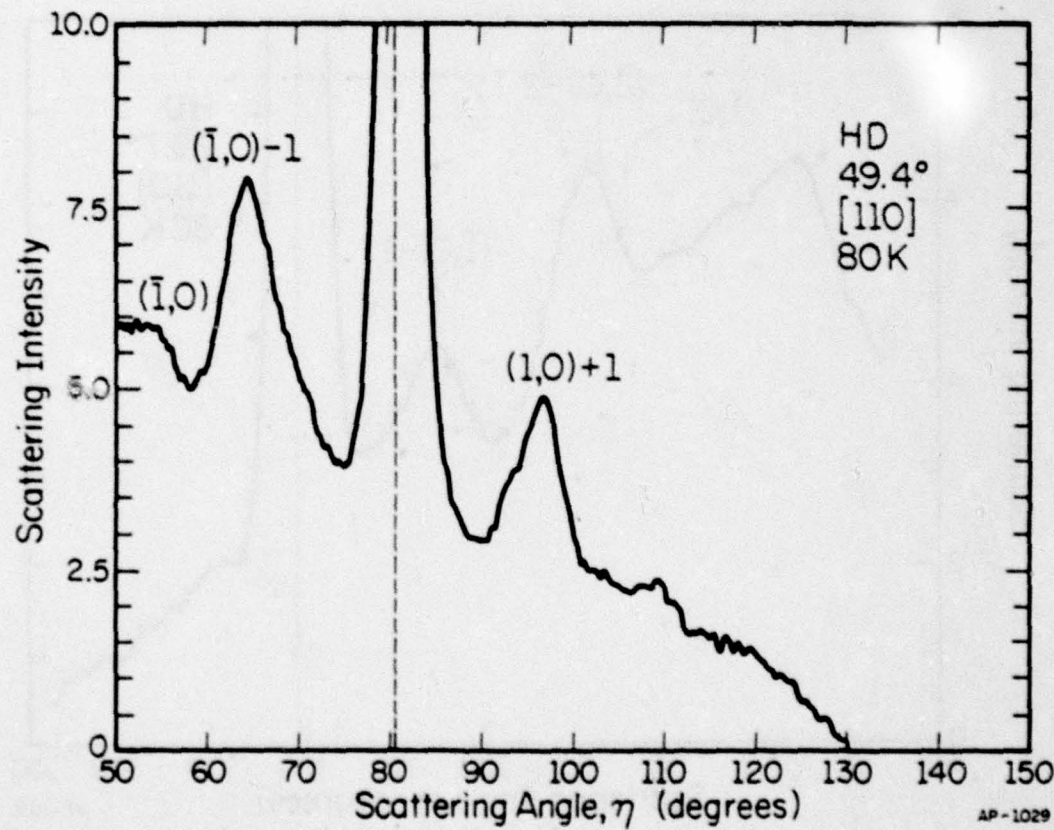


Fig. 43. HD scattering, 80 K beam, [110] azimuth,  $49.4^\circ$  incident angle.

AD-A077 151

ILLINOIS UNIV AT URBANA-CHAMPAIGN COORDINATED SCIENCE LAB F/G 7/4  
EXTREMAL EFFECTS IN ROTATIONALLY INELASTIC DIFFRACTION. (U)  
MAR 79 L C RATHBUN DAAB07-72-C-0259  
R-840 NL

UNCLASSIFIED

2 OF 2  
AD-  
A077151



END  
DATE  
FILMED  
12-79  
DDC

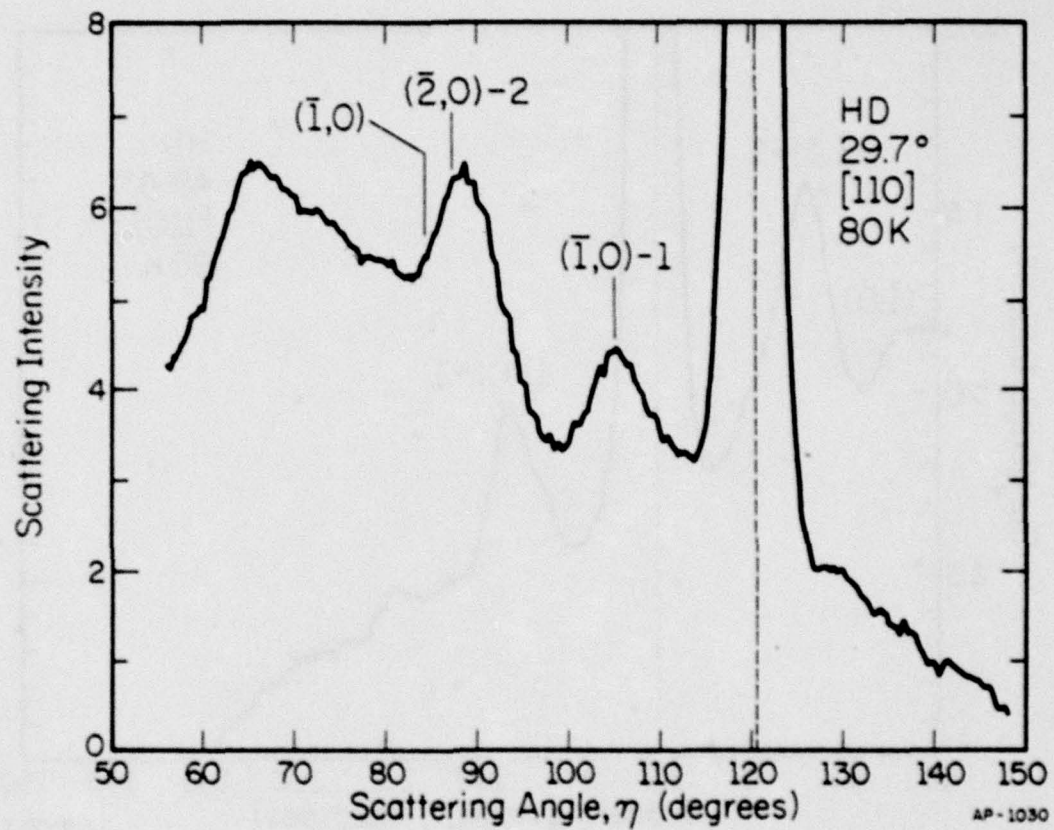


Fig. 44. HD scattering for 80 K beam. Incident angle = 29.7°.  
[110] azimuth.

we can hope to decrease peak overlap and more clearly resolve the individual peaks.

Lowering the temperature of the source has effects other than changing  $\lambda$  and shifting the peaks outward. Cooling the beam will also shift the distribution of rotational states toward lower  $J$ , as shown in Fig. 45. Furthermore, as  $T$  is lowered, that is, as the energy of the beam is lowered, fewer elastic scattering channels are open. One effect of this can be seen in comparing Fig. 37 to Fig. 42, for scattering at approximately  $\theta_0 = 50^\circ$  at 300 K and 80 K respectively. The specular intensity (i.e. the elastic, non-diffracted intensity) is approximately twice as large at 80 K as at 300 K.

### 5.2 Extremal Effects

Of particular interest in the data is the apparent sharpness of the peaks, as well as their peculiar shape. Furthermore, it can be noted that although some of the transitions are strong, others are not observed at all, for example, at  $\theta_0 = 30^\circ$ , the  $(\bar{1}, 0) + 2$  is clearly visible but not the  $(\bar{1}, 0) + 3$ . The reason for these effects becomes apparent if we examine more closely the mechanism involved.<sup>51,52</sup>

Recalling Eq. (5), rotationally inelastic diffraction can be described by

$$k^2 = k_0^2 + \frac{2M\Delta E}{h^2} \quad (\text{conservation of energy}) \quad (5a)$$

$$\vec{k} = \vec{k}_0 + \vec{G}_{nm} \quad (\text{conservation of momentum}), \quad (5b)$$

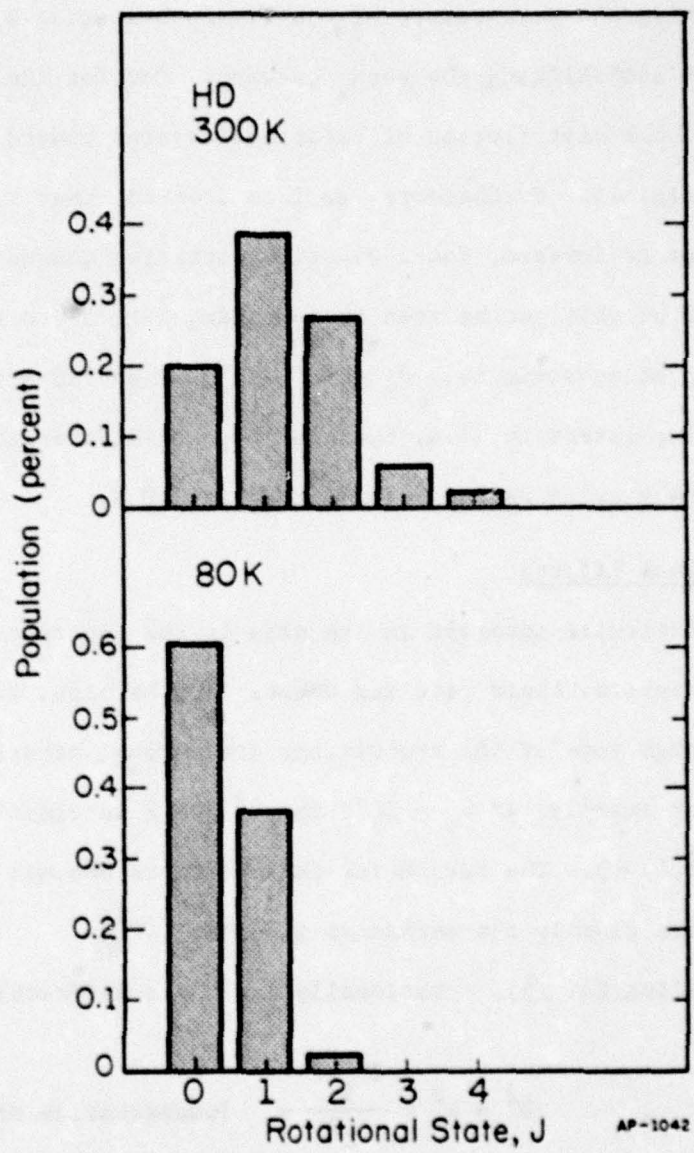


Fig. 45. Rotational state population for normal HD at 300 K and 80 K, from Table 1.

where again  $\vec{k}_o = (\vec{k}_o, k_{oz})$  and  $\vec{k}$  are the incident and scattered wave vectors, respectively, and  $\Delta E$  is the energy transferred from rotation to translation. Note that for inelastic scattering, the scattered wavelength,  $\lambda$ , is no longer equal to the incident wavelength,  $\lambda_o$ . We will at present confine ourselves to in-plane scattering along the [110] azimuth; for this case  $m=0$  and the inelastic diffraction peaks are labeled  $(n,0) \pm 1$ . From Eq. (5) we previously obtained Eq. (6) for the scattered angles

$$\cos\theta = \frac{\lambda}{\lambda_o} \left( \cos\theta + \frac{n\lambda}{d} \right) \quad (6a)$$

$$\frac{\lambda}{\lambda_o} = [1 + 2\Delta EM_g \frac{\lambda_o^2/h^2}{\lambda^2}]^{-\frac{1}{2}} \quad (6b)$$

Although at first these relations appear normal, on closer examination, peculiar behavior is observed. Consider the case of a loss transition from the  $(1,0)$  diffraction peak, for which both  $\Delta E$  and  $n$  are negative. In this instance,  $\lambda/\lambda_o$  is an increasing function of wavelength, whereas  $\cos\theta_o + \frac{n\lambda}{d}$  is a decreasing function.  $\cos\theta$  is the product of these two terms and thus the relationship can be double valued, that is, it may have a turning point. Such a relation between  $\lambda_o$  and  $\theta$  is shown in Fig. 46, where it is important to recall that  $\theta$  and  $\pi$  are related by  $\pi = 180 - \theta_o$ .

The effect of this extremum on the rotational inelastic peaks can now be clearly seen. We know that the differential scattering intensity  $\frac{dF}{d\theta}$  can be written as

$$\frac{dF}{d\theta} \approx Z(I)T(\lambda_o)f(\lambda_o) \frac{d\lambda_o}{d\theta} \quad , \quad (35)$$

where  $T(\lambda_o)$  and  $f(\lambda_o)$  are the transition probability and the wavelength.

100

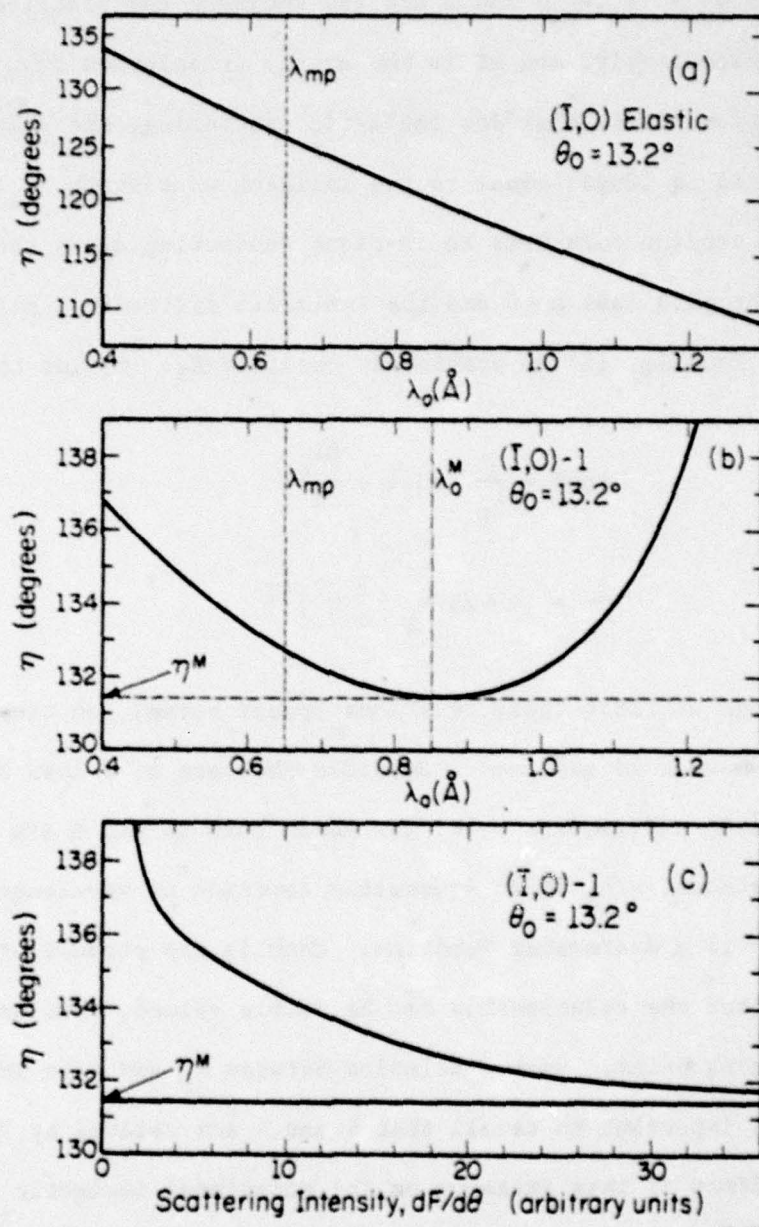


Fig. 46. In-plane scattering of HD of MgO (001) azimuth  $\theta_0 = 13.2^\circ$ .  
 a) Scattering angle as a function of  $\lambda_0$  for elastic  $(\bar{1},0)$  peak.  $\lambda_{mp}$  is the most probable wavelength in the beam.  
 b) Scattering angle as a function of  $\lambda_0$  for the  $(\bar{1},0)-1$  rotational loss peak, showing the extremum at  $\lambda_o^M - \eta^M$ .  
 c) Extremal scattering intensity for  $(\bar{1},0)-1$  transition, with singularity at the extremal angle  $\eta^M$ .

distribution respectively.  $Z(I)$  is the population of molecules in the proper rotational state for transition I. It is apparent from Fig. 46b that  $\frac{dF}{d\theta}$  become infinite at the turning point, that is, at the angle  $\theta = \theta_m$ . This is shown in Fig. 46c.

This simple argument predicts a singularity in the scattering intensity for these rotational processes at certain scattered angles,  $\theta_m$ , called the extremal angles. We will denote this process as "extremal scattering". Qualitatively we can understand this process by referring again to Fig. 46. At the extremal angle, a large range of wavelengths is scattered to the same scattered angle. The kinematics of the inelastic scattering process have acted to focus the scattered particles. This is in contrast to the elastic diffraction peaks, where each wavelength goes to a different angle. Extremal scattering will occur whenever  $\frac{d\lambda}{d\theta} = 0$ . It follows from Eq. (6) that the extremal angle is given by

$$\cos \theta_m = \left(1 + \frac{n^2 h^2}{2d^2 \Delta EM g \cos^2 \theta_0}\right)^{\frac{1}{2}} . \quad (36)$$

The wavelength of the incident molecules scattered at  $\theta_m$  is

$$\lambda_m = nh^2 / 2 \Delta EM g d \cos \theta_0 . \quad (37)$$

Extremal scattering peaks can thus only occur when  $n$ , the diffraction index, and  $\Delta E$  the energy change, have the same sign (nonzero). The extremal scattering peaks will therefore appear between the elastic diffraction peak and the specular (0,0) peak. Although these considerations predict a singularity in the differential scattering intensity, this singularity will be removed by integration over the finite aperture of the detector in

any real experiment. However, we expect these peaks to remain quite distorted and sharp when compared with the elastic scattering peaks.

To get a clear insight into the magnitude of extremal scattering, we have undertaken some calculations to simulate the experimental peak shapes. Calculations were done for two different beam temperatures, 300 K and 80 K. The elastic diffraction peaks will shift outward, away from the specular, as the temperature is decreased and the wavelengths increase. The positions of the extremal peaks, however, given by Eq. (36), depend only on  $M_g$  and  $\Delta E$  and should not change. The shapes should change however, as the wavelength distribution shifts through the singularity.

Several factors should influence the observed shapes and intensities of the rotational peaks. Briefly, the most important are:

- 1) The transition probability,  $T(\lambda)$ , as a function of wavelength.
- 2) The initial wavelength distribution,  $f(\lambda)$ , in this case a modified Maxwell-Boltzmann distribution.
- 3) The extremal focusing mechanism.
- 4) The finite detector resolution.

For the present calculations we will ignore the transition probability as a function of wavelength. This variation is expected to be minor with respect to the expected singularities due to extremal focusing. The simulations were done by solving Eq. (5) for a weighted distribution of several thousand individual wavelengths and integrating the resultant distribution at each angle over the finite detector aperture of 3.25 degrees. These calculations, for a beam of HD incident on MgO (001) along the [110] azimuth, are shown in Figs. 47-50. In each figure, the upper section represents scattering at a beam temperature of 300 K and the lower at 80 K. The

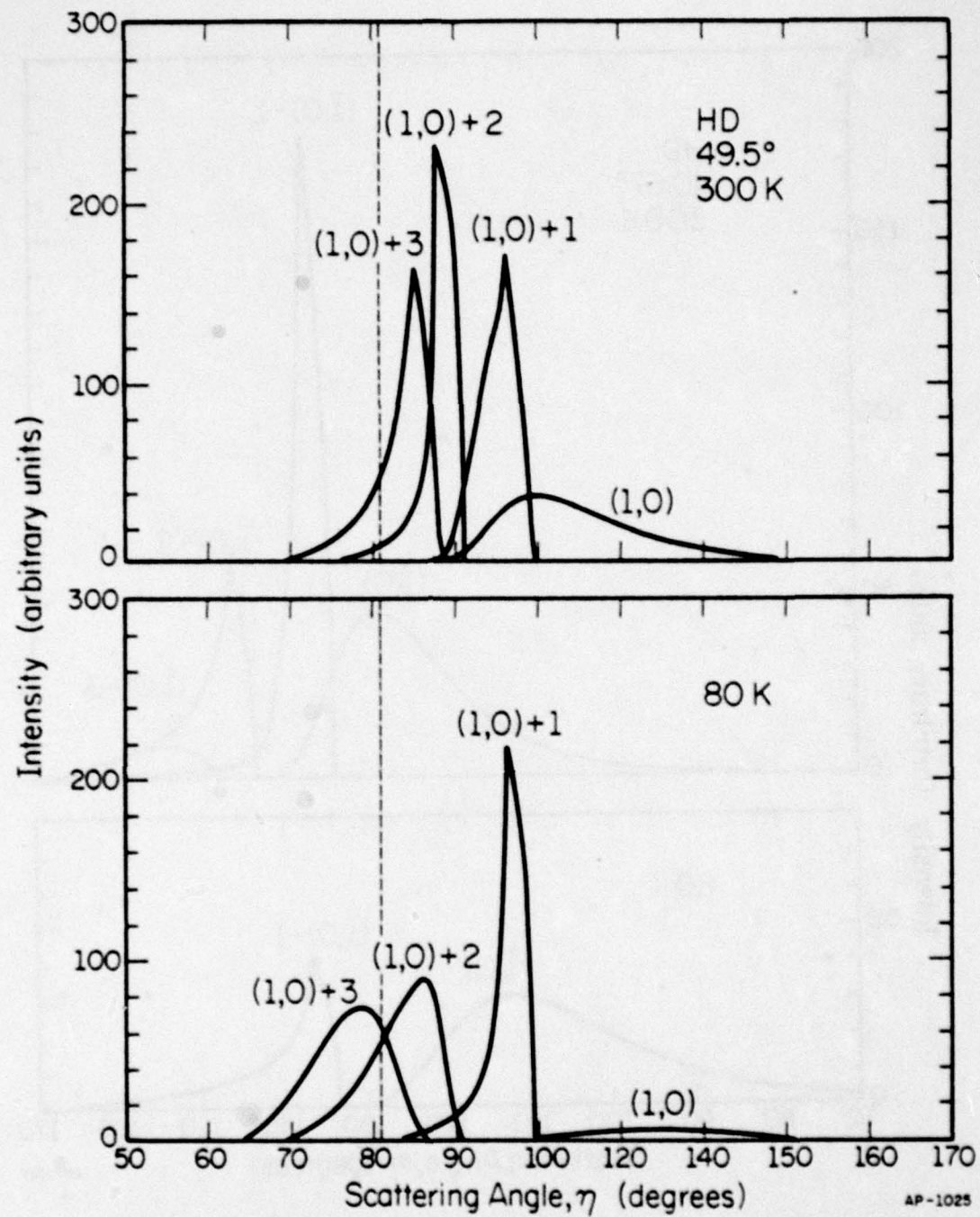


Fig. 47. Calculated extremal scattering peaks for HD from MgO (001), [110] azimuth. 49.5 degrees incident angle.  $(1,0)$  series of inelastic diffraction peaks. Top panel, 300 K beam; lower panel, 80 K beam. Intensity in arbitrary units.  
 $\eta = 180^\circ - \theta - \theta_0$ .

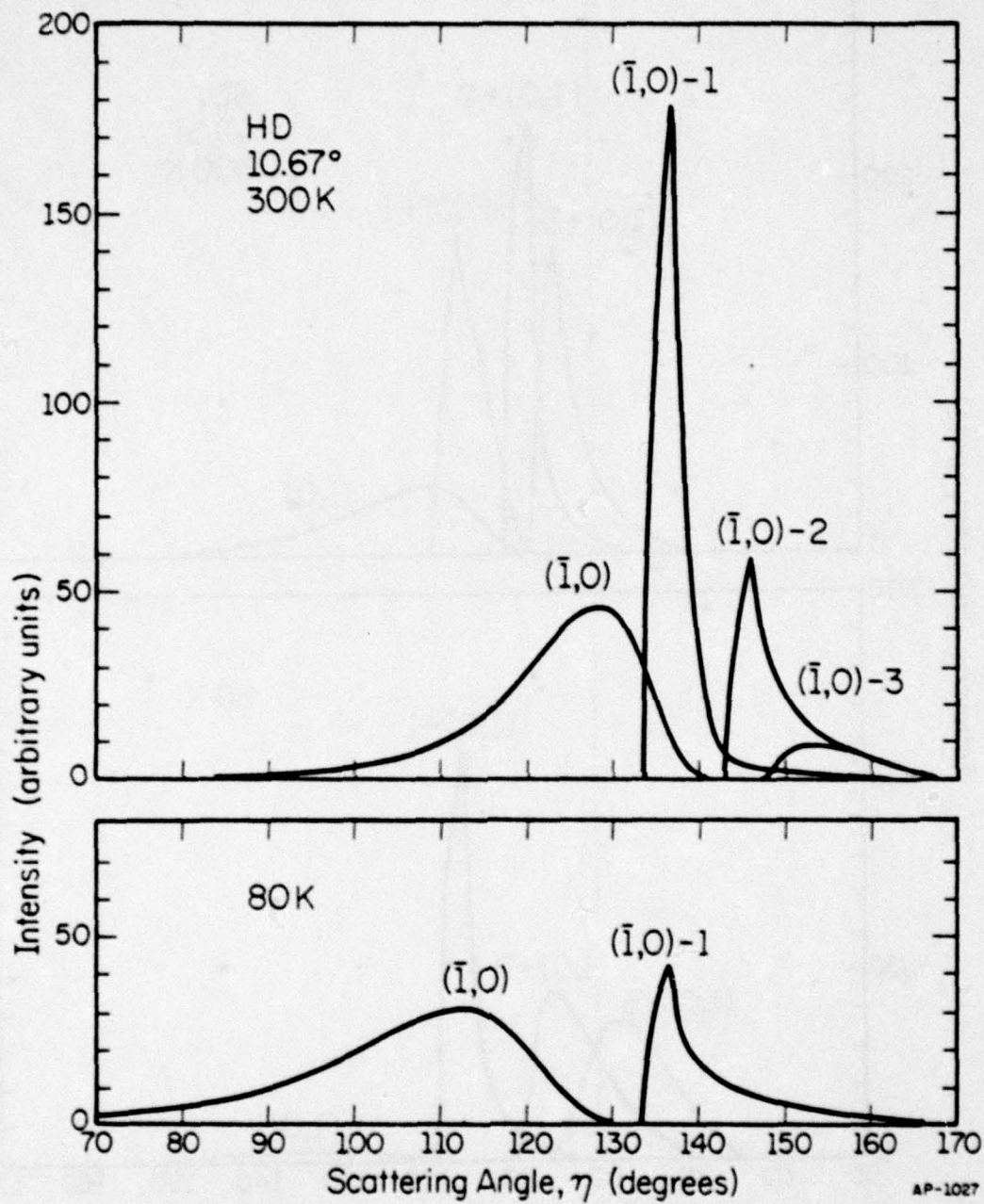


Fig. 48. Calculated extremal peaks for HD at 10.67 degrees incident angle. [110] azimuth,  $(\bar{1}, 0)$  series of inelastic peaks. Upper panel 300 K beam; lower = 80 K. Intensity in arbitrary units.

AP-1027

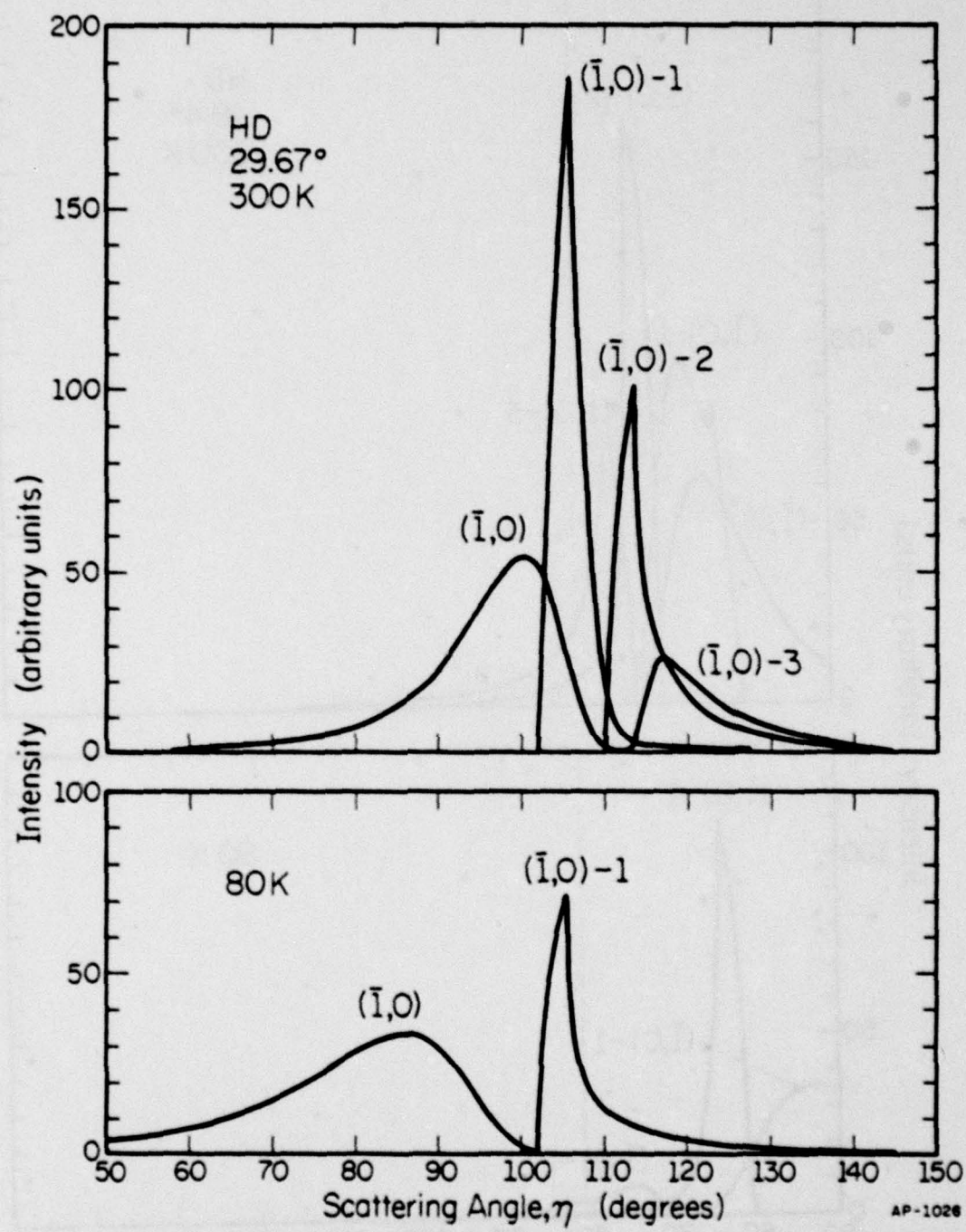


Fig. 49. Same as Fig. 47 except incident angle  $29.67^\circ$ .

AP-1026

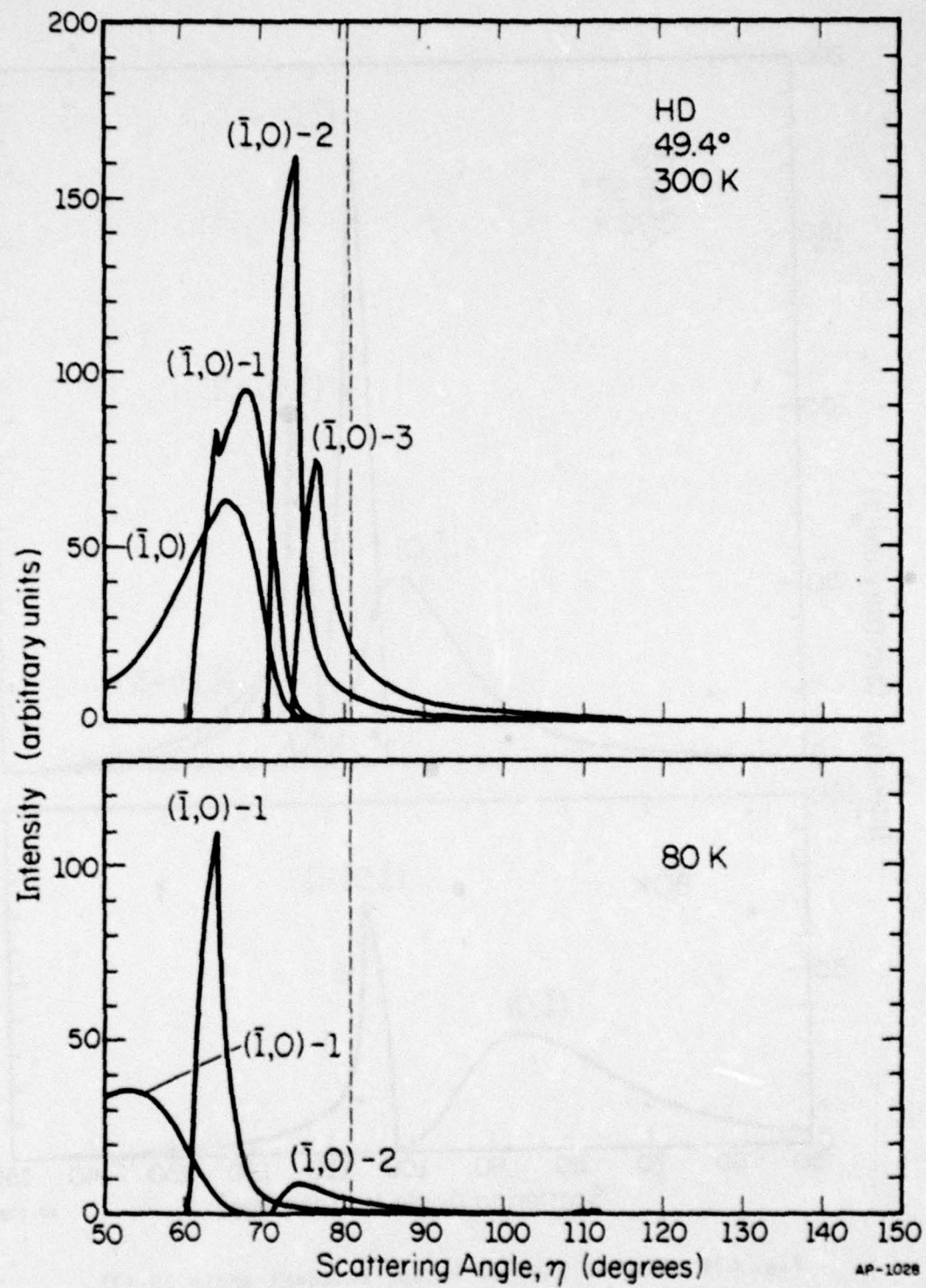


Fig. 50.  $(\bar{1}, 0)$  extremal scattering peaks.  $49.4^\circ$  incident angle for 300 K and 80 K beam. Intensity in arbitrary units.

calculated intensities are plotted vs  $\bar{\theta}$ , the experimental angle. These distributions were calculated assuming an equal number of molecules in each initial rotational state. Only the initial velocities have been Boltzmann weighted; the distribution of initial rotational states will be accounted for later.

Consider for example, the (1,0) set of peaks for  $\theta_0 = 49.5^\circ$ , shown in Fig. 47. At 300 K, the +1, +2, and +3 peaks all exhibit extremal scattering. The peaks rise rapidly on the low angle side and then fall precipitously to zero at the extremal angle. These sharp peaks are what remains of the singularity after integration over the detector aperture. The behavior for  $\theta_0 = 10.67^\circ$  and  $29.7^\circ$  shown in Figs. 48-49 is similar. Here the -1 and -2 transitions clearly show the extremal behavior. The transition (1,0)-3 is different. This peak remains smooth. We recall, however, that the extremal singularity is associated with the scattering of a narrow range of wavelengths near  $\lambda_m$ . For (1,0)-3 at this angle,  $\lambda_m$  is far from the most probable wavelength in the beam. There are thus relatively few beam molecules in the region of the singularity. After integration over the detector, no evidence of it remains. An interesting intermediate case is evident in Fig. 50 for  $\theta_0 = 49.5^\circ$ . Here the (1,0)-1 shows a peculiar double peaked structure: one caused by the peak in  $f(\lambda)$ , the other by the singularity in  $\frac{d\lambda}{d\theta}$ . In all cases, however, the extremal edge occurs, as expected, at  $\theta_m \pm \Delta$ , where  $\Delta$  is the half width of the detector aperture.

At a beam temperature of 80 K, the situation is similar; there are fewer peaks involved, however. These are shown in the lower portions of Figs. 47-50. In going to lower beam temperatures, the elastic peaks have

shifted outward. Most of the higher order rotational peaks have been severely attenuated; they have become energetically closed to a significant portion of the beam population. Furthermore, from Table 1 on page 13, we see that there is an appreciable population of molecules in the initial state only for the +1, -1, and -2 transitions. This will further attenuate the other transitions. As a result, the  $\pm 1$  loss peaks along with the elastic peaks now clearly dominate the distributions. There is little peak overlap to obscure the rotational features. Note that the positions of the extremal edges do not change as the beam temperature is changed.

It should be noted again that not all rotational inelastic transitions are affected by this extremal scattering mechanism. An example of non-extremal transitions is shown in Fig. 51, calculated for helium at 300 K, incident at  $49.5^\circ$ . The  $n\Delta E < 0$  transitions are shown. The distributions are all smooth. No evidence of singularities exists.

From these calculations we can make several observations to guide us in our interpretation of the experimental data. The extremal scattering peaks should dominate the distribution. This should be particularly true at 300 K, where the peaks overlap to a significant extent, smearing out all but the sharpest features. These calculations were done assuming equal transition probability into each peak, except when a channel was closed to a particular wavelength. The disproportionate height of the extremal peaks is solely caused by the extremal focusing mechanism; it is not caused by differences in transition probability. We should be able to resolve these peaks even if only a fraction of the incident molecules undergo these

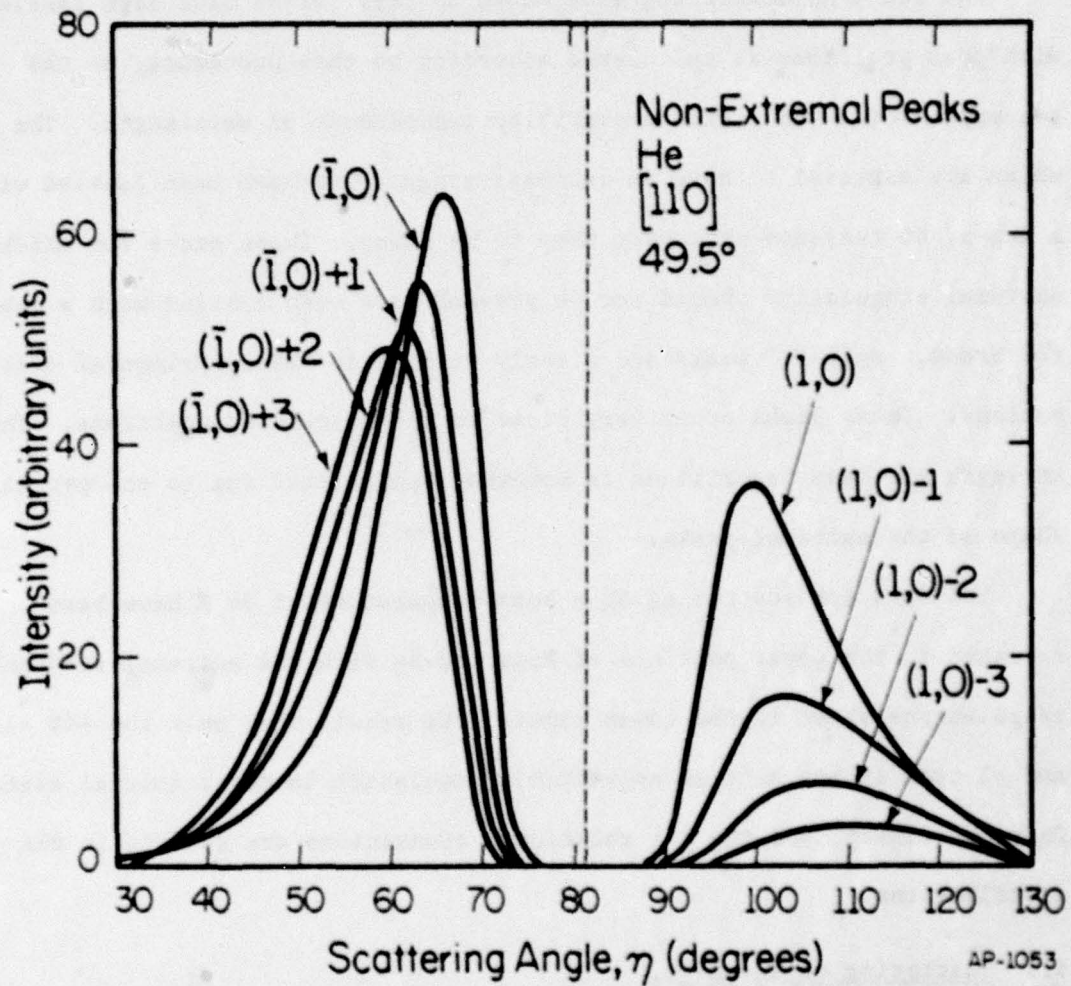


Fig. 51. Non-extremal HD transitions. The  $(\bar{1}, 0)$  gain peaks and  $(1, 0)$  loss peaks at 49.5 degrees are shown. Extremal singularities are not expected since  $\Delta E \cdot n < 0$ . These smooth shapes are typical of such non-extremal rotational transitions. Intensity in arbitrary units.

110

transitions. However, only those transitions for which  $n \cdot \Delta E > 0$  will have these singularities. Of these, only transitions having a significant number of molecules near  $\lambda_m$  will be strongly affected.

The 300 K HD scattering data shown in Figs. 37-41 have been labeled with peak positions as calculated according to this procedure, on the assumption of a transition probability independent of wavelength. The peaks which are expected to have an extremal singularity have been labeled with a sub-s, to indicate we expect them to be sharp. Those peaks for which the extremal singularity should not be present have been labeled with a sub-b, for broad. Only "s" peaks are clearly visible in the experimental distributions. These peaks occur very close to the calculated positions. The strength of these transitions is somewhat exaggerated due to the peculiar shape of the extremal peaks.

The data for scattering at a beam temperature of 80 K have been repeated in the upper portions of Figs. 52-54 with the extremal scattering calculations shown in the lower panels. We recall that only the +1, -1, and -2 transitions have an appreciable population in their initial states. Only the elastic and the  $\pm 1$  rotational transitions are evident in the distributions.

### 5.3 Scattering of H<sub>2</sub> and D<sub>2</sub>

The preceding data and calculations were for HD. Similar effects should occur for the scattering of H<sub>2</sub> and D<sub>2</sub>. It is instructive to consider what we expect for H<sub>2</sub> and D<sub>2</sub> in light of our findings for HD scattering. Rotational scattering is expected to be stronger for HD for several reasons. HD is a very asymmetric rotor, resulting in stronger coupling to the surface potential. Furthermore, as shown in Tables 1-3, the energies of the allowed

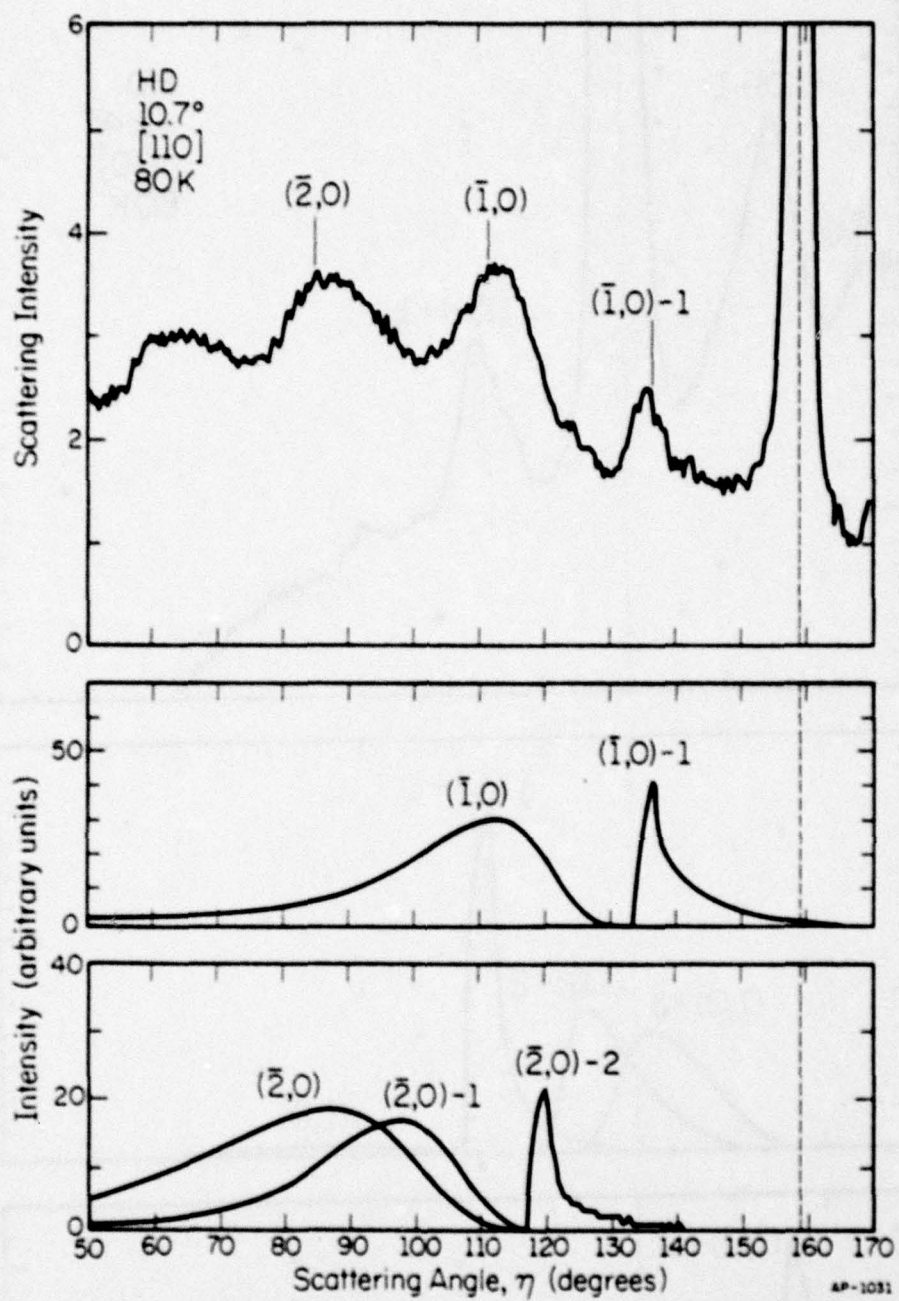


Fig. 52. HD scattering from MgO (001). [110] azimuth. 80 K beam. Experimental data in upper panel. Calculations in lower panel.

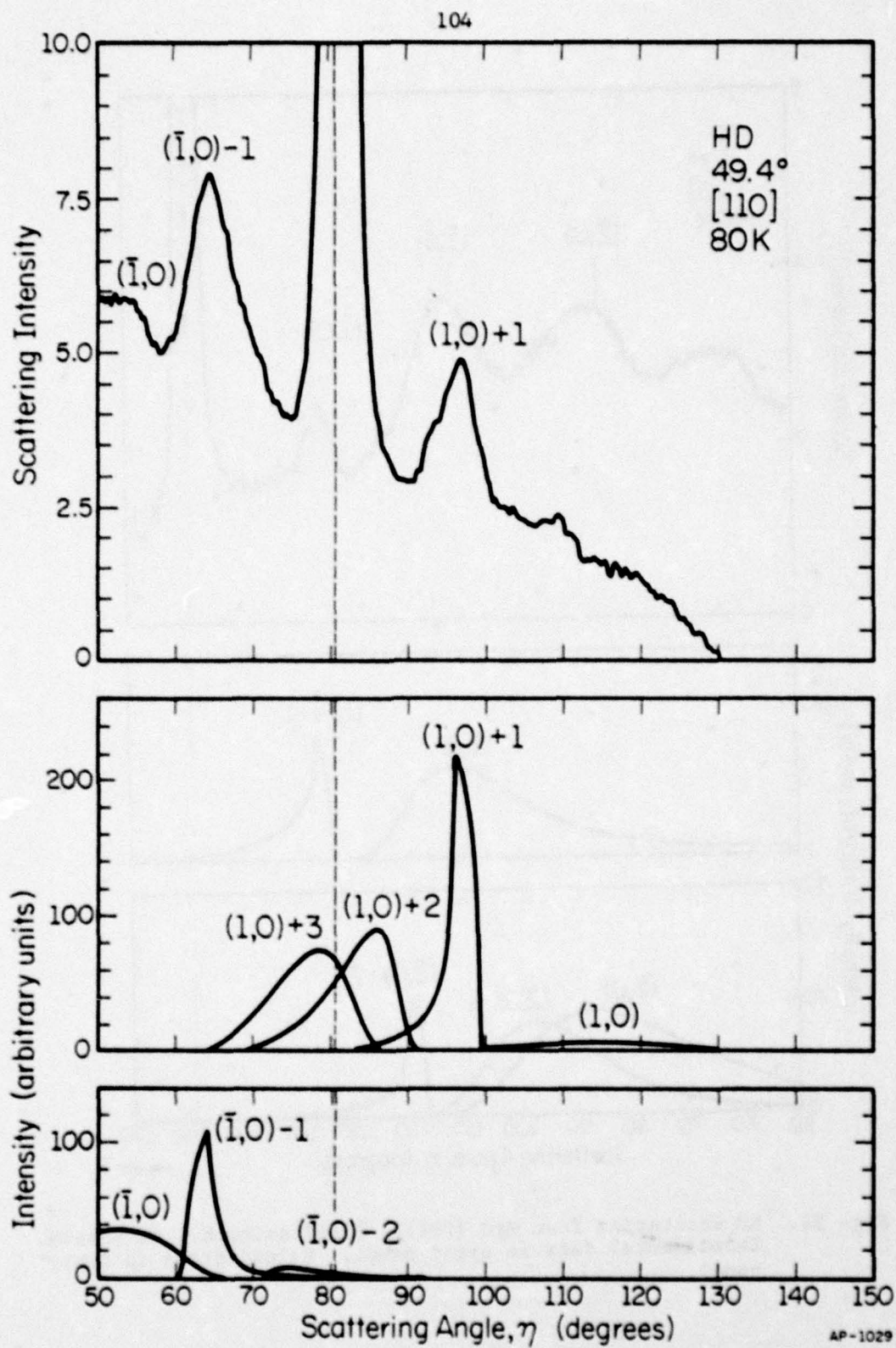


Fig. 53. HD scattering at 80 K. Same as Fig. 52 except 49.4° incident angle.

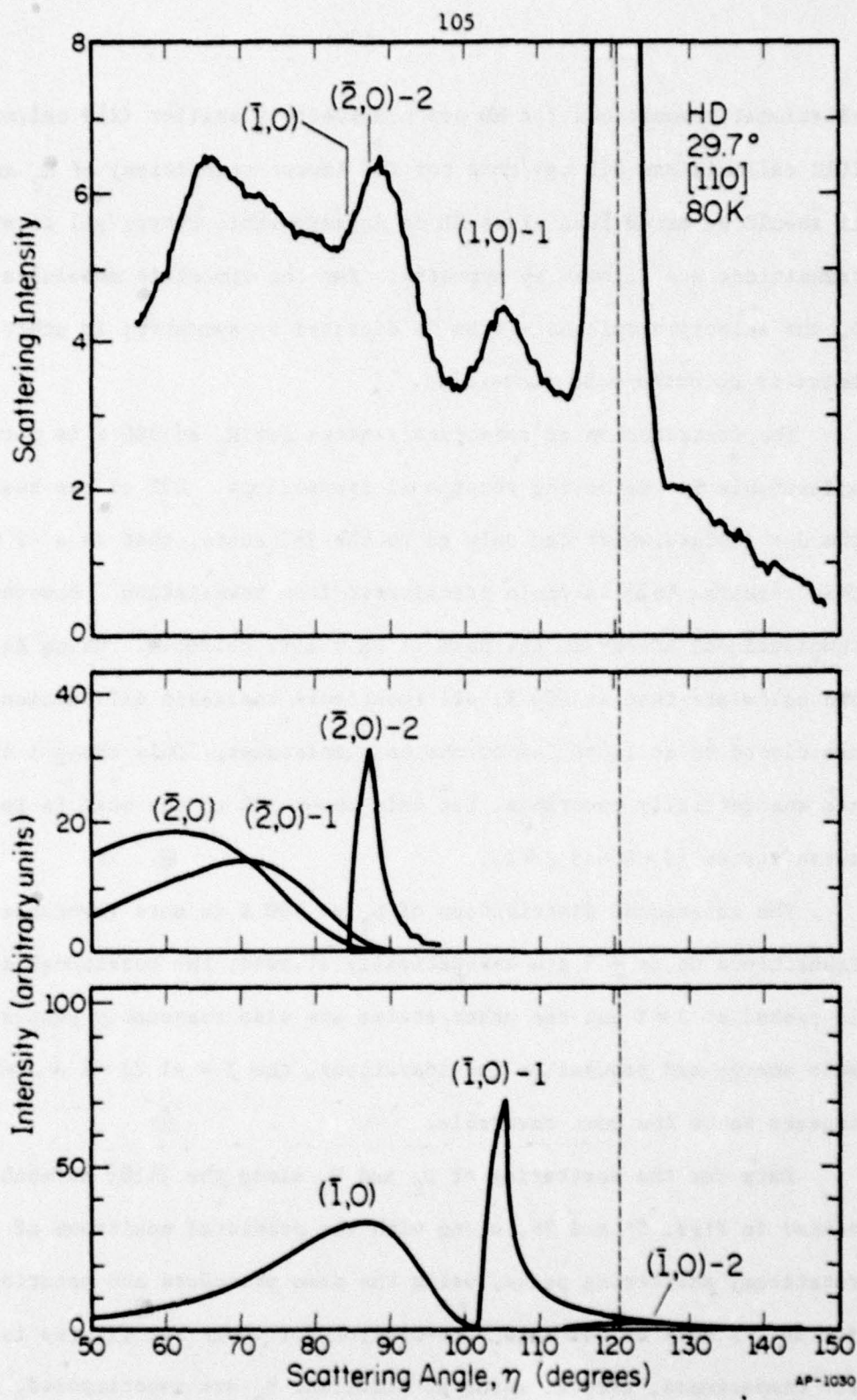


Fig. 54. HD scattering at 80 K. Experimental data in upper panel.  
 Calculated rotational transitions in lower channel.  
 $\theta_0 = 29.6^\circ$ .

rotational transitions for HD are considerably smaller (255 cal/mole vs. 1012 cal/mole and 512 cal/mole for the lowest transition) of  $H_2$  and  $D_2$ . It should be noted that since HD is an asymmetric rotor, all rotational transitions are allowed by symmetry. For the symmetric molecules  $H_2$  and  $D_2$ , the selection rule  $\Delta J = \text{even}$  is dictated by symmetry; in other words, there is no ortho-para conversion.

The distribution of rotational states for  $H_2$  at 300 K is particularly unfavorable for detecting rotational transitions. 65% of the beam is in the  $J = 1$  state, which can only go to the  $J=3$  state, that is a -2 transition. This requires 1678 cal/mole transferred from translation. However, the mean translational energy in the beam is only 1192 cal/mole. Using Eq. (33) we can calculate that at 300 K, all rotational inelastic diffraction channels are closed to at least 54% of the beam molecules. Only the  $\pm 1$  transitions are energetically favorable, but only about 10% of the beam is in each of these states ( $J = 0$  and  $J = 2$ ).

The rotational distribution of  $D_2$  at 300 K is more favorable (Table 3). Transitions up to  $\pm 3$  are energetically allowed; the rotational distribution is peaked at  $J = 2$  but the other states are also reasonably populated. From mere energy and population considerations, the  $I = +1$  ( $J = 2 \rightarrow J = 0$ ) transition appears to be the most favorable.

Data for the scattering of  $D_2$  and  $H_2$  along the [110] azimuth is presented in Figs. 55 and 56, along with the predicted positions of the rotational scattering peaks, using the same procedure and notation as used for HD. A note on the data presentation for these two figures is in order. For compactness, several scans at different  $\theta_0$  are superimposed. Each is shifted up from the previous one. The baseline appropriate to each curve

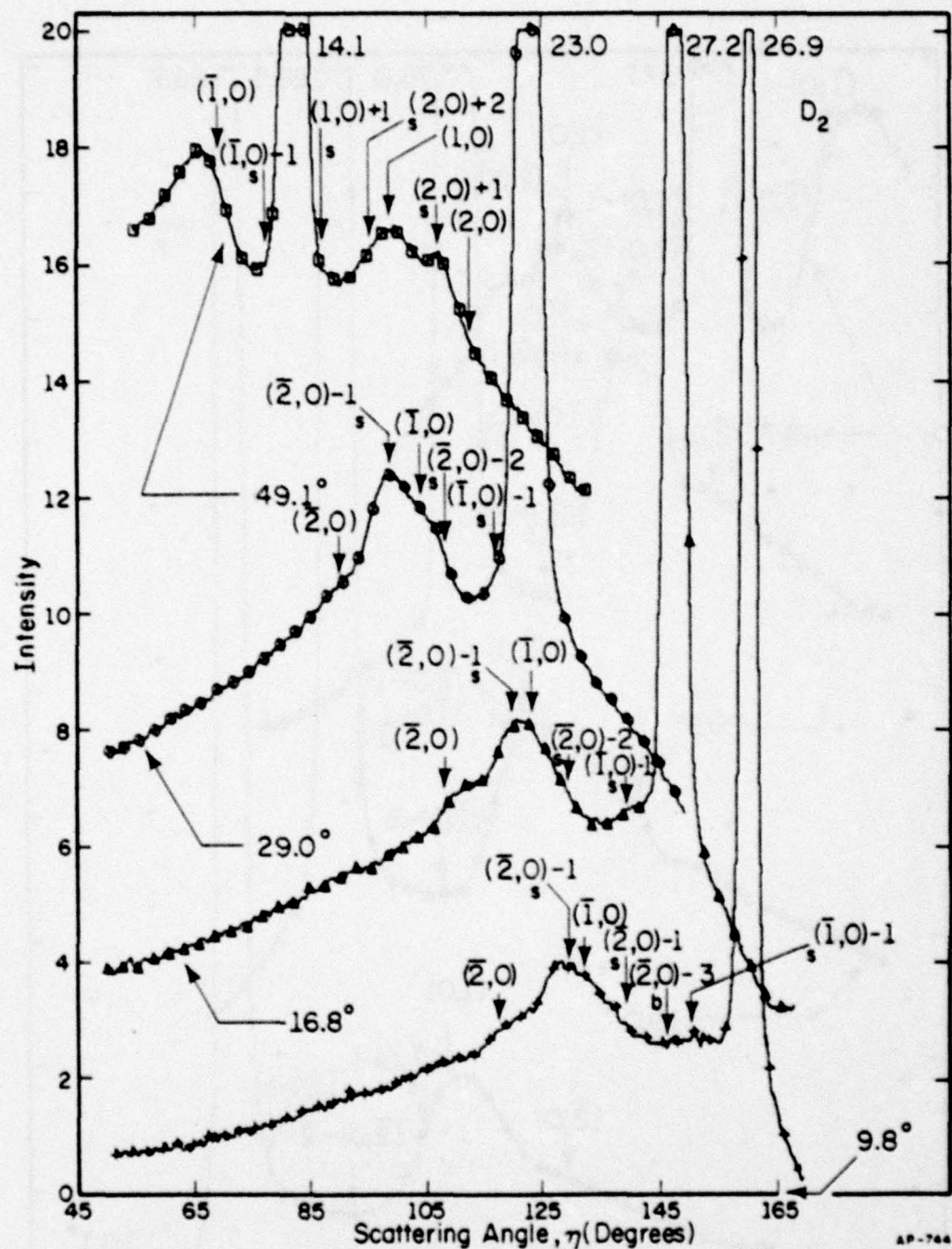


Fig. 55. D<sub>2</sub> scattering from MgO (001). [110] azimuth.

300 K beam, Only every 5-th data point marked.  
Each run shifted successively upward. Baseline  
indicated by horizontal portion of angle indicating  
incident angle.

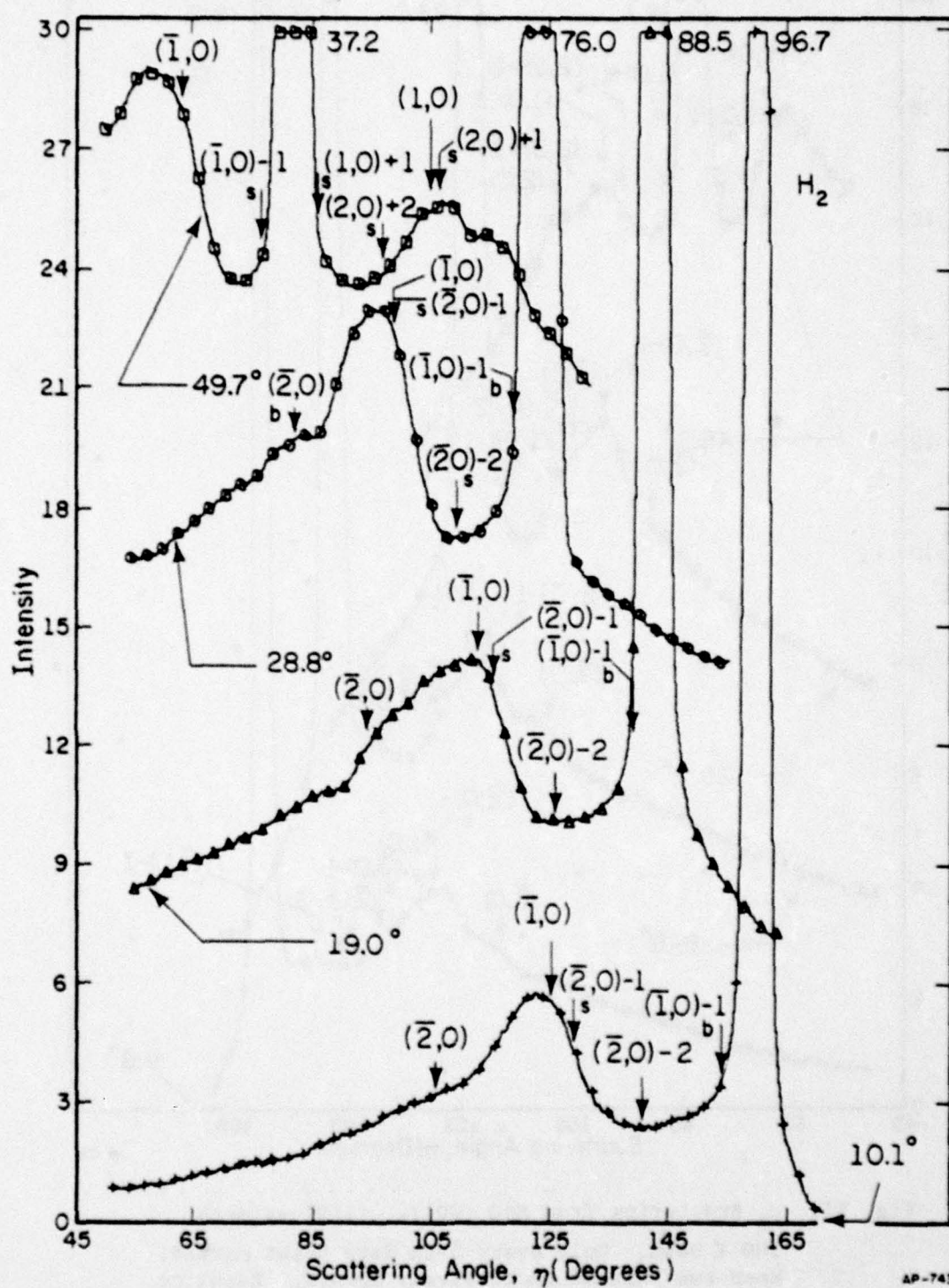


Fig. 56.  $H_2$  scattering, as in Fig. 50.

is indicated by the horizontal portion of the arrow indicating the incident angle. The full intensity of the specular peak is indicated where the peak extends off the page. Again, the expected extremal peaks have been labeled with a sub-"s".

We will consider the  $D_2$  data first. It is immediately evident that there is much less rotational inelastic scattering. The scattering is much more like the helium scattering in Chapter 4 than the HD scattering earlier in this chapter. There are a few peaks which can be identified as extremal scattering. The  $(2,0)+1$  for  $\theta_o = 49.1^\circ$  is most clearly marked. Additional evidence can be seen for the  $(\bar{2},0)-1$  for  $\theta_o = 29.0^\circ$  and the  $(\bar{1},0)-1$  for  $\theta_o = 9.8^\circ$ , but these are very weak. As expected from the considerations earlier in this section, the +1 rotational transition is the most distinct.

It is instructive to compare this  $D_2$  data to the helium data presented earlier. Deuterium and helium have the same mass and thus the same wavelength. The specular intensity for  $D_2$  is lower than for He by almost an order of magnitude. This is due to a large extent to the increased inelastic scattering involving rotational modes of the  $D_2$  molecules.

The  $H_2$  data in Fig. 56 show even less rotational scattering. Little direct evidence of any of the extremal transitions can be seen. The intensity of the specular peak is considerably more for  $H_2$  and  $D_2$ . This may, however, not all be due to decreased inelastic scattering. The wavelength of  $H_2$  is  $\sqrt{2}$  longer than that of  $D_2$  or helium at the same energy. There are thus fewer elastic diffraction channels open as well.

#### 5.4 Summary

The sharp peaks which appear in the scattering distributions of hydrogenic molecules from MgO are in keeping with the effects predicted by our theory of extremal scattering. These peaks are actually singularities in the differential scattering intensity. For these rotationally inelastic transitions, molecules with a significant range of wavelengths can be focused into a small angular increment. The resulting sharp peaks stand out against the smooth background of elastic scattering. In a sense, the use of a beam with a broad energy distribution has, therefore, proved to be an advantage.

Extremal scattering occurs for all the hydrogenic molecules, but is particularly strong for HD. It could, however, occur in the scattering of other, heavier diatomic molecules. Several things stand in the way, however. Diffraction, a necessary precondition for extremal scattering, has not yet been observed for these heavier molecules. Furthermore, the rotational levels of these molecules are so closely spaced that the peaks would not be separately resolvable. The occurrence of extremal singularities, has been very important, in allowing us to establish rotational-translational interchange. Rotational inelastic events of this type occur with high probability for the hydrogenic molecules. Although direct data are not available for other molecules, we expect rotational inelastic scattering, as described here, to play an important part in energy transfer for other diatomic molecules at surfaces.

## CHAPTER 6

## DIFFUSION OF CHEMISORBED GASES

The dynamics of chemical reactions on surfaces is governed to a large degree by the energetics of adsorption, diffusion, and desorptions of the reactant species. In a typical reaction, adsorbate molecules may have to diffuse to an active site or to each other in order to react. The rate of diffusion relative to the rate of desorption, for example, may be of critical importance. Little, however, is known about the energetics of diffusion of even simple gases on low index crystal surfaces.<sup>53,54</sup> One of the problems that has stood in the way of learning more about diffusion is the need to create a spatially localized initial deposit, the spreading of which can be studied. During the course of this investigation of molecular beam scattering, we have incidently mastered this particular aspect of the problem, and have developed a quite general technique for obtaining data on the surface diffusion of gases on macroscopic single crystal surfaces. It combines a molecular beam source with an Auger electron spectroscopy detector. The technique can be used for any gaseous species which adsorbs readily on the substrate of interest, with the notable exception of hydrogen. The substrate, however, must be in a form to allow rapid heating and cooling. Although quantitative data are not yet available because of difficulties with some of the instrumentation, the proposed technique and the equipment will be briefly described in this chapter.

#### 6.1 Experimental Apparatus

We wish to measure the rate at which a localized deposit proceeds toward a spatial equilibrium distribution by diffusion across the surface. We thus require 1) a method of establishing a reproducible lateral concentration gradient of the chemisorbed gas, and 2) a method of measuring both

the initial and final concentration profiles. We will use our molecular beam to create the initial deposit, and a form of scanning Auger electron spectroscopy to measure it. To carry out these measurements the scattering equipment in Figs. 4-5 has been modified as indicated by the schematic view in Fig. 57.

We are now interested in the gas which sticks to the surface, and not that which scatters. We will use the molecular beam to form the concentration gradient. This is done by slowly rotating the sample in an arc in front of the molecular beam. If done under the proper conditions, this should produce a narrow line of chemisorbed gas running across the crystal. The flux of molecules at the surface from the molecular beam is approximately  $10^3$  times the flux due to the background gas, so there should be considerable contrast between the line deposit and the background. The beam has been stopped down to approximately 0.020" diameter for these experiments. We thus expect a line extending across the crystal surface slightly wider than 0.020".

Auger electron spectroscopy will be used to measure the lateral concentration profile. In this technique, we measure the energy distribution of secondary electrons when the sample is bombarded with  $\approx 3$  kV electrons. Each element has a characteristic set of transitions. Because of the short mean free path of low energy electrons in a solid, the technique is only sensitive to the surface layer. Concentrations down to  $\sim 0.1\%$  can be detected for most elements.

A commercially available cylindrical mirror electrostatic energy analyzer (CMA) (PHI, 10-234 G) is used to detect the Auger electrons. The spatial resolution is limited by the lateral size of the electron beam.

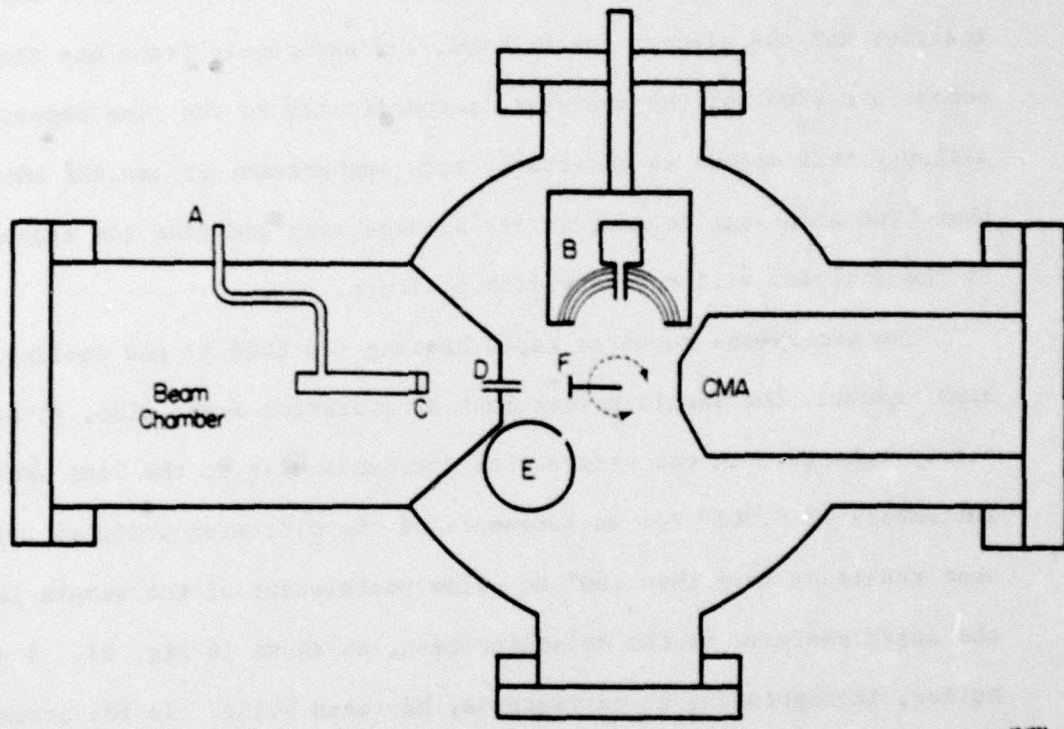


Fig. 57. Modified molecular beam system for diffusion studies. Top view.  
A) Gas inlet, B) L.E.E.D screen, C) Source, D) Collimator,  
E) Mass spectrometer, F) Sample; CMA is the cylindrical mirror  
Auger analyzer.

Our analyzer delivers a beam 0.004" in diameter at 3 kV. Scanning Auger electron spectroscopy typically involves electrostatically deflecting the beam back and forth across the surface with the analyzer fixed. One can thus obtain lateral concentration profiles. The field of view of most electron energy analyzers is quite small, however; one is typically limited to areas less than 1/2 mm by 1/2 mm. That is too small for this experiment, as the initial deposit is larger than that. We will therefore keep the analyzer and the electron beam fixed, and accurately translate the sample across the front of the analyzer, perpendicular to the line deposit. Although this method is admittedly more cumbersome, it has the advantages that line scans can be done across a large area and that the transmission of the analyzer will not vary with position.

The experiment requires rapid heating (to 2400 K) and cooling in ultra high vacuum. The sample holder must be vibration free; also, it must accurately translate in the y-direction (perpendicular to the line source) in increments of 0.001" for measurements of the diffusion profile. Finally, it must rotate by more than 180° to allow positioning of the sample in front of the Auger analyzer or the molecular beam, as shown in Fig. 57. A new sample holder, incorporating these features, has been built. In the present design, the sample, in the form of a 0.010" thick wafer, is electron beam welded to two 0.080" W pins. These are firmly held in molybdenum clamps which are an integral part of the liquid nitrogen cooling tubes, as shown in Fig. 58. The sample is heated by passing current directly through it. On the order of 100 amps are required to heat the crystal to 2000 K; it cools from 1400 K to room temperature in  $\approx$  15 seconds. The requirements of good thermal and electrical contact as well as rigidity are at odds with the thermal

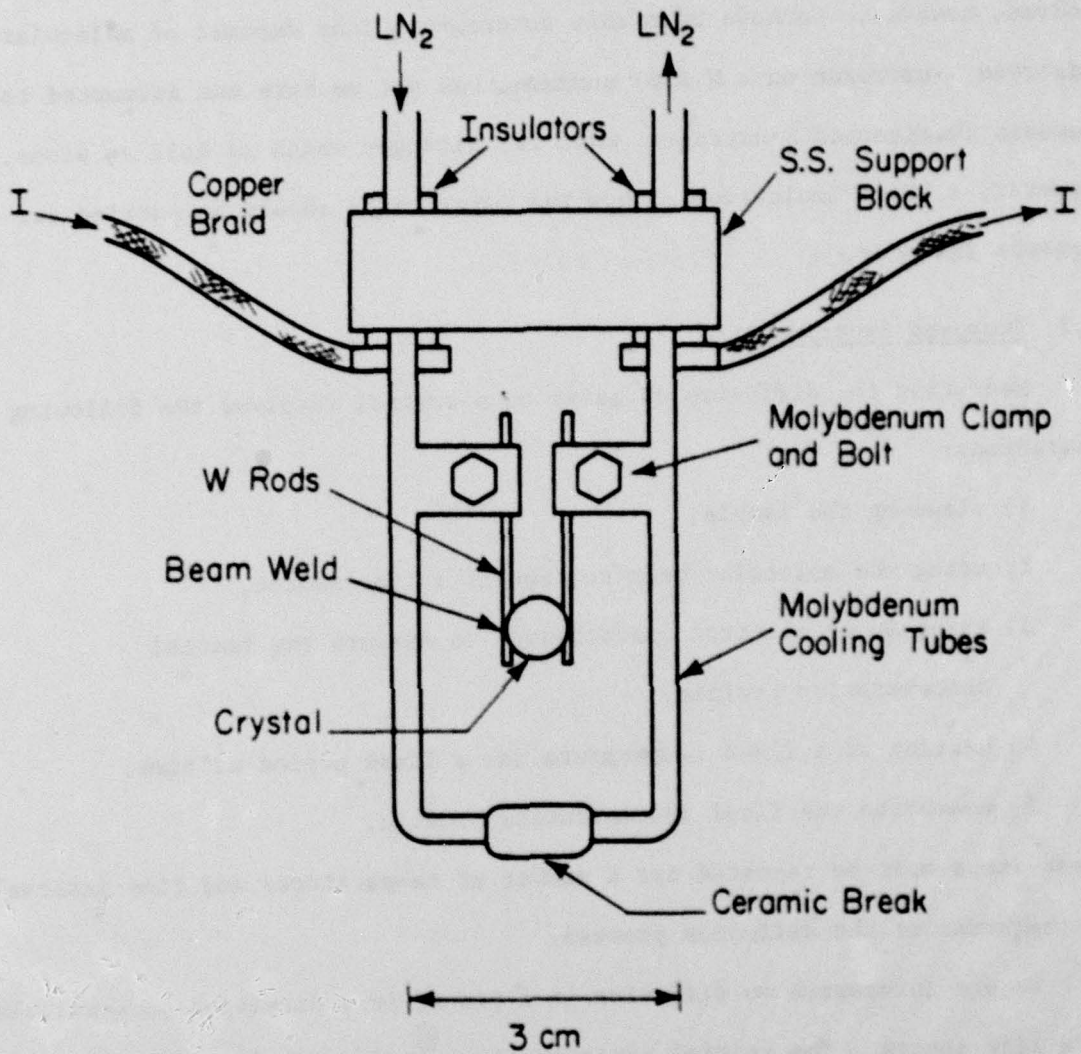


Fig. 58. Schematic view of sample holder for diffusion studies.

expansion of the crystal when heated to 2400 K. These problems have prevented quantitative experiments to date. Most difficulties appear to be solved, however. We have been able to create a line deposit of molecularly adsorbed  $\gamma$ -nitrogen on a W(110) surface. As yet we have not attempted to deposit chemisorbed  $\beta$ -nitrogen, that is, nitrogen which is held as atoms. However, a brief indication of how the experiments should be carried out appears in order.

### 6.2 Proposed Experiments

Measuring the diffusion of gases on a crystal involves the following operations:

- 1) cleaning the sample,
- 2) using the molecular beam to deposit a line source,
- 3) using Auger electron spectroscopy to measure the initial concentration profile,
- 4) heating at a fixed temperature for a fixed period of time,
- 5) measuring the final concentration profile.

These steps must be repeated for a number of temperatures and time intervals to characterize the diffusion process.

We are interested in diffusion in a plane, in a direction perpendicular to a line source. The initial concentration profile  $C(x,0)$ , and the final concentration profile,  $C(x,t)$ , are actually measured. Diffusion proceeds according to Fick's second law,<sup>55</sup> which in one dimension is

$$\frac{\partial C(x,t)}{\partial t} = \frac{\partial}{\partial x} (D \frac{\partial C(x,t)}{\partial x}) , \quad (38)$$

where  $D$  is the diffusion coefficient. We will assume that  $D$  is independent of concentration; Eq.(38) then reduces to

$$\frac{\partial C(x,t)}{\partial t} = D \frac{\partial^2}{\partial x^2} C(x,t) . \quad (39)$$

For an initial distribution in the form of a delta function, that is, for

$$C(x,t=0) = C_0 \delta(x) ,$$

the solution to Eq. (39) can be written by inspection as

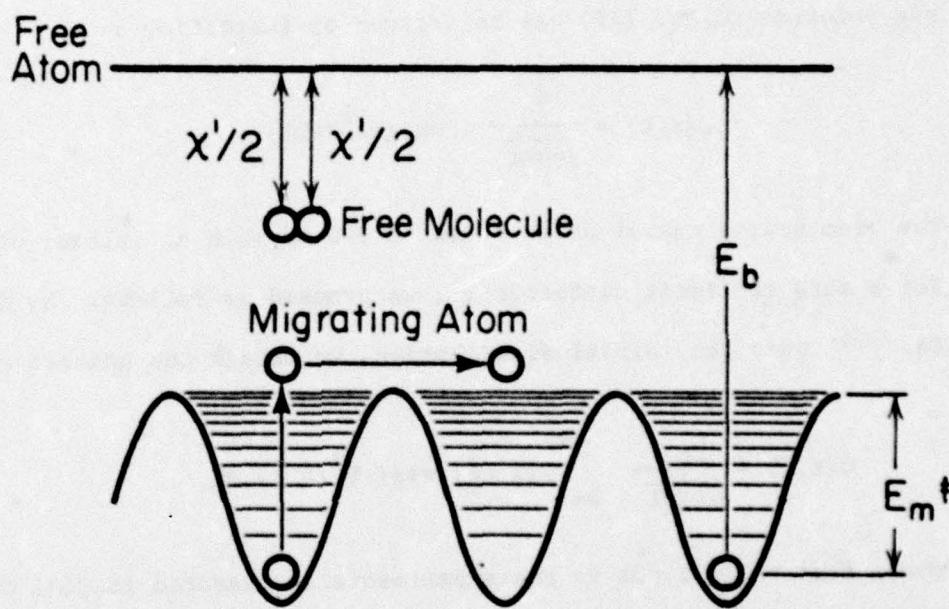
$$C(x,t) = \frac{C_0}{\sqrt{4\pi Dt}} \exp(-x^2/4Dt) . \quad (40)$$

The beam source cannot be expected to create such an initial distribution. For a more realistic distribution, we proceed as follows. By integrating Eq. (40) over the initial distribution, we obtain the general solution

$$C(x,t) = \frac{C_0}{\sqrt{4\pi Dt}} \int_{-\infty}^{+\infty} f(x+\xi) \exp(-\xi^2/4Dt) d\xi , \quad (41)$$

where  $f(x) = C(x,t=0)$  is the experimentally measured initial concentration at  $x$ . Substitution into Fick's second law, Eq. (39), confirms that this is the correct solution. For simple distributions, this integral can be done analytically. Otherwise, it is necessary to evaluate it numerically. In either case, the experimental data, that is,  $C(x,0)$  and  $C(x,t)$  at a fixed temperature, are fit to this solution using the diffusion constant,  $D$ , as a variable parameter.

Diffusion on a solid surface generally occurs over an activation barrier. The atom must gain sufficient energy to surmount the barrier between binding sites. This is shown schematically in Fig. 59. The



AS-754

Fig. 59. Schematic potential barrier diagram for diffusion.  $E_m^*$  is activation barrier to diffusion.

diffusion coefficient can be written in terms of this activation barrier,  $E_m^{\ddagger}$ , as

$$D(T) = D_0 e^{-E_m^{\ddagger}/kT}, \quad (42)$$

where T is the temperature. From measurement of D(T) vs T we obtain the activation barrier to diffusion. Our diffusing atoms thus provide us with a microscopic probe of the surface potential.

The above technique can be applied to almost any gas-solid system in which the gas chemisorbs readily from the gas phase. The major exception is hydrogen, which has no Auger transitions. Some other method would be necessary to detect hydrogen. We have begun studies on the diffusion of chemisorbed nitrogen on tungsten (100). The adsorption of nitrogen on tungsten has previously been extensively characterized. This makes it an ideal system for our initial studies.

There are numerous interesting problems to which this technique can be applied. For instance, the diffusion of a gas on various planes of the same material can be studied. Of particular interest is diffusion on highly anisotropic planes such as the W(112), which is composed of one-dimensional channels. Studies in the field ion microscope<sup>56</sup> have shown that for metal adatoms, diffusion occurs only along the channels, not over the ridges. The correlation of diffusion behavior of chemisorbed gas with substrate structure would provide us with valuable information on microscopic surface forces.

## REFERENCES

1. F. O. Goodman and H. Y. Wachman, Dynamics of Gas-Surface Scattering, Academic Press (New York, 1976).
2. I. Stern and O. Estermann, Z. Physik, 61, 95 (1930).
3. a) C. J. Davisson and L. Germer, Phys. Rev., 30, 705 (1927);  
b) C. J. Davisson and L. Germer, Nature, 119, 558 (1927).
4. D. R. O'Keefe, J. N. Smith, Jr., R. L. Palmer, and H. Saltsburg, Surf. Sci. 20, 27 (1970).
5. J. C. Crews, J. Chem. Phys., 37, 2004 (1962).
6. D. R. O'Keefe, R. L. Palmer, H. Saltsburg, and J. N. Smith, Jr., J. Chem. Phys., 49, 5194 (1968).
7. R. L. Palmer, D. R. O'Keefe, H. Saltsburg, and J. N. Smith, Jr., J. Vac. Sci. Tech., 7, 91 (1970).
8. R. Sau and R. P. Merrill, Surf. Sci., 34, 268 (1973).
9. R. M. Logan, Mol. Phys., 17, 147 (1969).
10. R. G. Rowe, Ph.D. Thesis, University of Illinois, (1974).
11. a) R. G. Rowe and G. Ehrlich, J. Chem. Phys., 62, 735 (1975);  
b) R. G. Rowe and G. Ehrlich, J. Chem. Phys., 63, 4648 (1975).
12. a) G. Boato, P. Cantini and L. Mattera, Japan J. Appl. Phys. Suppl. 2, Pt. 2, 533 (1974);  
b) G. Boato, P. Cantini and L. Mattera, J. Chem. Phys., 65, 544 (1976).
13. H. Chow, Surf. Sci., 62, 487 (1977).
14. N. Cabrera, V. Celli, F. O. Goodman, and J. R. Manson, Surf. Sci., 19, 67 (1970).
15. a) G. Wolken, Jr., J. Chem. Phys., 58, 3047 (1973);  
b) G. Wolken, Jr., Chem. Phys. Letters, 21, 373 (1973).
16. For a complete review of the present state of molecular beam scattering theory, the reader is referred to F. O. Goodman, CRC Crit. Rev. in Sol. State and Mat. Sci., 7, 33 (1977).
17. See, for example, W. H. Miller, Adv. in Chem. Phys., 25, 69 (1974).

18. a) R. A. Marcus, J. Chem. Phys., 56, 311 (1972);  
b) R. A. Marcus, J. Chem. Phys., 59, 5135 (1973).
19. a) W. H. Miller, J. Chem. Phys., 53, 1949 (1970);  
b) W. H. Miller, J. Chem. Phys., 53, 3578 (1970);  
c) W. H. Miller, J. Chem. Phys., 54, 5386 (1970).
20. a) R. I. Masel, R. P. Merrill and W. H. Miller, Surf. Sci., 46, 681 (1974);  
b) R. I. Masel, R. P. Merrill and W. H. Miller, J. Vac. Sci. Tech., 13, 355 (1976);  
c) R. I. Masel, R. P. Merrill and W. H. Miller, J. Chem. Phys., 64, 45 (1976);  
d) R. I. Masel, R. P. Merrill and W. H. Miller, J. Chem. Phys., 65, 2690 (1976).
21. a) J. D. Doll, Chem. Phys., 3, 257 (1974);  
b) J. D. Doll, J. Chem. Phys., 61, 954 (1974).
22. D. R. Dion and J. D. Doll, Surf. Sci., 58, 415 (1976).
23. K. J. McCann and V. Celli, Surf. Sci., 61, 10 (1976).
24. W. A. Steele, Surf. Sci., 38, 1 (1973).
25. A. Farkas, Orthohydrogen, Parahydrogen, and Heavy Hydrogen, The University Press (Cambridge, 1935).
26. A. Kantrowitz and J. Gray, Rev. Sci. Inst., 22, 328 (1951).
27. R. Campargue, Rev. Sci. Inst., 35, 111 (1964).
28. F. Reif, Fundamentals of Statistical and Thermal Physics, McGraw-Hill (New York, 1965).
29. N. F. Ramsey, Molecular Beams, Clarendon Press (Oxford, 1956).
30. For general reviews of molecular beam scattering techniques from surfaces, the reader is referred to: J. P. Toennies, Appl. Phys., 3, 91 (1974); S. T. Ceyer and G. A. Somorjai, Ann. Rev. Phys. Chem., 28, 477 (1977).
31. C. B. Lucas, Vacuum, 23, 395 (1973).
32. S. G. Kukolich, D. E. Oates, and J. H. S. Wang, J. Chem. Phys., 61, 4686 (1974).
33. R. J. Gallagher and J. B. Fenn, J. Chem. Phys., 60, 3492 (1974). 150

34. G. Frodsham, Rev. Sci. Inst., 46, 312 (1975).
35. B. F. Mason and B. R. Williams, Surf. Sci., 45, 141 (1974).
36. G. Boato, P. Cantini and L. Mattera, Surf. Sci., 55, 141 (1976).
37. W. Bayh and H. Pflug, Z. Angew. Phys., 25, 358 (1968).
38. T. E. Gallon, I. G. Higginbotham, M. Prutton and H. Tokutaka, Surf. Sci., 21, 224, 233, 241 (1970).
39. Y. Murata, S. Murakami, H. Namba, T. Gotoh and K. Kinosita, Proc. 7th Int. Vac. Conf. and 3rd Intern. Conf. Solid Surfaces (Vienna, 1977) p. 2439.
40. The author has found the presentations of references 16 and 23 particularly useful for the development of the semiclassical approximation to surface scattering. References 20 and 22 are particularly useful from an applications standpoint. The development of the primitive and uniform semiclassical approximations as applied to gas phase problems is thoroughly covered in reference 19.
41. H. Goldstein, Classical Mechanics. Addison-Wesley (Reading, Mass., 1965).
42. R. P. Feynman and A. R. Hibbs, Path Integrals and Quantum Mechanics, McGraw-Hill (New York, 1965).
43. C. Eckart, Rev. Mod. Phys., 20, 399 (1948).
44. G. Wolken, J. Chem. Phys., 61, 456 (1974).
45. See Ref. 1, p. 66.
46. An error in Eq. (21) of reference 22 should be noted. Our Eq. (31) is correct as presented here.
47. Much of the literature on molecular beam scattering has developed with the angles  $\theta_0$  and  $\theta$  measured from the surface normal. The angles  $\theta_0$  and  $\theta$  used in this thesis are measured up from the surface. They are obviously related by  $\theta_{\text{ours}} = 90^\circ - \theta_{\text{theirs}}$ . Although this thesis is internally consistant, care must be taken in comparing these formulas to those in the literature.
48. U. Garibaldi, A. C. Levi, R. Spadacini and G. E. Tommei, Proc. 2nd Int. Conf. on Solid Surf., Tokyo (1974), Japan; J. Appl. Phys. Suppl. 2, pt. 2, 549 (1974).

49. See ref. 1, p. 214.
50. A. Tsuchida, Surf. Sci., 46, 611 (1974).
51. L. Rathbun and G. Ehrlich, Proc. 10th Int. Symp. on Rarefied Gas Dynamics, Progress in Astronautics and Aeronautics, Vol. 51, Part II, p. 555, AIAA (New York, 1977).
52. R. G. Rowe, L. Rathbun and G. Ehrlich, Phys. Rev. Lett., 35, 1104 (1975).
53. A. Polak and G. Ehrlich, J. Vac. Sci. Tech. 14, 407 (1977).
54. R. Butz and H. Wagner, Surf. Sci. 63, 448 (1977).
55. J. Crank, The Mathematics of Diffusion, Clarendon Press (Oxford, 1956).
56. See, for example, G. Ehrlich, Surf. Sci. 63, 422 (1977).

## VITA

Lynn Rathbun was born in Toledo, Ohio on October 9, 1949. He graduated from Bryan High School, Bryan, Ohio in 1967. He attended The Ohio State University from 1967 to 1971, receiving a B.S. in Physics in June 1971. Thereafter, he entered graduate school at the University of Illinois in the Physics Department in September 1971. In June 1972 he began research in the Coordinated Science Laboratory under Professor Gert Ehrlich. He received a M.S. in Physics in January 1973 and continued working toward the Ph.D. This research has to date resulted in the following publications:

"Extremal Effects in Rotationally Inelastic Diffraction," with R. G. Rowe and G. Ehrlich, Phys. Rev. Letters.

"Extremal Scattering of Molecular Hydrogen from (001) MgO," with G. Ehrlich, Proceedings 10th Int. Rarefied Gas Dynamics Conf., Aeronautics and Astronautics, Vol. 51, pt. 1, p. 555, AIAA (New York, 1977).